Continuous Observations of Atmospheric Trace Gases by Ground-based FTIR Spectroscopy at Izaña Observatory, Tenerife Island

M. Schneider
Institut für Meteorologie und Klimaforschung

Mai 2002

Continuous Observations of Atmospheric Trace Gases by Ground-based FTIR Spectroscopy at Izaña Observatory, Tenerife Island*

Matthias Schneider

Institut für Meteorologie und Klimaforschung

*Von der Fakultät für Physik der Universität Karlsruhe (TH) genehmigte
Dissertation

Abstract

Worldwide stratospheric ozone decline is observed with great concern, since it yields an increase of the harmful UV radiation on the Earth surface and it may contribute to climate change. While in the past, it was focused on the investigation of the polar atmosphere, there is now a growing interest in lower latitudes, where stratospheric O_3 is mainly produced and measurement data are still sparse. Therefore, a Fourier spectrometer manufactured by Bruker was installed at the subtropical site of the Izaña Observatory (28°N, 2367 m a.s.l.) on Tenerife, Spain, in February 1999, with the objective to perform long-term measurements.

Between February 1999 and July 2001 measurements on approximately 200 days were conducted and analyzed within this work. The height dependent pressure broadening allows to invert trace gas profiles by the measured solar absorption spectra. The inversion was performed using the Tikhonov-Phillips method on a logarithmic scale.

The retrieved profiles and column amounts showed typical annual cycles with enhanced upwelling in summer, due to a stratosphere with strong tropical characteristics, and relatively high variability in winter, caused by horizontal transport as a result of enhanced wave activity. We found a good agreement between the column amounts determined by the Fourier spectrometer and those obtained by Differential Optical Absorption Spectroscopy, the Brewer spectrometer, O_3 sondes, radiosondes, and measurements conducted simultaneously by another Fourier spectrometer close to Izaña. We also compared O_3 sonde profiles and O_3 profiles obtained by the Fourier spectrometer, which coincided on 45 days, and found good agreement. H_2O profiles detected by the radiosonde coincided on 152 days with the Fourier spectrometer measurements. The corresponding profiles agree well between 4 and 20 km.

Data of a three dimensional Chemical Transport Model were available for nearly the whole measurement period. These data show a similar annual evolution, however, some significant differences from the Fourier spectrometer results are found. All these differences can be explained by the modelled stratosphere with a stronger coupling to the tropics than detected in the measurements.

The short-term variability of the trace gases can be attributed mainly to transport processes. This was shown by trace gas ratios which show less short-term variability than the respective trace gas column amounts themselves. Further investigation of the trace gas variations was made with meteorological parameters, like tropopause height and backward trajectories. A correlation was derived between the tropopause height and the trace gas profiles, which confirms the role of vertical transport in short-term variability. The importance of horizontal transport in this respect was demonstrated by a correlation between the origin of the airmasses and

the trace gas profiles.

While the model shows no correlation with the tropopause height, it demonstrates a similar correlation with the origin of the airmass. The former may be attributed to a boundary effect, since the lowest model layer (10 km) is in the typical tropopause region. The latter demonstrates that the model calculates a latitudinal trace gas variation similar to that detected by the Fourier spectrometer.

Zusammenfassung:

Langzeitbeobachtungen atmosphärischer Spurengase mittels bodengebundener FTIR Spektroskopie am Izaña Observatorium, Teneriffa

Der weltweite stratosphärische Ozonabbau wird mit großer Sorge beobachtet, da er zu einer Erhöhung der schädlichen UV Strahlung an der Erdoberfläche führt und möglicherweise zu Klimaveränderungen beiträgt. Während in der Vergangenheit das Hauptaugenmerk auf der Erforschung der polaren Atmosphäre lag, ist in letzter Zeit das Interesse an den Prozessen niederer Breiten, wo stratosphärisches Ozon hauptsächlich produziert wird, gestiegen. Aus diesen Regionen liegen jedoch noch wenig Messdaten vor. In diesem Zusammenhang wurde im Februar 1999 ein Fourier Spektrometer der Firma Bruker an einem subtropischen Ort, dem Izaña Observatorium (28°N, 2367 m ü.NN) auf Teneriffa, in Betrieb genommen. Ziel war es, Messungen über einen längeren Zeitraum durchzuführen.

Zwischen Februar 1999 und Juli 2001 wurden an annähernd 200 Tagen Messungen durchgeführt und anschließend ausgewertet. Die höhenabhängige Druckverbreiterung der Absorptionslinien ermöglicht es, aus den gemessenen solaren Spektren Spurengasprofile zu invertieren. Als Inversionsverfahren kam die Tikhonov-Phillips Methode auf einer logarithmischen Skala zur Anwendung.

Die ermittelten Profile und Säulengehalte zeigten typische Jahresgänge mit ausgeprägtem Aufsteigen der Luftmassen im Sommer, bedingt durch den Einfluss der Tropen, und relativ starken Variabilitäten im Winter, verursacht durch verstärkte Wellenaktivität. Es ergab sich eine gute Übereinstimmung zwischen den ermittelten Säulengehalten des Fourier Spektrometers und den Ergebnissen aus Differentieller Optischer Absorptionsspektroskopie, eines Brewer Spektrometers, O_3 Sonden, Radiosonden, und weiteren FTIR Messungen, welche gleichzeitig in der Nähe des Izaña Observatoriums durchgeführt wurden. Weitere gute Übereinstimmungen ergaben die Vergleiche der O_3 Sondenprofile und der O_3 FTIR Profile, welche an 45 Tagen gleichzeitig bestimmt wurden, sowie der H_2O Radiosondeprofile und der H_2O FTIR Profile für Höhen zwischen 4 and 20 km. Die H_2O Messungen wurden an 152 Tagen gleichzeitig durchgeführt.

Die Berechnungen eines dreidimensionalen Chemischen Transport Modells wurden mit den FTIR Messungen verglichen. Obwohl das Modell ähnliche Jahreszyklen zeigt, gibt es bedeutende Unterschiede zu den Messungen. All diese Unterschiede

iv

weisen konsistent darauf hin, dass das Modell die Kopplung zwischen der tropischen und außertropischen Stratosphäre überschätzt

Die kurzzeitigen Variabilitäten der Spurengase sind größtenteils Transport-prozessen zuzuschreiben. Dies wird deutlich anhand der Verhältnisse der Säulengehalte von Spurengasen, welche eine geringere Variabilität aufzeigen als die entsprechenden einzelnen Säulengehalte. Weiterhin wurden die kurzzeitigen Variabilitäten der Spurengase mittels meteorologischer Parameter, wie der Tropopausen-höhe und Rückwärtstrajektorien, untersucht. Es ergab sich ein Zusammenhang zwischen der Tropopausenhöhe und den Spurengasprofilen, welches die Bedeutung des vertikalen Transports hervorhebt. Die Rolle horizontaler Transportprozesse wurde durch den Zusammenhang der Spurengasprofile mit der Herkunft der Luftmassen aufgezeigt.

Die Modellrechnungen hingegen zeigen keinerlei Korrelationen mit der Tropopausenhöhe, welchem möglicherweise ein Randeffekt zu Grunde liegt, da sich die unterste Modellschicht (10 km) in der typischen Region der Tropopause befindet. Die Modellprofile zeigen jedoch einen ähnlichen Zusammenhang mit der Herkunft der Luftmassen wie die Messungen. Dies legt nahe, dass die Breitengradabhängigkeit der Spurengase vom Modell in Übereinstimmung zu den FTIR Messungen berechnet wird.

Contents

viii

Chapter 1

Introduction

In the past few decades, it has become obvious that the impact of human activity could cause an environmental change on a global scale. A notable example is the worldwide decline of stratospheric ozone. It yields an increase of the harmful UV radiation on the Earth's surface and it may contribute to climate change.

When in 1985, the dramatic decrease of stratospheric ozone during early spring in the Antarctic polar region was reported for the first time [16], it was completely unexpected. But quickly consensus was reached and meanwhile, polar ozone depletion seems to be well understood. It is dominated by halogenic catalytic cycles and strongly linked to heterogeneous reactions that take place on Polar Stratospheric Clouds (PSCs).

Due to the quick progress made in the scientific understanding of the ozone depletion, the Montreal Protocol came into force in 1989 already. It restricts ozone-destroying substances. In the 1990s it was followed by further amendments and adjustments, resulting in stricter regulations on ozone-depleting substances.

Nevertheless, a number of questions still remain unresolved. In particular, the ozone decrease at mid-latitudes and the subtropics needs further investigation. Since there are higher solar fluxes and temperatures compared to polar regions, its ozone decrease of (0.6% per year at mid-latitudes and 0.2% per year at subtropics) cannot be explained solely by the same processes as for high latitudes.

A number of mechanisms are in discussion. Firstly, transport of ozone-depleted air or air containing direct precursors of ozone-destroying substances from the polar vortex to mid-latitudes may serve as an explanation. Secondly, sulfate aerosol or carbon aerosol may replace PSC only present in polar regions and, thus, enable heterogeneous reactions in analogy to polar regions ([69]). Thirdly, transport of aerosol-loaded air or precursors of ozone-destroying species from the tropics, where the majority of source gases injected into the atmosphere enter the stratosphere, to mid-latitudes may be important.

A detailed study of these mechanisms must be based on measurements. Apart

from giving a description of the actual state or trends present in the stratosphere they are necessary to validate model calculations and, hence, allow to test the assumed mechanisms. Ground-based measurements are also essential for the validation of satellite instruments, which themselves allow a global observation of the atmosphere. However, while at high latitudes a lot of measurement sites are operative, data from low latitudes are sparse. In this context, we present zenith column amounts (ZCA) and profiles of important atmospheric trace gases (H_2O, N_2O, CH_4, OCS, HCN, O_3, HF, HCl, $ClONO_2$, NO_2, NO, and HNO_3) for a subtropical site derived from ground-based FTIR measurements. On roughly 200 days between February 1999 and July 2001 measurements were conducted at the Izaña Observatory (IZO) on the Island of Tenerife (28°N). An analysis of all these measurements within this work was only possible by some automatization of the evaluation procedure.

In spring 2001, IZO was accepted as a complementary site within the Network for Detection of Stratospheric Change (NDSC) due to its DOAS (Differential Optical Absorption Spectroscopy), Brewer spectrometer, O_3 sounding, and FTIR activities.

In order to retrieve profiles from the measured spectra, the characteristics of the FTIR spectrometer have to be known accurately. Therefore, the instrumental line shape (ILS) was determined approximately every two months according to a method described in [26]. This measured ILS was then applied in the retrieval algorithm.

The time series of $2\frac{1}{2}$ years allows to observe typical annual cycles of the ZCAs and profiles of the trace gases, which can be attributed to typical dynamical and chemical processes, present in these latitude regions.

The retrieved ZCA and profiles are compared to results obtained by Differential Optical Absorption Spectroscopy (DOAS), the Brewer spectrometer, O_3 sondes, radiosondes, and other FTIR measurements conducted simultaneously at IZO or in its vicinity. They are also compared to a 3-D chemical transport model, the Karlsruhe simulation model of the middle atmosphere (KASIMA) ([62], [63]). The resulting differences and agreements between model and measurement are described and commented.

Additionally, meteorological parameters, like backward trajectories or tropopause height, are applied to interpret the measured data. The trace gas distributions for a subtropical stratosphere influenced by polar and tropical airmasses are examined in the form of a case study. The correlations found between the measured data and both the height of the tropopause and the origin of the airmasses demonstrate the importance of transport processes for the short-term variations observed in the column amounts and profiles.

Chapter 2

The Atmosphere

2.1 Composition and Thermal Structure of the Earth's Atmosphere

The Earth's atmosphere consists of a mixture of gases, mostly molecular nitrogen (78% by volume) and molecular oxygen (21% by volume). Water vapor, carbon dioxide, and ozone, along with other minor constituents, comprise the remaining 1% of the atmosphere. Although they appear in very small amounts, these trace species play a key role in atmospheric processes. Water vapor is involved in radiation processes, cloud formation, and in the exchange of energy with the oceans. It is confined almost exclusively in the troposphere. Ozone plays a key role in supporting life at the Earth's surface. By intercepting harmful UV radiation, ozone allows life to exist. The evolution of the Earth's atmosphere and the formation of the ozone layer are thought to be closely related to the development of life on Earth. Its volume mixing ratio reaches a maximum at about 32 km, forming the so-called ozone layer. Atmospheric trace gases are generally created and destroyed in certain regions and are involved in global transport processes. Depending on their lifetime they are highly variable both spatially and temporally. Thus, for understanding the distribution of the trace gases in the atmosphere, it is crucial to consider both their chemistry and the dynamics of the atmosphere.

Suspensions of liquid and solid particles (atmospheric aerosols) are also present in the atmosphere. Aerosols serve as condensation nuclei for water droplets and ice crystals, which do not form readily in their absence. Hence they are vital to cloud formation. Since aerosols scatter solar radiation at visible wavelength regions and absorb infrared radiation, they are involved in the energy balance of the Earth. They are also crucial to heterogeneous chemical processes, i.e. chemical reactions that require the presence of multiple phases. The activation of ozone-destroying halogen components, which takes place on the surface of cloud particles, plays a key role in
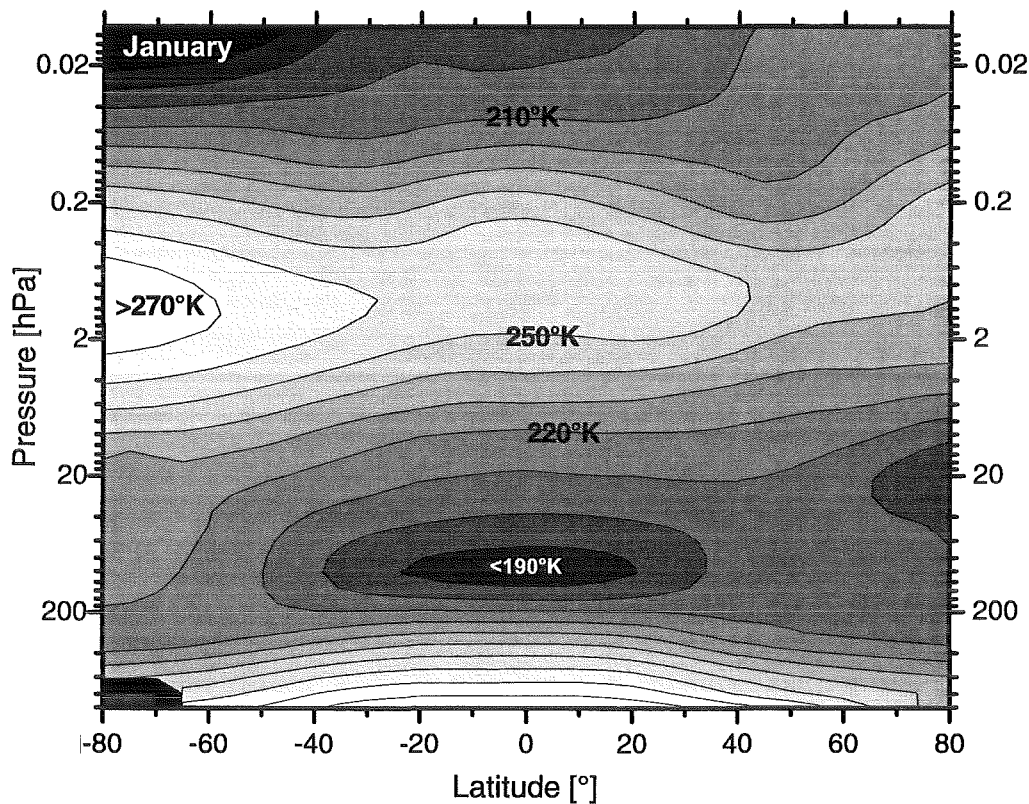
Fig. 2.1: Zonal mean atmospheric temperature profile for January ([55]).

the formation of the Antarctic ozone hole. Aerosols are produced both naturally as dust, sea salt, or volcanic debris and anthropogenically through combustion and industrial processes. For a summary of the composition of the Earth's atmosphere see table 2.1.

The Earth's atmosphere is commonly described as a series of layers defined by their thermal characteristics. Each layer is a region where the change in temperature relative to altitude has a constant sign. The layers are called "spheres" and the boundaries between them are the "pauses". The troposphere is vertically well-mixed because of the negative temperature gradient. Temperature and location of the tropopause vary with latitude and season. At the equator, its mean altitude is near 17 km and the corresponding temperature is about 190 K, while in polar regions its elevation is about 8 km only and the temperature roughly is 220 K. In contrast to the troposphere, the stratosphere is characterized by a stable layering, i.e. only weak vertical motions exist (reduction of vertical turbulent transport). This is due to the increase of temperature with height in this layer. The positive temperature gradient is a result of ozone heating, which is due to the absorption of solar ultravi-

Con- stitu- ent	Typical mixing ratio	Vertical distribution	Controlling processes
N_2	0.7808	homogeneous	vertical mixing
O_2	0.2905	homogeneous	vertical mixing
H_2O	$\leq 0.030^t$	decreases sharply in troposphere; increases in stratosphere; highly variable	evaporation, condensation, transport; production by CH_4 oxidation
Ar	0.0093	homogeneous	vertical mixing
CO_2	370ppmv	homogeneous	vertical mixing; production by surface and anthropogenic processes
O_3	10ppmv^s	increases sharply above tropopause; maximum at 32 km	photochemical production in stratosphere; transport; destruction at surface (in absence of high NO levels)
CH_4	1.7ppmv^t	homogeneous in troposphere; decreases in stratosphere	production by surface processes; oxidation produces H_2O
N_2O	350ppbv^t	homogeneous in troposphere; decreases in stratosphere	production by surface and anthropogenic processes; dissociation in middle atmosphere produces NO; transport
CO	70ppbv^t	decreases in troposphere; increases in stratosphere	production anthropogenically and by oxidation of CH_4; transport
NO	10ppbv^s	increases vertically	production by dissociation of N_2O and anthropogenically; catalytic destruction of O_3
HCl	2.5ppbv^s	increases sharply in stratosphere	heterogenic reactions; transport
HF	1.5ppbv^s	increases sharply in stratosphere	transport
HNO_3	8ppbv^s	increases in stratosphere; pronounced maximum around 25 km	transport; photodissociation; heterogenic reactions
NO_2	4ppbv^s	increases in stratosphere; maximum around 30 km	transport; photodissociation
$ClONO_2$	0.8ppbv^s	increases above troposphere; maximum around 25 km	transport; photodissociation; heterogeneous reactions
aerosol	$0.025\,\mu g/m^{3\,s}$	decrease with height in troposphere; stratospheric maximum around 20 km (Junge layer)	production anthropogenically, dispersion of dust, sea salt particles, volcanic eruptions; sedimentation

Table 2.1: Composition of the atmosphere. Index ^{t} indicates tropospheric and index ^{s} stratospheric values.

olet radiation by ozone. The stratopause lies at an altitude of about 50 km with a temperature of 270 K. In the mesosphere ozone heating is reduced and the temperature decreases with height up to the mesopause at about 85 km. Temperatures once again increase in the thermosphere, where energetic solar radiation is absorbed. A zonally averaged temperature distribution is shown in Figure 2.1.

2.2   Fundamental Description of Atmospheric Dynamics

To describe the theoretical dynamic and thermal behavior of the atmosphere, the fundamental equations of fluid mechanics must be employed. The dynamics of the Earth's atmosphere is governed by three basic principles. These are Newton's laws of motion, the conservation of energy, and the conservation of mass.

First we will use Newton's second law which describes the response of a fluid to external forces:

$$\frac{\mathrm{d}\vec{v}}{\mathrm{d}t} + \underbrace{\frac{1}{\rho}\nabla p}_{pressure\ gradient\ force} + \overbrace{2\vec{\Omega}\times\vec{v}}^{Coriolis\ force} = \underbrace{\vec{g}}_{gravitational\ force} + \overbrace{\vec{F}}^{frictional\ forces} \qquad (2.1)$$

where $\vec{v}$ represents the vector speed of an air parcel, p is the pressure, ρ the mass per unit volume, $\vec{\Omega}$ is the angular rotation rate of the Earth, $\vec{g}$ is the gravitational acceleration, $\vec{F}$ is the frictional force due to viscosity, and t is the time. See, for example, [29] for a detailed physical explanation of each of these terms.

A further basic principle is the conservation of energy (first law of thermodynamics):

$$c_p \frac{\mathrm{d}T}{\mathrm{d}t} - \frac{1}{\rho}\frac{\mathrm{d}p}{\mathrm{d}t} = Q \qquad (2.2)$$

where T is the temperature, c_p represents the specific heat of air at constant pressure, and Q is the net heating rate per unit mass. In the stratosphere and mesosphere, this rate is principally due to the difference between heating by absorption of ultraviolet radiation by ozone and cooling by infrared emission by ozone, CO_2, and water vapor and, thus, depends on the distributions of several important minor constituents. For adiabatic (energy-conserving) processes the net heating rate remains zero and the two left terms express the inverse relationship between pressure and temperature, i.e. cooling through expansion and heating through compression.

Finally, we consider the conservation of mass (equation of continuity). It is described by:

$$\frac{d\rho}{dt} + \rho \, \nabla \cdot \vec{v} = 0 \tag{2.3}$$

Hydrostatic Approximation

That part of equation 2.1, which refers to the z-component, can be simplified considerably if we only consider the two dominant terms, which are the pressure gradient and gravitational force:

$$\frac{1}{\rho} \frac{\partial p}{\partial z} + g = 0 \tag{2.4}$$

This equation is called the hydrostatic approximation. Substitution in 2.4 of ρ together with the ideal gas law yields:

$$\frac{dp}{p} = -\frac{m \, g}{k_B \, T} dz = \frac{dz}{H} \tag{2.5}$$

where $H = k_B \, T / m \, g$ is called the scale height and k_B is the Boltzmann's constant. Integration of equation 2.5 gives a relation between height and pressure:

$$p(z) = p_0 \, e^{\int_0^z \frac{dz'}{H(z')}} \tag{2.6}$$

The atmospheric scale height $H(z)$ depends on z, mainly due to its temperature dependence. It is roughly $7 \pm 1\,$km below 80km. The scale height represents the altitude which corresponds to a reduction by $1/e$ in pressure.

Potential Temperature

The net radiative heating Q is the only source of external forcing in the energy conservation equation (2.2). Assuming $Q = 0$, we can examine the thermodynamics of adiabatic air parcel displacements. The energy conservation equation changes to:

$$c_p \frac{dT}{dt} = \frac{1}{\rho} \frac{dp}{dt} \tag{2.7}$$

Use of the ideal gas law and integration provides a relation between the actual temperature T and the so-called potential temperature Θ, which represents a temperature attained by an air parcel if it was adiabatically compressed or expanded to a pressure p_0, starting from a defined actual temperature T and a pressure p:

$$\Theta = T \left(\frac{p_0}{p}\right)^{\frac{R}{c_p}} \tag{2.8}$$

with $R/c_p = 0.286$ for dry air. Since Θ is a conservative variable in adiabatic displacements, air parcels that do not receive any net heating, cooling or latent heat can only move along isentropic surfaces (surfaces with the same potential temperature).

Geostrophic Wind Equation

For typical wind speeds and scales observed in the atmosphere, all terms in equation 2.1 are small compared to the pressure gradient and Coriolis acceleration. Additionally, the vertical wind component is small compared to the horizontal components. As a good approximation, winds will therefore blow according to a balance between pressure gradient and Coriolis acceleration. This balance is called geostrophic balance. Expression in spherical coordinates (φ for latitudinal degrees and ϑ for longitudinal degrees) yields:

$$f\,v \;=\; \frac{1}{\rho\,a\,\cos\varphi}\,\frac{\partial p}{\partial\vartheta} \tag{2.9}$$

$$f\,u \;=\; \frac{1}{\rho\,a}\,\frac{\partial p}{\partial\varphi} \tag{2.10}$$

using the Coriolis parameter $f = 2\,\Omega\,\sin\varphi$, also called planetary vorticity, and the approximation $r \approx a$ with r being the distance from the center of the Earth and a the Earth's radius ($r = a + z$).

An alternative version of the geostrophic balance can be obtained by differentiating 2.9 and 2.10 with respect to z and substituting the hydrostatic approximation (equation 2.4):

$$f\,\frac{\partial v}{\partial z} \;=\; \frac{R}{H}\,\frac{1}{\rho\,a\,\cos\varphi}\,\frac{\partial T}{\partial\vartheta} \tag{2.11}$$

$$f\,\frac{\partial u}{\partial z} \;=\; -\frac{R}{H}\,\frac{1}{\rho\,a}\,\frac{\partial T}{\partial\varphi} \tag{2.12}$$

These are the thermal wind equations which state that the vertical shear of the horizontal wind field is proportional to the horizontal temperature gradient.

Potential Vorticity

A very useful parameter in atmospheric dynamics is the potential vorticity, also called Ertel potential vorticity (EPV) or isentropic potential vorticity:

$$\mathrm{EPV} = \frac{\zeta_\Theta + f}{-\frac{1}{g}\frac{\partial p}{\partial\Theta}} \tag{2.13}$$

where ζ_Θ is the relative vorticity, i.e. the vorticity with respect to the Earth's surface, evaluated on a certain isentropic level. Equation 2.13 is derived from the horizontal momentum equation 2.1, neglecting friction and assuming adiabatic motions. The Ertel potential vorticity is conserved under inviscid diabatic conditions. It is a dynamic tracer of horizontal motion.

2.3 Atmospheric Transport

In this section we describe spatially and temporally averaged motions, emphasizing stratospheric circulation. The tropospheric global-scale averaged circulation is only described shortly, for more details see e.g. [29]. We also mainly concentrate on the subtropical region and its particularities in terms of atmospheric transport.
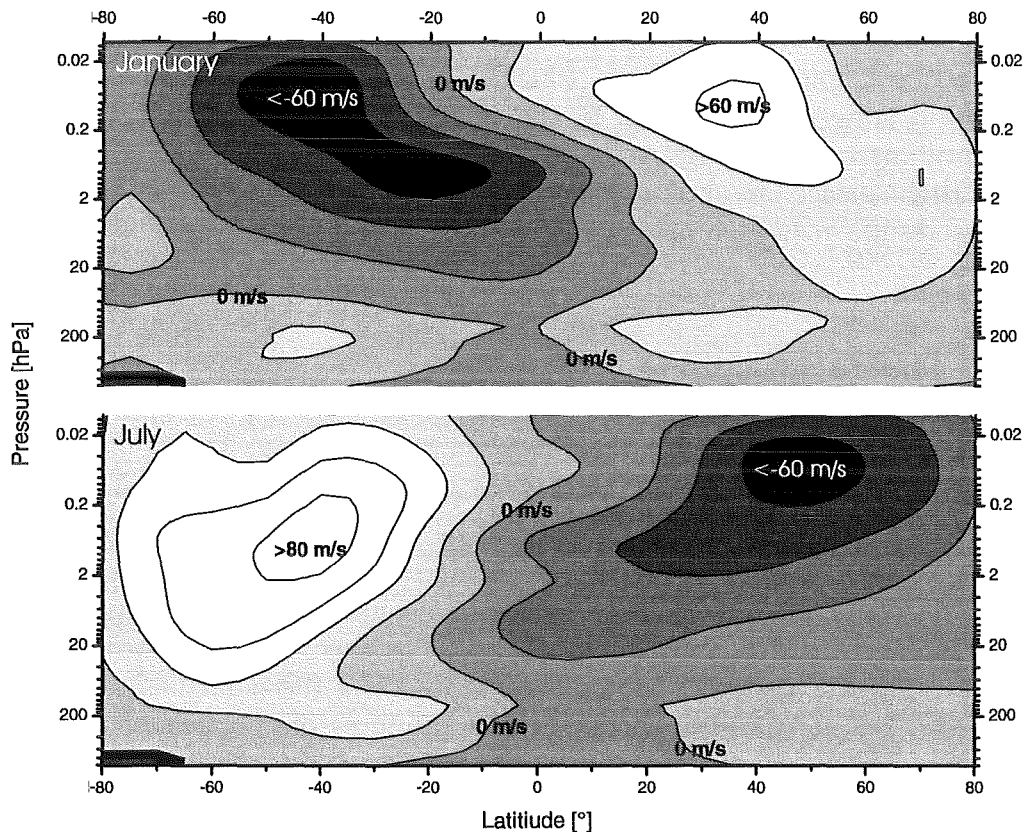
Fig. 2.2: Zonal winds in January and July. Dark means westward wind (given in negative values), bright means eastward wind (positive values)([55]).

2.3.1   The Troposphere

In the troposphere at low latitudes, i.e. when the Coriolis force is weak, the pressure gradient force is the leading term in equation 2.1. Up to approximately 35° latitude, general motions are determined by the Hadley circulation which is a thermally direct circulation. High latent heat release causes air to rise inside the Inner Tropical Convergence Zone (ITCZ). The result is low surface pressure and high pressure in the tropopause region, which leads to poleward flow in the height and equatorward flow at the surface and, as a consequence, to downward motions in the subtropical regions (30°-35° latitude), where this subsiding air is responsible for the dry climates found at those latitudes. The resulting subsidence inversion is a great benefit of the Izaña Observatory, since it provides clear sky conditions nearly all days per year. At the surface, the equatorward air flow is weakly deflected westward by the Coriolis force, producing the northeast (northern hemisphere) and southeast (southern hemisphere) passat winds. At higher latitudes, thermal winds which are a geostrophic balance between pressure gradient and Coriolis force (see equations 2.11 and 2.12), provide for an eastward flow. Asymmetries which deflect air meridionally are responsible for poleward transport processes. In the troposphere these deflections are caused by synoptic disturbances. Above the poles (up to approximately 3 km) easterlies prevail. High surface pressure at poles, caused by low temperatures over the huge ice planes, results in an equatorward flow which is deflected westwards by the Coriolis force.

2.3.2   The Stratosphere

Zonal Circulation

In Figure 2.2, mean values of the zonal wind component (wind in latitudinal direction) are shown. This wind component can be explained by the geostrophic wind equations 2.11 and 2.12, as can be seen by comparison of Figures 2.1 and 2.2. In the winter hemisphere, ozone heating establishes an equatorward temperature gradient over a deep layer, which, by the thermal wind balance, produces strong westerly flow. Stratospheric westerlies intensify upwards along the polar night terminator, where ozone heating vanishes abruptly. This produces the polar night jet and the circumpolar vortex. In the summer hemisphere, a poleward gradient of heating, which results from the distribution of daily insolation, produces a deep temperature gradient of the opposite sense and strong easterly circumpolar flow. Due to the strong zonal easterlies and westerlies, transport along the longitudinal direction is relatively rapid compared to the chemical lifetime of the trace gases. Thus, trace gases may be considered well-mixed in the zonal direction.

Meridional Circulation

In latitudinal direction, trace gases are far from being distributed uniformly. Before the appearance of the "ozone hole", for example, ozone reached its highest column amounts in polar regions in winter/spring with values of about 450 DU, whereas typical values for tropical latitudes are around 260 DU. Nevertheless, its maximum of production is found in the tropical upper stratosphere, due to highest ultraviolet insolation. Dobson argued that this indicates important transport processes from the tropical stratosphere to the polar stratosphere ([15]). Brewer came to a similar conclusion by considering the stratospheric distribution of water vapor ([5]). Both suggested rising motions in the tropics, poleward transport from the tropical stratosphere to mid-latitudes, and descent at high latitudes. This zonally averaged circulation scheme is often referred to as Brewer-Dobson circulation. It is indicated by the big open arrows in Figure 2.3. It is driven by mechanical disturbances (e.g. Gravity and Rossby waves, indicated by wavy arrows in Figure 2.3), which force the atmosphere out of radiative equilibrium. These disturbances are stronger in the northern hemisphere, due to larger orographic forcing, and in winter when there are westerlies throughout the troposphere and stratosphere (no blocking of planetary wave propagation by stratospheric easterlies). As a consequence, air descends in regions where diabatic net cooling occurs and ascends where diabatic net heating is present. The horizontal motions are then consequences of the continuity equation.
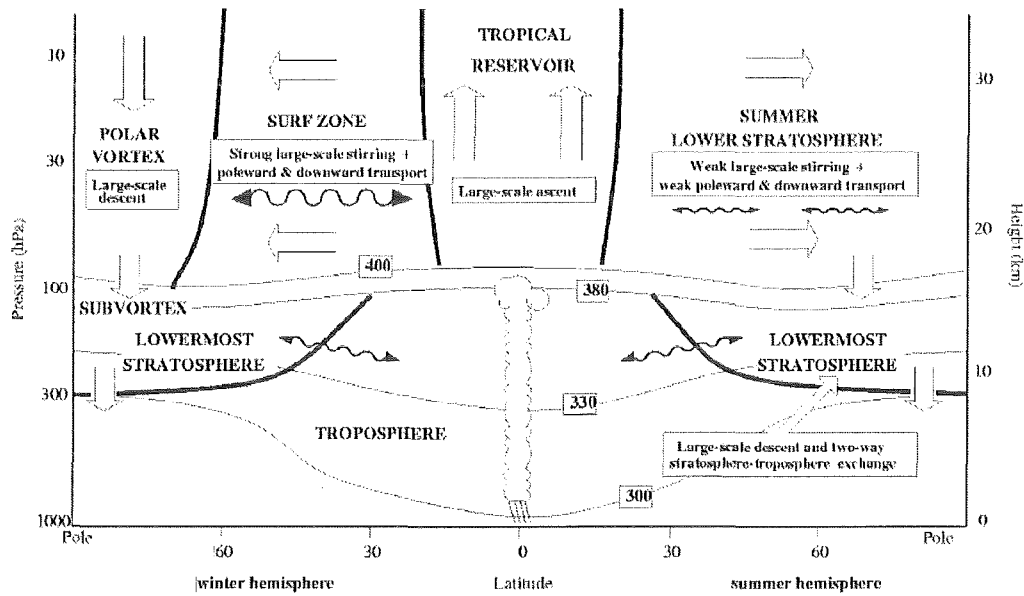
Fig. 2.3: Schematic diagram showing the pattern of transport and mixing in the troposphere and stratosphere (adopted from [28]): Visible are isentropic surfaces, labelled by their potential temperature (thin lines); transport due to the zonally averaged diabatic circulation, also known as Brewer-Dobson circulation (big arrows); eddy transport along isentropic surfaces (wavy arrows); the stratosphere above 400 K is divided into three different regions for the winter hemisphere, which are polar vortex, surf zone, and tropical reservoir, and two regions for the summer hemisphere, which are tropical reservoir and extratropics, by eddy transport barriers (thick lines); below 400 K the atmosphere is divided into lowermost stratosphere and troposphere by eddy transport barriers (thick lines) coincident with the tropopause, which is given by the 2 PVU isoline in the extratropics and by the 380 K isentrope in the tropics; the lowermost stratosphere is distinguished from the rest of the stratosphere by being accessible from the troposphere along isentropic surfaces.
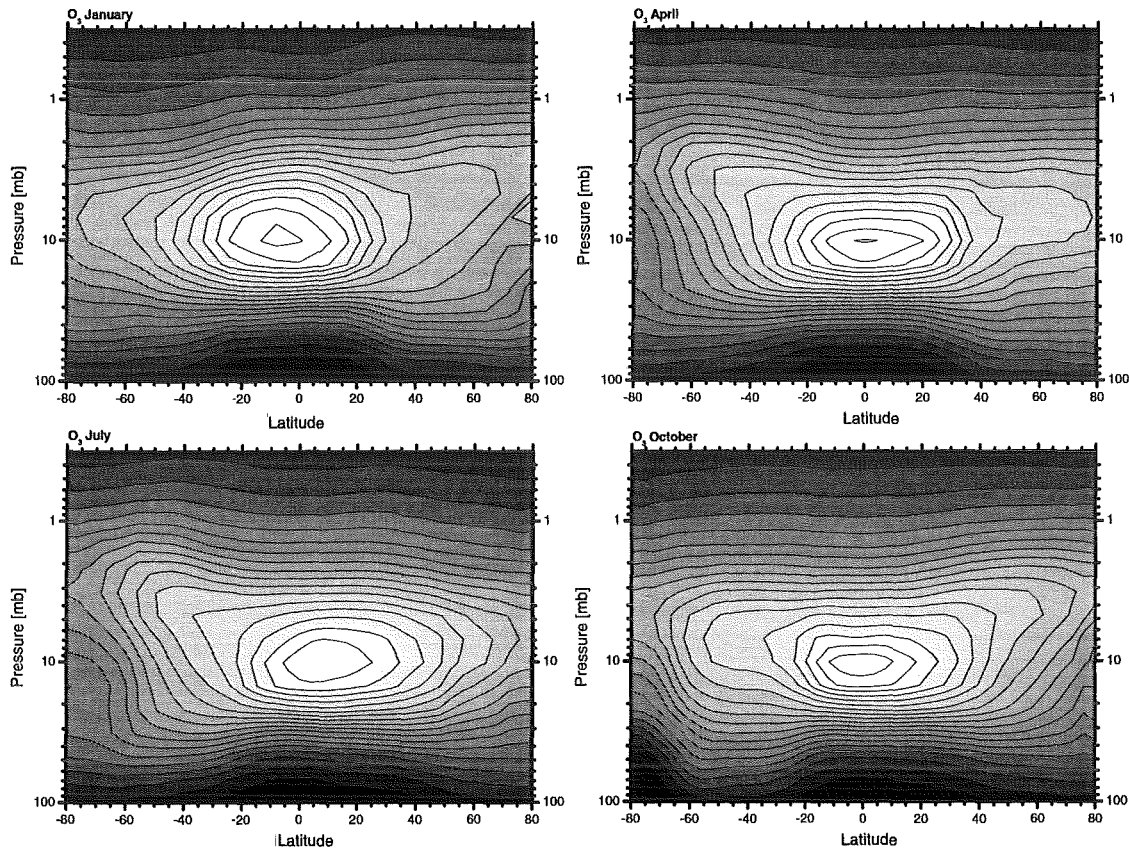
Fig. 2.4: Zonal mean latitude-height distribution of O_3. Data are taken from UARS and are mean values for January, April, July, and October. Scale is from 0.0ppmv (black) to 10.0ppmv (white) in steps of 0.5ppmv

Transport Barriers

The step gradients of potential vorticity at the edge of the polar vortex cause the inner vortex air to be isolated from the outer vortex air. This prevention of mixing is essential for the formation of the ozone hole. Observations suggest that there is a similar confinement of air within the tropics and that there are steep gradients of trace components at the edge of this "reservoir" (e.g. [20]). Studies with general circulation models show that in analogy to the polar vortex there exists an "eddy transport barrier" against isentropic transport in the subtropical region ([51], [28], see also Figure 2.3). Such barriers work via a combination of dynamic effects involving both horizontal shear and isentropic gradients of EPV ([36]). Figures 2.4 - 2.6 show zonal mean values for O_3, HF, and CH_4 as measured by UARS (Upper Atmospheric Research Satellite). While in particular Figure 2.4 demon-
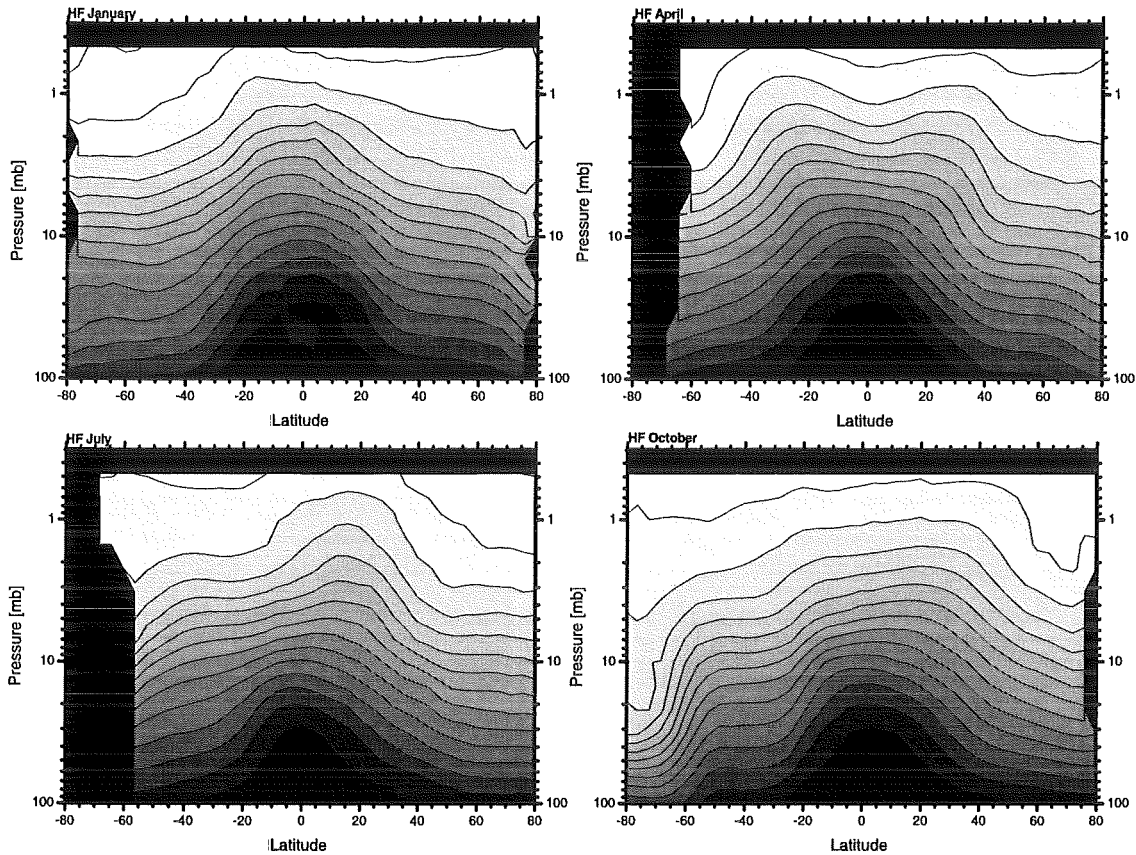
Fig. 2.5: Zonal mean latitude-height distribution of HF. Data are taken from
UARS and are mean values for January, April, July, and October. Scale
is from 0.0ppbv (black) to 1.6ppbv (white) in steps of 0.1ppbv.

strates the importance of transport for the distribution of trace gases (production
in tropics at approximately 10mb (30km), poleward transport, downward motion
at high latitudes), a mixing barrier between tropical and extratropical air becomes
visible, indicated by the sharp gradients in the distribution of HF and CH_4 in the
subtropoical region. Like the polar vortex, this subtropical barrier which is much
weaker in confining trace components than its counterpart at higher latitudes, un-
dergoes erosion with significant volumes of air transported to mid-latitudes. Those
transport processes appear to be associated with planetary wave activity in analogy
to transport processes across the edge of the polar vortex. This zonally asymmetric
wave perturbations are responsible for the mean meridional transport, as explained
before (see Figure 2.3). Events of tongues of air are observed by which the air
is transported from out of the tropics into middle latitudes. Such incidence have
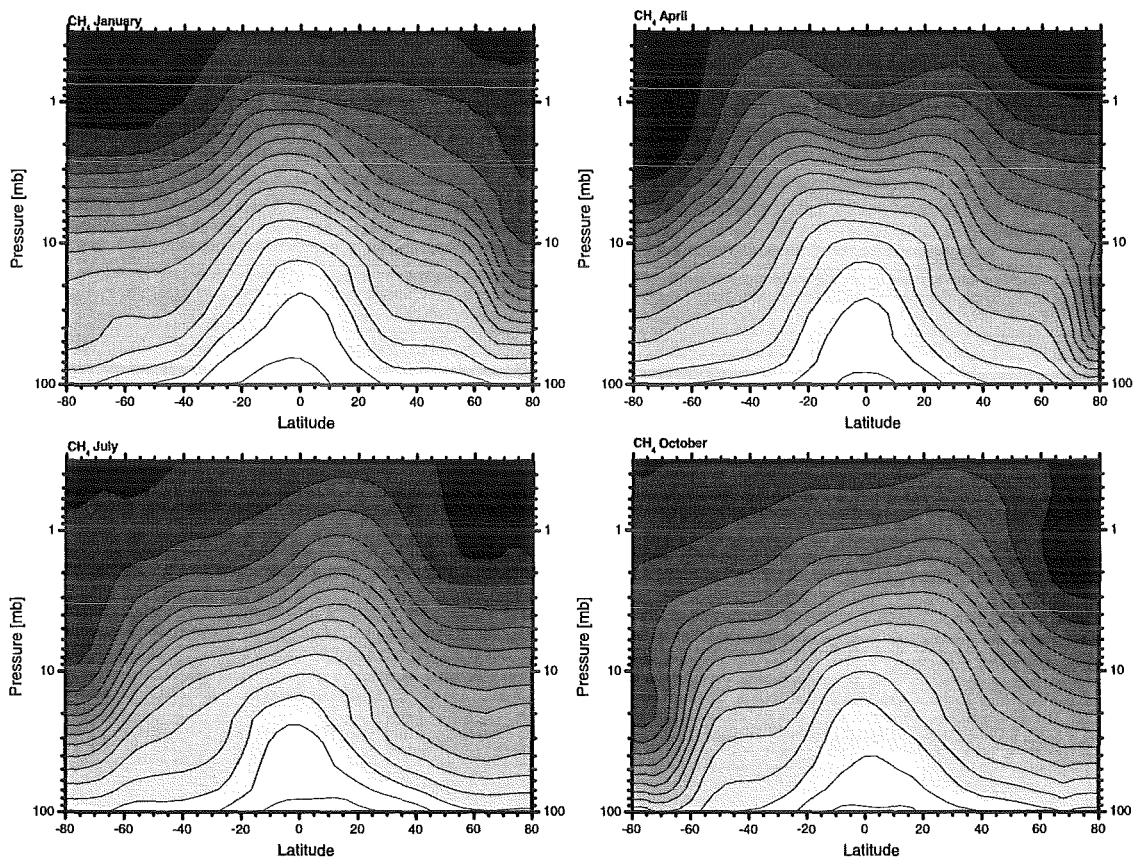
Fig. 2.6: Zonal mean latitude-height distribution of CH$_4$. Data are taken from
UARS and are mean values for January, April, July, and October. Scale
is from 0.0ppmv (white) to 1.8ppmv (black) in steps of 0.1ppmv

already been studied by model calculations ([54], [39]). Long-term measurements
performed in the subtropical regions, like those presented in this work, can there-
fore help to estimate the efficiency of those transport processes, determine their
frequency or interannual variability. In chapter 7 we will present such a tropical
streamer event detected in February 2001.

A further barrier preventing vertical transport is formed by the tropopause. In
the subtropics, the tropopause height changes abruptly from typically 17 km in the
tropics to 10 - 12 km at mid-latitudes (tropopause break). At the Izaña Observatory
the tropopause height therefore varies strongly. The 2 PVU dynamical tropopause
varies between 8 km and 16 km. Generally, in summertime when the atmosphere
is tropically influenced, a high tropopause prevails. Wintertime is characterized
by a strong variability. Since the subtropical tropopause cuts also steeply across

isentropic surfaces by ranging from near $380\,K$ in the tropics to 300-$330\,K$ in mid-latitudes, adiabatic stratosphere-troposphere exchange is possible. However, it will usually be inhibited by strong potential vorticity gradients (see Figure 2.3). Nevertheless, some transport across the tropopause is likely to occur ([30]). There already exists a study of these processes above the Izaña Observatory ([40]).

2.4   Stratospheric Chemistry

The simplest treatment of ozone photochemistry is attributed to Chapman [10]. Only a pure oxygen atmosphere was considered. The governing reactions are:

$$O_2 + h\nu \, (\lambda < 242\,nm) \quad \rightarrow \quad O + O \quad (J_2) \tag{2.14}$$

$$O + O_2 + M \quad \rightarrow \quad O_3 + M \quad (k_2) \tag{2.15}$$

$$O + O_3 \quad \rightarrow \quad 2\,O_2 \quad (k_3) \tag{2.16}$$

$$O_3 + h\nu \, (\lambda < 1140\,nm) \quad \rightarrow \quad O_2 + O \quad (J_3) \tag{2.17}$$
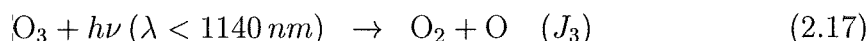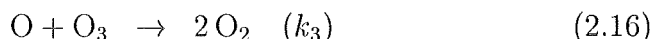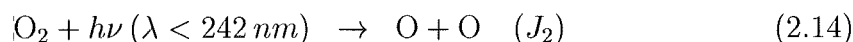
where the rate coefficients in parentheses characterize the speeds of the individual reactions. These reactions result in the equilibrium of ozone number density:

$$[O_3] = [O_2] \sqrt{\frac{k_2 \, J_2}{k_3 \, J_3}} \, [M] \tag{2.18}$$

These considerations already can qualitatively predict a maximum near $32\,km$. Starting at high altitudes, ozone production increases with decreasing heights due to rising O_2 amounts. Below the maximum, it decreases because the ultraviolet flux and, therefore, J_2 fall off sharply. But this simple consideration predict total ozone to minimize at high latitudes because ultraviolet flux and, hence, J_2 are small there, whereas observations show maximum values of the column amounts at high latitudes. This simple consideration also generally underestimate ozone number density in the lower stratosphere and overestimate it in the upper stratosphere. These discrepancies are attributed firstly to transport processes, as described in the preceding section, and secondly in neglecting additional chemical ozone-destroying cycles. In these cycles free radicals act catalytically, i.e. they remain unchanged while destroying ozone. The importance of a catalytic cycle is determined by the concentration of the involved radical, the reaction speeds, and the number of cycles that are possible during the lifetime of the radical. Detailed considerations of the efficiency of the respective cycles are shown in [43]. In those catalytic cycles the radical destroys ozone without being removed:

$$X + O_3 \quad \rightarrow \quad XO + O_2 \tag{2.19}$$

$$XO + O \quad \rightarrow \quad X + O_2 \qquad (2.20)$$
$$\text{net}: O + O_3 \quad \rightarrow \quad 2\,O_2 \qquad (2.21)$$

with OH [23], NO [13], Cl [71], or Br [76] acting as radical X. Additionally, cycles exist which combine various of the above-mentioned cycles ([16], [35]). Precursor molecules of the radicals generally originate from the Earth's surface, and by photodissociation they transform into reactive radicals in the stratosphere. CH_4 and H_2O, for example, can be converted into OH, and N_2O into NO. Both CH_4 and N_2O are produced in enormous quantities by microorganisms. Cl and Br are produced from anthropogenically injected CFCs and halons. Holding cycles also are of a certain importance to the ozone balance. The radicals or molecules crucial to the catalytic cycles are held back from their cycles by forming reservoir compounds which are rather unreactive. Important reservoir compounds are $ClONO_2$, HCl, HNO_3, N_2O_5, and HO_2NO_2. They control the availability of important ozone destroying radicals by the following cycles:

$$ClO + NO_2 + M \quad \rightarrow \quad ClONO_2 + M \qquad (2.22)$$
$$ClONO_2 + h\nu \quad \rightarrow \quad Cl + NO3 \qquad (2.23)$$

$$CH_4 + Cl \quad \rightarrow \quad CH_3 + HCl \qquad (2.24)$$
$$HCl + OH \quad \rightarrow \quad H_2O + Cl \qquad (2.25)$$

$$NO_2 + OH + M \quad \rightarrow \quad HNO_3 + M \qquad (2.26)$$
$$HNO_3 + OH \quad \rightarrow \quad H_2O + NO_3 \qquad (2.27)$$
$$HNO_3 + h\nu \quad \rightarrow \quad OH + NO_2 \qquad (2.28)$$

$$NO_2 + O_3 \quad \rightarrow \quad NO_3 + O_2 \qquad (2.29)$$
$$NO_2 + NO_3 + M \quad \rightarrow \quad N_2O_5 + M \qquad (2.30)$$
$$N_2O_5 + h\nu \quad \rightarrow \quad NO_3 + NO_2 \qquad (2.31)$$
$$NO_3 + h\nu \quad \rightarrow \quad NO_2 + O \qquad (2.32)$$

$$HO_2 + NO_2 + M \quad \rightarrow \quad HO_2NO_2 + M \qquad (2.33)$$
$$HO_2NO_2 + h\nu \quad \rightarrow \quad HO_2 + NO_2 \qquad (2.34)$$
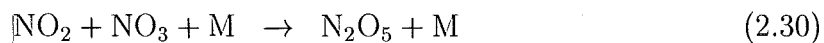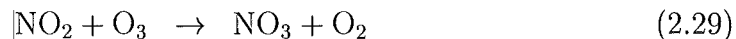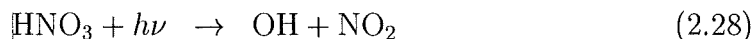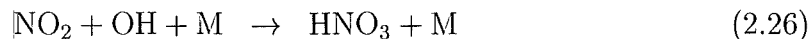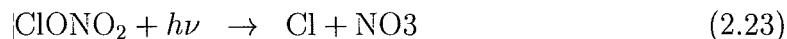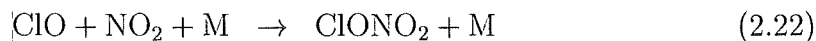
The chemical reactions considered so far involve species in the gas phase only. Consequently, slightly increased depletions due to anthropogenic CFC release might be expected. Also aircraft NO_x and water vapor (H_2O is a precursor of the ozone-

destroying OH radical) emissions are thought to influence the ozone balance. However, pure gas-phase chemistry cannot explain the spectacular ozone depletion observed in the Antarctic spring ([16]). Especially since this great depletion is observed at latitudes, where ozone is thought to be photochemically inert, because of the small ultraviolet fluxes. The key to understanding the ozone hole lies in the presence of solid phase in the stratosphere, which is normally excluded by the very low mixing ratio of water vapor. In the cold winter polar stratosphere, Polar Stratospheric Clouds (PSC) provide the solid phase necessary for important heterogeneous reactions:

$$ClONO_2(g) + HCl(a) \quad \rightarrow \quad Cl_2(g) + HNO_3(a) \qquad (2.35)$$

$$ClONO_2(g) + H_2O(a) \quad \rightarrow \quad HOCl(g) + HNO_3(a) \qquad (2.36)$$

$$N_2O_5(g) + H_2O(a) \quad \rightarrow \quad 2\,HNO_3(a) \qquad (2.37)$$

$$N_2O_5(g) + HCl(a) \quad \rightarrow \quad HNO_3(a) + ClNO_2(g) \qquad (2.38)$$
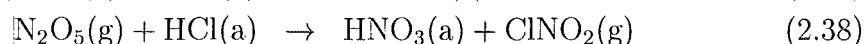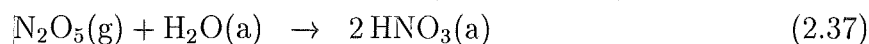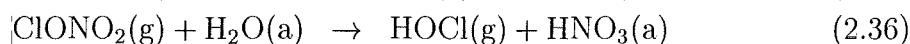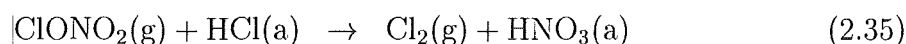
where (g) stands for a molecule in the gas phase and (a) for a molecule adsorbed on a particle's surface. It is evident that these reactions cause Cl_2, $HOCl$, and $ClNO_2$ to be released from their reservoirs of $ClONO_2$ and HCl. The respective stratospheric region is then "pre-conditioned" for ozone depletion. As soon as the sun rises in spring, those gases (Cl_2, $HOCl$, and $ClNO_2$) undergo photolysis and release the chlorine radical:

$$Cl_2 + h\nu \quad \rightarrow \quad Cl + Cl \qquad (2.39)$$

$$HOCl + h\nu(\lambda < 301nm) \quad \rightarrow \quad ClO + H \qquad (2.40)$$

$$HOCl + h\nu(\lambda < 503nm) \quad \rightarrow \quad Cl + OH \qquad (2.41)$$

$$ClNO_2 + h\nu \quad \rightarrow \quad Cl + NO_2 \qquad (2.42)$$

The chlorine radical is then responsible for the ozone hole via its catalytic cycle. While converting reservoir species of chlorine into reactive Cl_x, the reactions 2.35 - 2.38 have the opposite effect on reactive nitrogen. It is converted into relatively inactive HNO_3 and removed from the gas phase (denoxification). If the particles become large enough to undergo sedimentation, nitrogen is removed extensively. This process is known as denitrification. A denitrified stratosphere then supports large ozone destruction, since a transformation of the chlorine radical into the reservoir $ClONO_2$ according to reaction 2.22 is avoided. Reaction 2.24 could also deactivate chlorine, but it is much slower than the chlorine catalytic cycle. Hence, it only becomes important, if ozone is nearly completely destroyed. This only happens in the Antartic winter/spring.

Recently, heterogeneous reactions on background sulfate aerosol or carbon aerosol, in analogy to reactions on PSC, were discussed ([69], [44]). Those reactions would not be restricted to a very cold stratosphere, they could take place at all latitudes and, hence, they may partly serve as an explanation of the ozone decline at lower latitudes.

Chapter 3

The Fourier Transform Infrared (FTIR) Spectrometer

FTIR spectroscopy allows to detect a great variety of atmospheric constituents simultaneously and various aircraft-, balloon-, or ground-based measurements have already been performed by the Institute of Meteorology and Climate Research (IMK) ([17]). The here analyzed measurements were performed with a high-resolution FTIR spectrometer manufactured by the Bruker company (IFS 120M), which had already measured for some years in Kiruna ([4]). They were conducted ground-based using a container on the Izaña Observatory (IZO) on the Canary Island of Tenerife. Since direct sunlight spectra were analyzed, a solar tracker was needed. This device was mounted on the roof of the container. In this Chapter the instrument assembly is described. We will also give a principle insight into the data processing involved in Fourier transform spectroscopy.

3.1 Instrument Assembly

3.1.1 Optics

The route of the radiation through the whole instrumental assembly, i.e. coupling unit and spectrometer, shall be described (Figure 3.1). Direct sunlight is captured by the solar tracker which consists of two rotation stages. The mirror mounted on the first stage reflects the sun beam horizontally, i.e. it transforms the elevation of the sun into a horizontal plane. The second stage's mirror is responsible for the remaining azimuth correction of the sun ray. It also reflects the beam perpendicularly that means downward into the container. The sun tracker is controlled by a combination of astronomical calculations and a quadrant detector. During clear sky conditions, the quadrant detector decides mainly on the sun tracker's movements. If
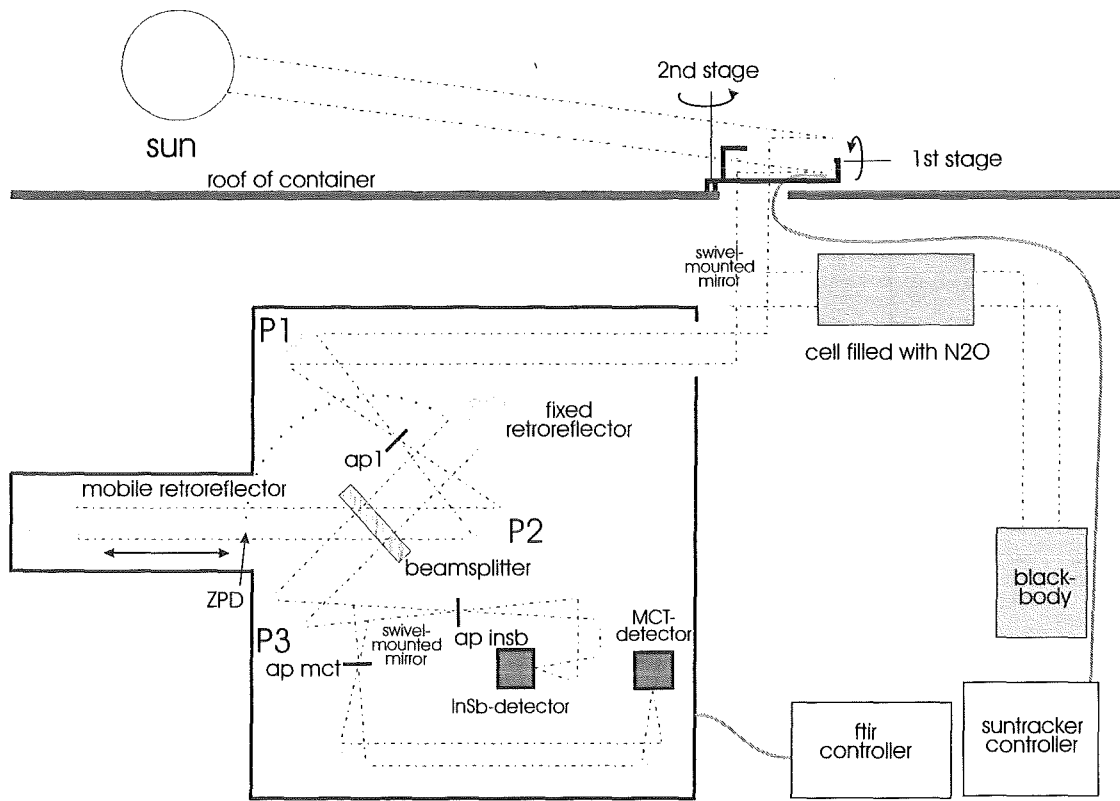
Fig. 3.1: Schematic representation of the instrument's optical devices.

its signal is lower than a certain threshold value, e.g. due to a sun masked by clouds, the astronomical calculations will be used for tracking. For more details concerning the sun tracker see [32].

Instead of sunlight, a laboratory source can be used by inserting a swivel-mounted mirror. This allows to calibrate the instrument by means of a black body. The instrumental line shape is also determined regularly with the black body radiation additionally passing a low-pressure gas cell filled with N_2O [26].

Another mirror inside the container reflects the beam perpendicularly, allowing the sun ray to enter the spectrometer in a horizontal plane.

Inside the spectrometer, a parabolic mirror (P1) focuses the beam on the aperture (ap1). The aperture limits the field of view, which ensures that only light emitted from the center of the solar disc will be considered. The downstream mirror (P2) also is a parabolic one and retransforms the bundle of light into parallel rays. The essential piece of the actual FTIR spectrometer is the Michelson interferometer. The Michelson interferometer consists of a beamsplitter which divides the incoming light into two beams. One of them is reflected by a fixed retroreflector, while the other one
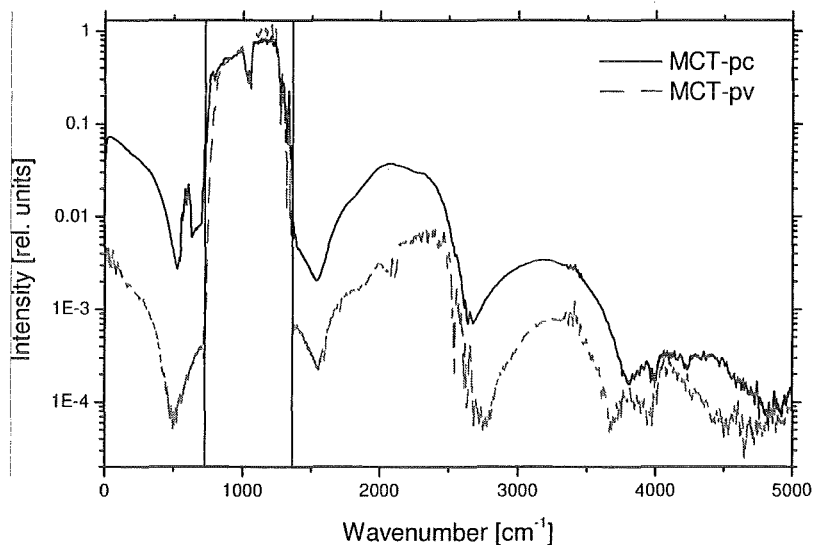
Fig. 3.2: Effect of the nonlinearity of photoconductive MCT (MCT-pc; solid line)
and of photovoltaic MCT (MCT-pv, dashed line). Marked wavenumber
interval indicates working interval of detector ($725\text{-}1355\,\mathrm{cm}^{-1}$).

is sent to a moving retroreflector, causing a variable optical path difference (OPD).
At the beamsplitter, they recombine and interfere according to their wavelength and
OPD. The recombined beam is collimated by a parabolic mirror (P3) to pass another
aperture (ap MCT, or ap InSb) and finally focused on one of the two detectors. A
swivel-mounted mirror is positioned depending on the detector to be illuminated.
Two detectors are used. Together, they cover the wavenumber range from 700 to
$4200\,\mathrm{cm}^{-1}$. At the detector, the intensity of the interfering beam is measured as a
function of OPD. The result is an interference pattern, the so-called interferogram.

3.1.2 Detectors

For the wavenumber range from 700 to $1400\,\mathrm{cm}^{-1}$ two different mercury-cadmium-
telluride (MCT) detectors were used between February 1999 and July 2001. Until
August 1999, a detector consisting of a photoconductive (pc) element was applied.
From August 1999 to January 2000, an MCT photodiode (MCT-pv) of Kolmar
Technologies was used. Once again, from February 2000 the photoconductive de-
tector was used until the end of March 2000, when the still measuring MCT-pv was
reinserted. Whereas a photoconductive working detector shows nonlinearity ([8]),
photodiodes work nearly linearly. The nonlinearity produces unreal artifacts in the
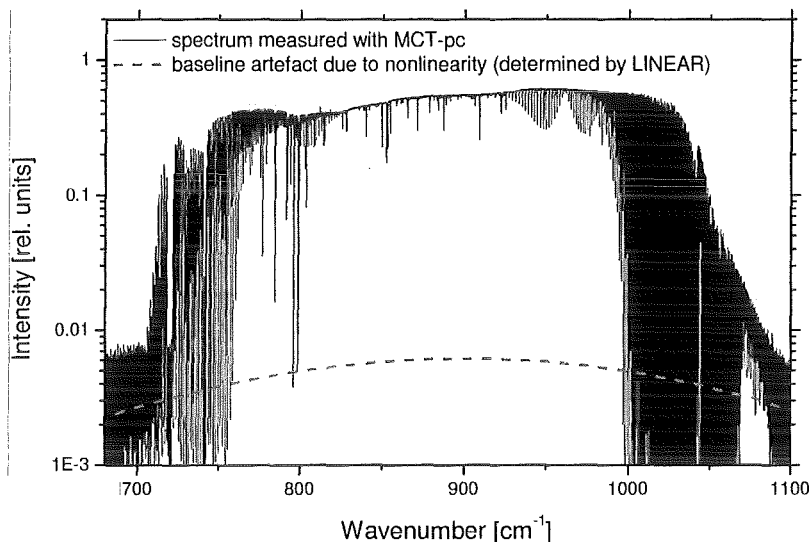
Fig. 3.3: Baseline correction of a MCT-pc spectrum covering 700-1100 cm^{-1}.

spectrum at a wavenumber of 0 cm^{-1} and at the double, triple, etc... wavenumber of the real wavenumber range. But also to the real wavenumber range, an artificial baseline is added. The size of those artifacts increases with increasing nonlinearities. In Figure 3.2, smoothed spectra recorded with the photoconductive MCT and the photovoltaic MCT are shown. The artifacts of the MCT-pc exceed those of the MCT-pv by one order of magnitude. The nonlinearities of the photoconductive MCT were corrected by the software LINEAR ([27]). In Figure 3.3, a spectrum measured on 20/3/00 at a solar zenith angle (SZA) of approximately 35° and the calculated artificial baseline are shown. All spectra measured with the MCT-pc in this work were corrected with such a calculated arteficial baseline. A disadvantage of the photodiodes (MCT-pv detectors) is that they have a slightly larger cutoff wavenumber, i.e. they are more limited towards longer wavelengths.

For the wavenumber range between 1800 and 4200 cm^{-1} an indium-antimonide (InSb) detector was applied.

3.2 Spectra Acquisition

In contrast to dispersive spectroscopy, Fourier transform (FT) spectroscopy does not produce the desired spectral data directly. In this section, the interrelation between the Fourier spectrometer's raw data (the interferogram) and the final spectrum is

illustrated.

3.2.1 Fourier Transformation

The intensity of the recombined beams as a function of the mirror displacement $I(x)$ must be converted into a spectrum by means of a mathematical operation called Fourier transformation. For simplification, we will first consider the case of a monochromatic radiation source. The interferometer produces and recombines two wave trains with a relative phase difference, depending on the mirror displacement. These partial waves interfere constructively, yielding a maximum detector signal, if their optical path difference is an exact multiple of the wavelength λ, i.e. if

$$2\,x = n\,\lambda \;\; (n = 0,\, 1,\, 2,\, ...) \tag{3.1}$$

Minimum detector signal and destructive interference occur, if $2\,x$ is an odd multiple of $\lambda/2$. The complete dependence of $I'(x)$ on x is given by a cosine function:

$$I'(x) = S'(k) \, \cos\,(2\,\pi\,k\,x) \tag{3.2}$$

where we used $k = 1/\lambda$ which is more common in FT spectroscopy, and $S'(k)$ is the intensity of the monochromatic line located at wavenumber k. Relation 3.2 is extremely useful for practical applications. In addition to the analyzed radiation the monochromatic light of an He-Ne laser is coupled into the interferometer. Its interference pattern according to relation 3.2 allows to determine the actual optical path difference with high precision.

In case of a polychromatic radiation source, we have to integrate over all monochromatic contributions:

$$I(x) = \int\limits_{k=-\infty}^{\infty} S(k) \, \cos\,(2\,\pi\,k\,x)\mathrm{d}k \tag{3.3}$$

This equation demonstrates that the interferogram $I(x)$ is nothing but the Fourier transformation of the spectrum. The inverse Fourier transformation allows to derive the spectrum $S(k)$ from the interferogram:

$$S(k) = \int\limits_{x=-\infty}^{\infty} I(x) \, \cos\,(2\,\pi\,k\,x)\mathrm{d}x \tag{3.4}$$

The last two equations give a good principle insight into the mathematical operations involved in FT data processing. Nevertheless, they strongly simplify the matter. Firstly, the interferogram actually is discrete, i.e. it is sampled only at discrete, equidistant points and not continuously as assumed in equations 3.3 and 3.4. Therefore, one has to use a discrete Fourier transformation, which will be described in one

of the following section. Secondly, not all monochromatic contributions integrated in equation 3.3 have the same phase. The phase is dependent on the wavenumber. This is due to dispersion of the beamsplitter, frequency-dependent electronic devices or the exact definition of the point of the mobile mirror's zero displacement (ZPD). Hence, equation 3.3 has to be completed by the wavenumber-dependent phase $\Phi(k)$:

$$I(x) = \int_{k=-\infty}^{\infty} S(k) \cos\left(2\pi k x + \Phi(k)\right)\mathrm{d}k \qquad (3.5)$$

or using the Euler relation and assuming a symmetric phase, i.e. $\Phi(k) = -\Phi(-k)$:

$$I(x) = \int_{k=-\infty}^{\infty} S(k)\, e^{i\,(2\pi k x + \Phi(k))}\mathrm{d}k \qquad (3.6)$$

Inverting the transformation then yields:

$$\int_{x=-\infty}^{\infty} I(x)\, e^{-i\,(2\pi k x)}\mathrm{d}x$$

$$= \int_{x=-\infty}^{\infty} \int_{\tilde{k}=-\infty}^{\infty} S(\tilde{k})\, e^{i\,(2\pi \tilde{k} x + \Phi(\tilde{k}))}\mathrm{d}\tilde{k}\, e^{-i\,(2\pi k x)}\mathrm{d}x$$

$$= \int_{x=-\infty}^{\infty} \int_{\tilde{k}=-\infty}^{\infty} S(\tilde{k})\, e^{i\,\Phi(\tilde{k})}\mathrm{d}\tilde{k}\,\mathrm{d}x \underbrace{\int_{x=-\infty}^{\infty} \int_{\tilde{k}=-\infty}^{\infty} e^{i\,2\pi\,(\tilde{k}-k)}\mathrm{d}\tilde{k}\,\mathrm{d}x}_{=0\ for\ \tilde{k}\neq k;\ =1\ for\ \tilde{k}=k}$$

$$= S(k)e^{i\,\Phi(k)}$$

$$= \mathbf{S}(k) \qquad (3.7)$$

Here, $\mathbf{S}(k)$ is the complex spectrum composed of a real $(S_{\mathrm{RE}}(k))$ and an imaginary part $(S_{\mathrm{IM}}(k))$:

$$\begin{aligned}
\mathbf{S}(k) &= S_{\mathrm{RE}}(k) + i\,S_{\mathrm{IM}}(k) \\
&= S(k)\,\cos\,\Phi(k) + i\,S(k)\,\sin\,\Phi(k) \\
&= S(k)e^{i\,\Phi(k)}
\end{aligned} \qquad (3.8)$$

Equations 3.6 and 3.7 show that $I(x)$ and $\mathbf{S}(k)$ are associated to each other by the general Fourier transformation.

3.2.2   Phase Correction

We have to keep in mind that not the result of the Fourier transformation, which is the complex spectrum $\mathbf{S}(k)$, is the actually interesting value, but $S(k)$ (see equation 3.2). Because of 3.8, $S(k)$ is also called amplitude spectrum. Due to equation 3.7, $S(k)$ is calculated by means of:

$$S(k) = e^{-i\,\Phi(k)} \int\limits_{x=-\infty}^{\infty} I(x)\, e^{-i\,2\,\pi\,k\,x} \mathrm{d}x \tag{3.9}$$

This step which extracts the amplitude spectrum $S(k)$ of the complex output $\mathbf{S}(k)$ of the Fourier transformation, is called the phase correction of the spectrum. The phase is calculated from equation 3.8:

$$\Phi(k) = \arctan\frac{S_{\mathrm{IM}}(k)}{S_{\mathrm{RE}}(k)} \tag{3.10}$$

3.2.3   Instrumental Line Shape

In equations 3.6 and 3.7 the integration was made from ∞ to $-\infty$, whereas a real interferometer consists of a spatially limited scanner. Consequently, the interferogram is truncated at finite optical path difference. To consider this, we multiply the infinite interferogram $I_{\mathrm{inf}}(x)$ used in equation 3.7 by a boxcar function $BX(x)$, which is zero for $|x| \geq L$ and unity for $|x| \leq L$. This yields a finite interferogram $I_{\mathrm{fin}}(x)$:

$$I_{\mathrm{fin}}(x) = BX(x)\, I_{\mathrm{inf}}(x) \tag{3.11}$$

This variation of the modulation efficiency with optical path difference is called apodization. The boxcar function $BX(x)$ is called apodization function. Hence, for calculating the spectrum $S_{\mathrm{fin}}(x)$ measured with a spatially limited scanner, we have to change equation 3.9 to:

$$\begin{aligned}
S_{\mathrm{fin}}(k) &= e^{-i\,\Phi(k)} \int\limits_{x=-\infty}^{\infty} I_{\mathrm{fin}}(x)\, e^{-i\,(2\,\pi\,k\,x)} \mathrm{d}x \\[2mm]
&= e^{-i\,\Phi(k)} \int\limits_{x=-\infty}^{\infty} I_{\mathrm{inf}}(x)\, e^{-i\,(2\,\pi\,k\,x)}\, BX(x)\, \mathrm{d}x
\end{aligned} \tag{3.12}$$

To determine S_{fin}, we make use of the convolution theorem of Fourier analysis. According to this theorem, the Fourier transform of a product of two functions is

given by the convolution (indicated by $\otimes$) of their individual Fourier transforms. Due to equation 3.12 in our case, we have to consider the Fourier transform $bx(k)$ of the boxcar function $BX(x)$, which is given by:

$$bx(k) = \int_{x=-\infty}^{\infty} BX(x)\, e^{-i\,(2\,\pi\,k\,x)}\mathrm{d}x \tag{3.13}$$

and the Fourier transform of $I_{\text{inf}}(x)$, which is known from equation 3.9:

$$S_{\text{inf}}(k) = e^{-i\,\Phi(k)} \int_{x=-\infty}^{\infty} I_{\text{inf}}(x)\, e^{-i\,(2\,\pi\,k\,x)}\mathrm{d}x \tag{3.14}$$

The convolution theorem then allows to reedit equation 3.12:

$$
\begin{aligned}
S_{\text{fin}}(k) &= e^{-i\,\Phi(k)} \int_{x=-\infty}^{\infty} I_{\text{inf}}(x)\, BX(x)\, e^{-i\,(2\,\pi\,k\,x)}\mathrm{d}x \\[2mm]
&= \int_{-\infty}^{\infty} S_{\text{inf}}(\tilde{k})\, bx(k - \tilde{k})\, \mathrm{d}\tilde{k} \\[2mm]
&= S_{\text{inf}}(k) \otimes bx(k)
\end{aligned}
\tag{3.15}
$$

Equation 3.15 states that every sharp, single spectral component that enters the interferogram is broadened by the FTIR spectrometer according to the function $bx(k)$, i.e. $bx(k)$ determines how the spectrometer distorts an incoming sharp spectral line. For this reason, $bx(k)$ is called instrumental line shape (ILS) function. Thus, the measured spectrum $S_{\text{fin}}(k)$ of a finite interferogram can be obtained by convolving the actual spectrum $S_{\text{inf}}(k)$ with the ILS. The analytical form of the ILS corresponding to boxcar truncation can be derived easily from the Fourier integral of a unity operand using a finite integration range. The result is the sinc function (see Figure 3.4):

$$bx(k) = \frac{L\,\sin(2\,\pi\,k\,L)}{2\,\pi\,k\,L} \tag{3.16}$$

According to the Rayleigh criterion, the spectral resolution is defined as the distance between the maximum of the sinc function and its first minimum. This yields:

$$\Delta k_{\text{Rayleigh}} = \frac{0.71}{L} \tag{3.17}$$
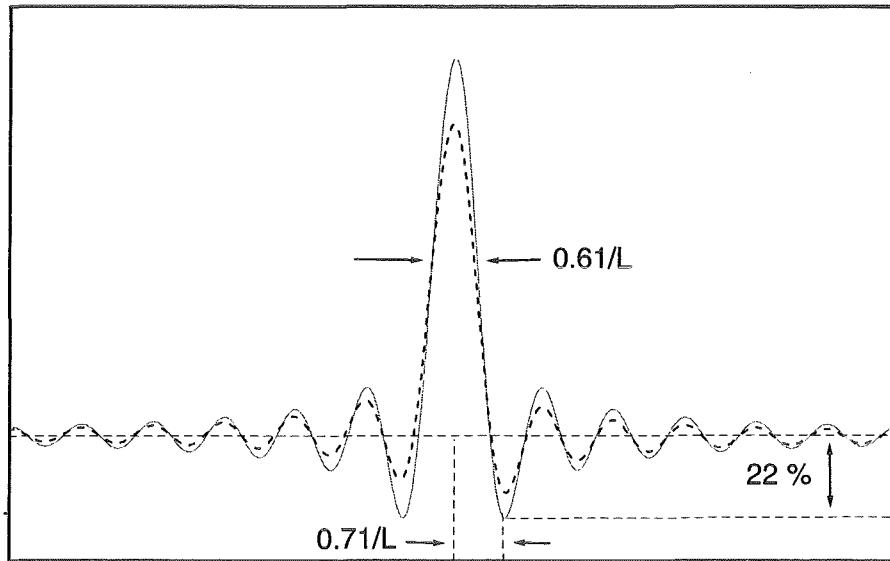
Fig. 3.4: Comparison of the ideal (solid line) and real (dotted line) ILS for
26/1/00.

The spectral resolution can also be characterized by the full width at half maximum:

$$\Delta k_{\text{FWHM}} = \frac{0.61}{L} \qquad (3.18)$$

Hence, the resolution of the FT spectrometer is proportional to the maximum optical path difference. In case of the IFS120M, the maximum optical path difference is 250 cm. Consequently, the achievable resolution is $0.0028\,\text{cm}^{-1}$ according to the Rayleigh criterion or $0.0024\,\text{cm}^{-1}$, if FWHM is applied. As the side lobes of the sinc function do not correspond to the actually measured information but rather represent an artifact due to the abrupt truncation at $x = L$, it is sometimes desirable to reduce their amplitude. Therefore, it is tried to find a cutoff function with a Fourier transform which showing fewer side lobes than the sinc function. An undesired side effect of these additional apodizations is a reduction of spectral resolution.

Additionally the so-called self-apodization influences the ILS. It is due to the finite field of view of the spectrometer, i.e. radiation enters from different angles. Self-apodization causes a infinite sharp line to be detected by the instrument as a spectral rectangle. Its width is approximately ([27]):

$$\Delta k_{\text{self}} = \frac{1}{2}\, k_0\, \alpha_{max}^2 \qquad (3.19)$$

Where k_0 is the wavenumber of the detected line and α_{max} is the maximum off-axis angle possible due to the finite field of view. Hence, finite aperture causes
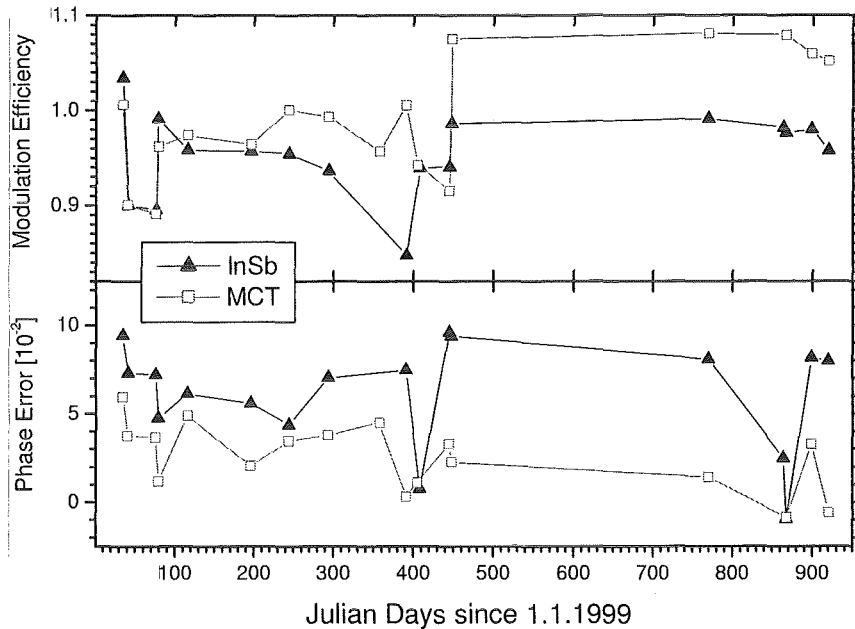
Fig. 3.5: Evolution of the ILS during the measurement period. The values are determined from gas cell measurements by means of LINEFIT ([26]).

an additional broadening of the ILS. Since the width of the spectral rectangle is proportional to k_0, the ILS becomes dependent on the wavenumber.

The profile of an atmospheric trace gas can be retrieved from the observed line shape because of the height-dependent pressure broadening. But the FWHM of absorption lines of stratospheric gases and of the ILS have similar magnitudes. Since the measured line shape is a convolution of the line shape of the trace gas and the ILS it is therefore crucial to know the ILS accurately. The real ILS differs from the ideal ILS (determined by the applied apodization function and the self-apodization) due to non-perfect alignment. We determined the real ILS of the IFS120M periodically by means of low-pressure gas cell measurements. The gas cell was filled with N_2O and placed in the parallel beam of a laboratory radiation source. The radiation source was a black body at 1000°C. The LINEFIT software was used to calculate the ILS by comparing the measured line shape with the theoretical one. A detailed description is given in [26]. The thus determined ILS was applied in the retrieval procedure. The evolution of the ILS during the measurement period of 1999-2001, as determined by LINEFIT, is shown in Figure 3.5, which demonstrates, that the instrumental alignment kept quite stable during the whole $2\frac{1}{2}$ years. Figure 3.5 illustrates the

modulation efficiency and the phase error, assuming a linear decline with the optical path difference, related to the respective values of an ideal instrument. Figure 3.4 shows the ideal ILS for the case of a boxcar apodization as well as a real ILS determined for 26/1/00. On 26/1/00 (day 391), Figure 3.5 indicates a relatively poor alignment of the instrument.

3.2.4   Discrete Fourier Transformation

Since the sampling of the interferogram is done at discrete points, the conversion performed actually is a discrete Fourier transformation. Thus, equation 3.7 changes to

$$S(m\,\Delta k) = \frac{1}{\sqrt{N}} \sum_{n=0}^{N-1} I(n\,\Delta x)\, e^{i\,2\,\pi\,\frac{n\,m}{N}} \tag{3.20}$$

The discrete analogue of equation 3.6 is

$$I(n\,\Delta x) = \frac{1}{\sqrt{N}} \sum_{m=0}^{N-1} S(m\,\Delta k)\, e^{-i\,2\,\pi\,\frac{n\,m}{N}} \tag{3.21}$$

where the continuous variables x and k have been replaced by $n\,\Delta x$ and $m\,\Delta k$, respectively. The spacing Δk of the spectrum is related to Δx by

$$\Delta k = \frac{1}{N\,\Delta x} \tag{3.22}$$

A derivation of the discrete Fourier transformation from the general Fourier transformation is made in [3].

For a limited number of functions, the corresponding Fourier transformation is known analytically and can be looked up in an integral table. However, in the general case of measured data, the discrete Fourier transformation and its inversion must be calculated numerically by computers. For this, equation 3.20 is not used directly, because it is highly redundant. Instead, the fast Fourier transformations method of Cooley-Tukey is in use. The Cooley-Tukey algorithm appreciably reduces the number of complex multiplications and sine and cosine calculations and therefore allows a faster transformation. However, this algorithm requires N, the number of sampling points, to be a power of two. As previously mentioned, the FT spectrometer uses the zero-crossing of the interference pattern of an He-Ne laser to control the displacement of the movable mirror. Therefore, the Cooley-Tukey algorithm, together with equations 3.1 and 3.22, only allows a sample spacing of $\Delta k = m\,k_{\text{laser}}/2^N$.

Chapter 4

The Measurement Site and Its Meteorological Situation

In this chapter, we present the measurement site, which is the Izaña Observatory (IZO). A short overview of its scientific activities shall be given. We briefly analyze the conditions of FTIR measurements and discuss the typical annual evolutions of the meteorological situation above Tenerife of 1999, 2000, and 2001 (until August).

4.1   Location

IZO forms part of the Instituto Nacional de Meteorología (INM , the National Spanish Meteorological Organization). It is located at 28°18'N, 16°29'W on the Canary Island of Tenerife at 2367 m a.s.l., on the foot of the Pico del Teide (3778 m) (see Figure 4.1). It belongs to the network of Global Atmospheric Watch (GAW) stations. This network was established in 1989 by the World Meteorological Organization (WMO) with the objective to provide information on the chemical composition and physical characteristics of the atmosphere and their trends. This requires clean air conditions in the present and future. Its minimum measurement program consists of in situ O_3, CO, CH_4, and aerosol composition measurements, analysis of precipitation chemistry, determination of meteorological parameters, and O_3 column amount measurements. The FTIR measurements were conducted from a container, placed appr. 50 m south of the main building on a concrete platform. This allows direct sunlight observations from sunrise to sunset. Only during some weeks in fall and winter does the peak of the Teide mountain inhibit measurements with an inclination lower than 8° during sunset. Within 2 km distance from IZO the Astrophysical Institute of the Canary Islands (IAC) is located. Liquid N_2 which is necessary for the cooling of the detectors, is supplied by the IAC.

Due to the FTIR, DOAS (Differential Optical Absorption Spectroscopy), Brewer,
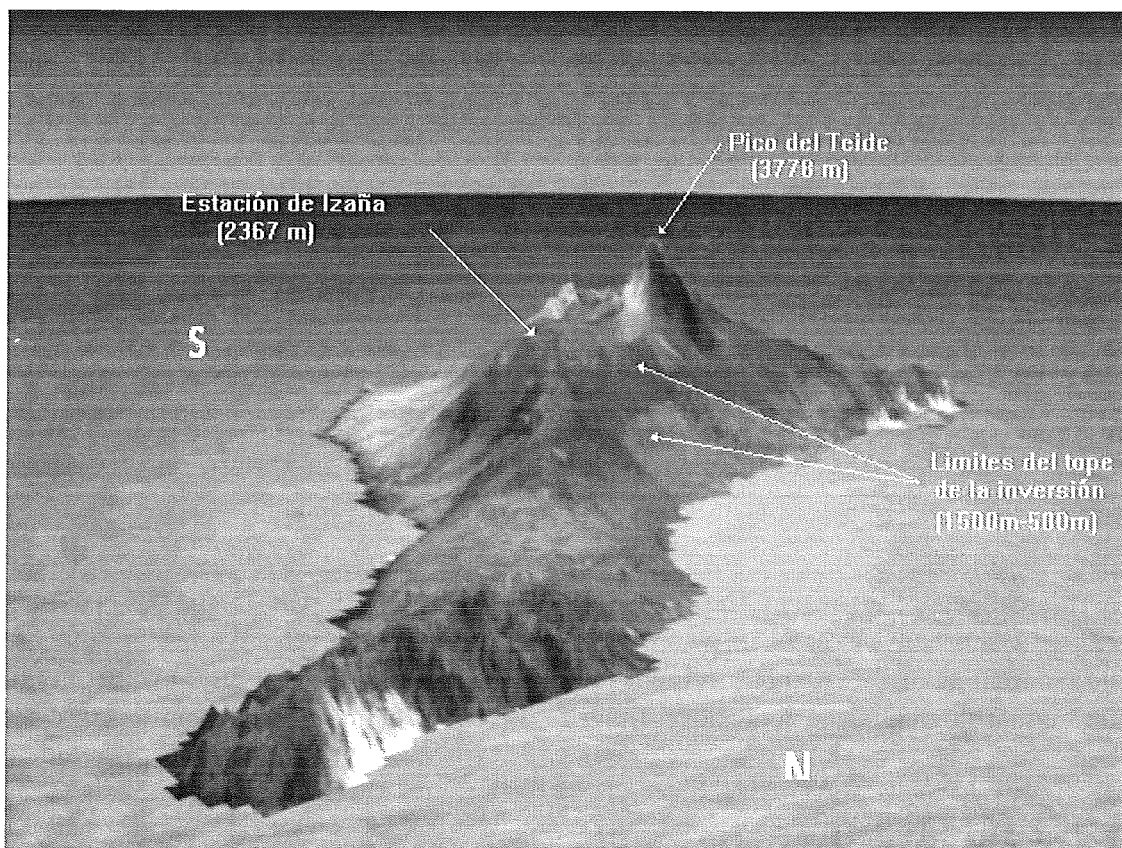
Fig. 4.1: Location of IZO on the island of Tenerife. Indicated are: Pico del Teide, Izaña Observatory, and the top of the inversion layer (which varies between 500 and 1500 m a.s.l.).

and O_3 sonde measurements, IZO was accepted as complementary site within the Network for Detection of Stratospheric Change (NDSC). This network consists of a set of high-quality remote-sounding stations for observing and understanding the physical and chemical state of the stratosphere. Ozone and ozone-related chemical compounds and parameters and their trends are the main targets of the measurement. It is also endorsed by international scientific organizations like the International Ozone Commission, the United Nations Environment Programme, and the WMO.

Instrument and Responsible Institution	Type of Observations	Record Start in	Relevant Publication
radio-soundings (INM)	meteorologic parameters	1958	[66]
surface O_3 analyzer TECO-49 C, TECO-49 C PS, Dasibi-100 8RS (INM)	surface O_3	1987	[38]
NDIR Siemens,Dani+Varia GCs, flask samples (INM, NOAA, U. Heidelberg)	surface CO, CO_2, and CH_4	1984	[67], [46], [59]
Brewer MARK II#33 and MARK III#157 (INM)	O_3 column, O_3 Umkehr profiles	May 1991	[1]
ECC-A5 and ECC-A6 (INM)	O_3 profiles	Nov. 1992	[48], [40]
Scanning UV/VIS spectrometer and UV/VIS photodiode array spectrograph (INTA)	O_3 and NO_2 column	Jan. 1993 and Dec. 1998 respectively	[77], [19]
PMOD/WRC sunphotometer (INM)	optical depth at 368, 500, and 778 nm	1994	[14]
Kipp&Zonen pyranometer (INM)	global and diffuse radiation	1992	
nuclei counter (TSI 3025) and particle size distribution detector (3071-A) (INM)	aerosol counting and size distribution (0.003 μm - 1μm	1997	[53], [7]
FTIR-spectrometer (IMK)	columns of H_2O, N_2O, CH_4, O_3, NO, NO_2, HNO_3, $ClONO_2$, HCl, and HF, and profiles of H_2O, N_2O, CH_4, O_3, NO, HCl, and HF	Feb. 1999	[this work]

Table 4.1: Experimental activities at IZO

4.2   Experimental Activities

The IZO's measurement program includes continuous CO_2, CH_4, CO, O_3, aerosol optical depth, and UV and VIS spectral radiation measurements. IZO also is a first-order synoptical station with both automated meteorological monitoring and visual observations. Meteorological sondes (PTU) are launched twice per day (at 00 UT and 12 UT) and ozone soundings (ECC electrochemical sonde) are generally conducted weekly. During intensive campaigns, more than twenty ozone sondes are launched per week. Both soundings were performed from the meteorological center in Santa Cruz de Tenerife (36 m a.s.l., 36 km northeast of Izaña). The O_3 column amount is monitored continuously with a Brewer spectrophotometer. It also provides two Umkehr-profiles per day (sunrise and sunset). Two UV/VIS DOAS spectrometers detecting zenith sky-scattered sunlight are used for the determination of the column amounts of O_3 and NO_2. A Bentham radiometer (DM-150) measures UV radiation (290-400 nm; 0.5 nm step). Finally, the FTIR spectrometer provides column amounts of H_2O, N_2O, CH_4, O_3, NO, NO_2, HNO_3, $ClONO_2$, HCl, and HF and profiles of H_2O, N_2O, CH_4, O_3, NO, HCl, and HF. For a summary of the experimental activities see also Table 4.1. In the near future, a Lidar will be installed additionally in the backfitted observatory, and the spectra evaluation of one of the UV/VIS absorption spectrometers will be improved for an additional measurement of BrO.

4.3   Meteorology

4.3.1   Measurement Conditions

While at sea level the temperatures show small seasonal variations only, IZO's mean temperatures range from 4.3°C (January) to 18.0°C (July). The distribution of precipitation is very irregular during the year, and strong interannual variability exists. Generally, the summer is very dry and the most rainy months are November and February. The Observatory with a mean pressure value of 770 hPa normally lies above a temperature inversion layer, which is generally well established between 500 and 1500 m a.s.l.. Consequently, it is free of local anthropogenic source influences. The sky is usually free of clouds and extremely clean, thus very suitable for radiation measurements (for statistics see 4.2). This is mainly a consequence of subsidence inversion which is typical for subtropical regions. The inversion is especially strong and regular in summertime, when the temperature and the relative humidity differences between the base and the top of the inversion reach their maximum values. Then, a dense persistent sea cloud is observed in the north part of the island. This layer clearly separates a marine mixed layer (high relative humidity (>60%) and an
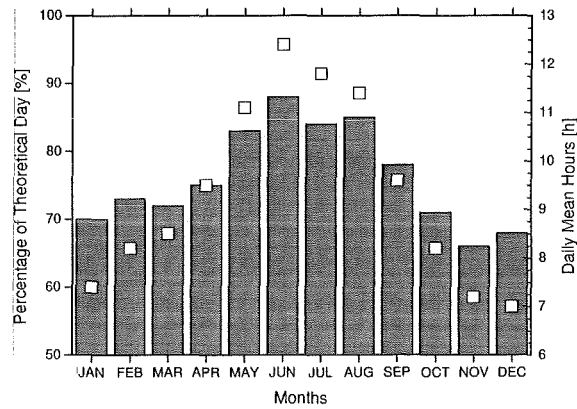
Fig. 4.2: Daily mean insolation at IZO. Bars represent the percentage of the theoretical day (left scale), hollow rectangles show the mean hours (right scale). The statistics results from observations made between 1961 and 1989.

aerosol optical depth of 0.2) from the free troposphere (normally, relative humidity less than 30% and an aerosol optical depth of 0.05 or less).

The pure air and clear sky conditions at Izaña are interrupted under Sahara outbreak conditions, when sand particles in the Sahara are lifted up to 6 km and are transported to the Canary Islands. These events occur occasionally in summer and early fall. The high content of suspended crustal dust particles results in an aerosol optical depth at Izaña of more than 0.2. In winter, when the inversion layer is weaker and less regular, it occasionally breaks and IZO is covered by fog or high clouds. Another restriction of the pure air condition at Izaña should also be mentioned: The strong diurnal insolation produces a slight upward flow of air originating from below the inversion layer. This results in a decrease of O_3 and CO_2 concentrations and an increase of NO, NO_2, NO_y, and PAN [67].

4.3.2 Atmospheric Parameters

In this section, some meteorological parameters which may be useful for an interpretation of the retrieved trace gases are presented. We show data of the tropopause height, potential vorticity, temperature, and backward trajectories for the years 1999, 2000, and 2001 (until August). The analysis of data spanning a long period also allows to describe the typical seasonal variations. As an example, we consider two isentropic levels in more detail. This is the 330 K level which is an upper tropospheric level and the stratospheric 550 K isentrope. For a typical altitude assignment
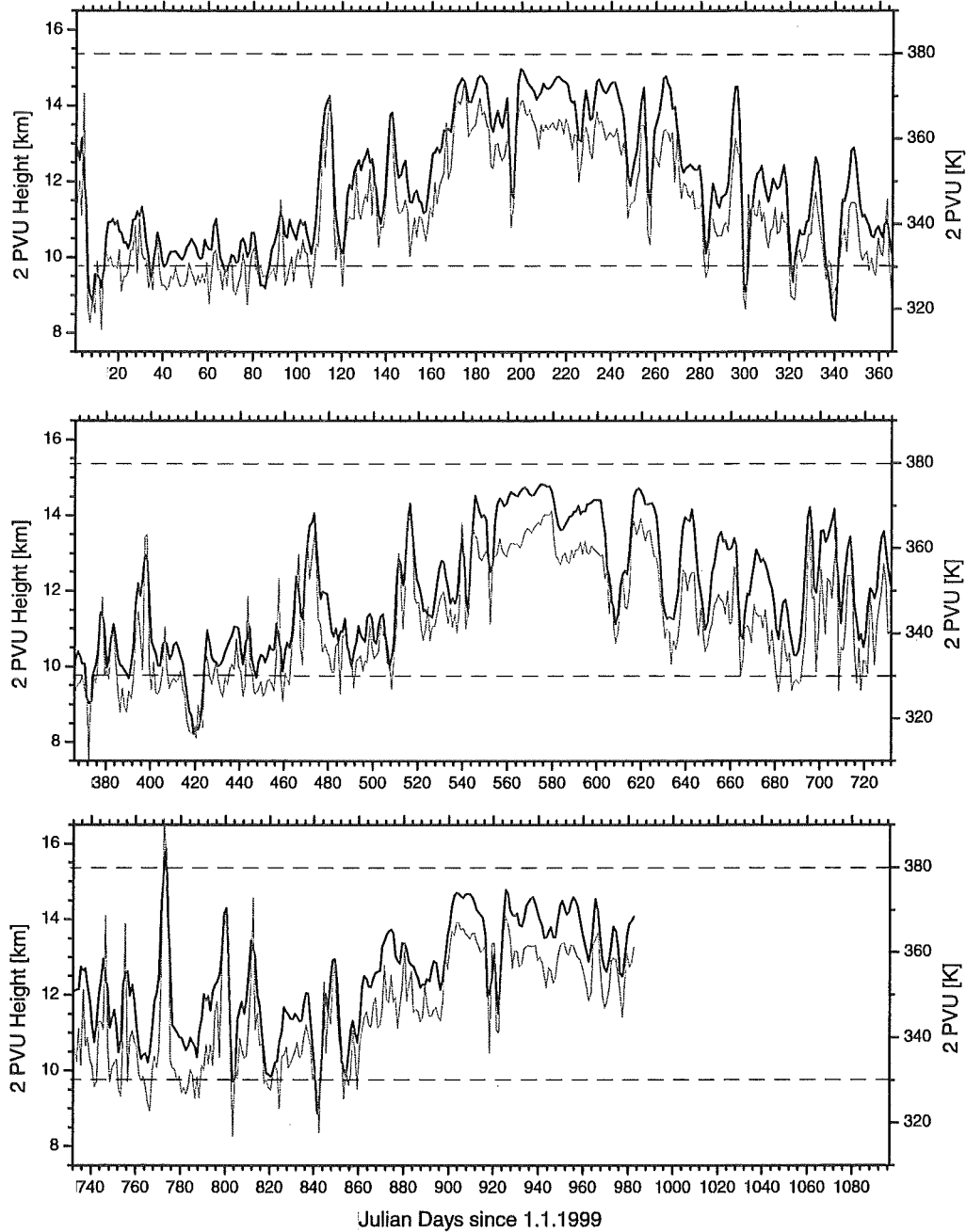
Fig. 4.3: Height of dynamical tropopause in 1999-2001. Thick line and left scale
show altitude of 2 PVU tropopause in km; thin line and right scale depict
2 PVU tropopause in potential temperature.
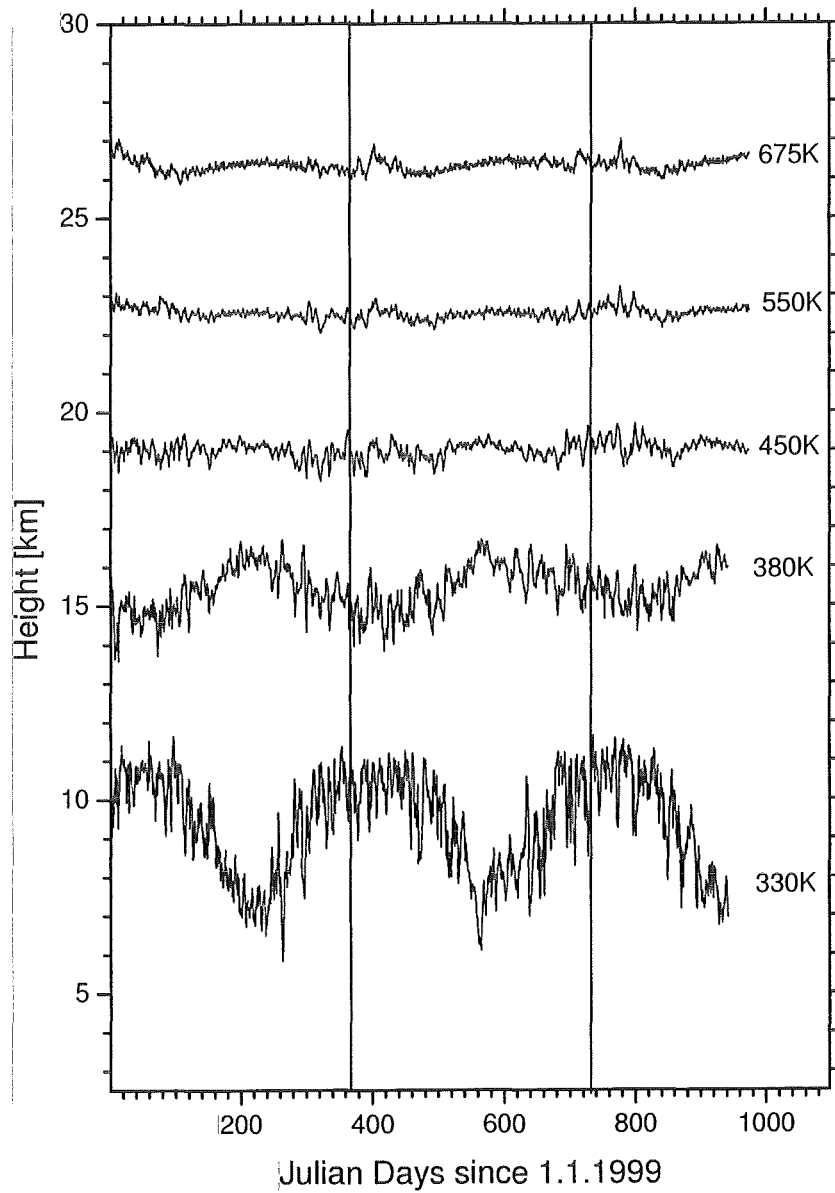
Fig. 4.4: Height of the 330 K, 380 K, 450 K, 550 K, and 675 K isentrope above IZO
in 1999-2001.

of the isentropes above IZO see Figure 4.4.

Tropopause Height

A dynamical tropopause height at 2 PVU is used. It is calculated from data obtained by an automailer system of the Atmospheric Chemistry and Dynamics Branch of NASA's Goddard Space Flight Center as described in [42]. Figure 4.3 depicts the corresponding data in km (left scale) and in potential temperature (right scale). A tropical tropopause is typically located around 380 K (appr. 16 km), while a mid-latitude tropopause is situated below 330 K (approximately 10 km). Above IZO, the tropopause varies strongly, in particular in winter. Both characteristic mid-latitude and tropical tropopauses occur. Occasionally, these strong variations take place during a short time only (e.g. April 1999 or February 2001). This is typical for subtropical regions, and due to the location in the tropopause break (see Figure 2.3). During summer, tropical influences prevail with a corresponding high tropopause.

Potential Vorticity

The potential vorticity was calculated from the Goddard automailer data [42] as already mentioned above. In contrast to high latitudes, where stratospheric potential vorticity is best-suited for interpretation of trace gas measurements due to its strong gradient across the polar vortex, these values are relatively uniform in the subtropics (see Figure 4.6). However, they may confirm conclusions deduced from other atmospheric parameters like backward trajectories. On 9/2/00, for example, the backward trajectories indicate polar airmasses. This is supported by the relatively high values of EPV occurring on the same days (see Figure 4.6). For a lower level like 330 K the EPV is very low, which is typical for the troposphere (see Figure 4.5).

Temperature

Temperatures are also taken from the Goddard automailer data. Although they are not suited for interpretation, they may, like the EPV values, support conclusions drawn from other parameters. E.g., on 9/2/00, the sharply decreasing temperature (Figure 4.6) supports the conclusion based on backward trajectories of polar airmasses being present.

Backward trajectories

The recorded time series of backward trajectories possibly represent the most powerful meteorological data set for the interpretation of the detected trace gases. These data are provided by the Climate Monitoring and Diagnostics Laboratory of NOAA.

Inputs of the trajectory model are 2.5-degree latitude-longitude gridded meteorological parameters furnished by the European Center for Medium Range Weather Forecasts or the U.S. National Centers for Environmental Prediction. For more details see [25]. All trajectory models are subject to uncertainties arising from interpolation of sparse meteorological data, assumptions regarding vertical transport, observational errors, sub-grid-scale phenomena, turbulence, convection, evaporation, and condensation. The averaged horizontal trajectory errors are estimated to be 140-290 km in 24 hours ([24] and references therein). Here 10-day isentropic backward trajectories are applied, and it should be remarked that the air parcel's trajectory 10 days prior to its arrival at IZO is subject to large uncertainties. However the large scale circulation should be reasonably represented by the calculated trajectories and hence it should be possible to deduce the origin region of the considered air parcel ([25]). It is seen in Figure 4.6 that in the stratosphere eastward flow prevails from November to April (airmasses originate from negative longitude values in Figures 4.5 and 4.6 means longitudinal degrees west of IZO), whereas in the summer months easterlies are observed, which is in agreement with Figure 2.2. In latitudinal direction, airmass origins vary widely during the winter period (November to April), which is due to the enhanced wave activity during that time, as described in chapter 2. In the summer, airmasses typically originate slightly south of IZO (negative latitude values in Figures 4.5 and 4.6 indicate latitudinal degrees south of IZO, positive values north of IZO). The small latitude area covered in this period during the 10 days prior to its arrival at IZO possibly indicates the vicinity of the subtropical transport barrier and, hence, the edge of the tropical reservoir. Both southernmost and northernmost airmasses are present above IZO during the winter, which makes this period especially interesting for studying transport processes. Another suitable parameter derived from the trajectories is the total distance travelled by the airmasses during the last 10 days. This value is especially high, if polar airmasses are present, which results from forcing of the polar vortex onto these airmasses and their consequent orbiting around the polar region. At lower altitudes (Figure 4.5) almost merely westerlies are observed. Only in some rare occasions are easterlies present during summer. This difference to higher altitudes is also indicated in Figure 2.2. The latitudinal flow pattern also is more uniform than in the case of the 550 K level. It indicates that meridional transport is stronger at this altitude and that there is no transport barrier similar to that observed for the summertime stratosphere. This is also consistent with the scheme shown in Figure 2.3.
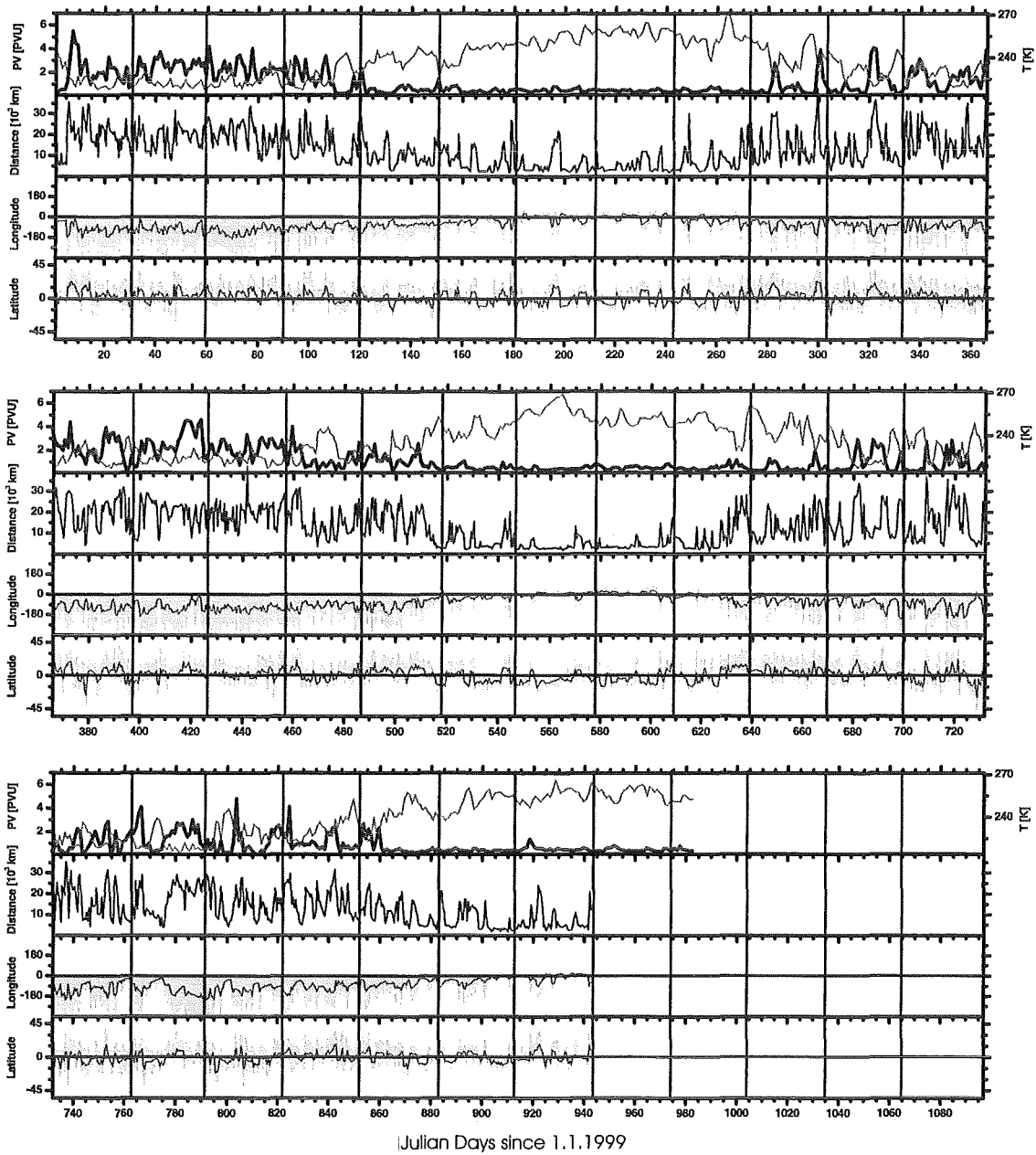
Fig. 4.5: Meteorological parameters for the 330 K isentrope from January 1999 until August 2001. Each panel shows from top to bottom: Potential vorticity (thick line and left scale) and temperature (thin line and right scale); total distance travelled by the airmass during the last 10 days before arriving at IZO; longitude region spanned by airmass during the last 10 days before arriving at IZO (shaded area), and the mean value (thin line) relative to IZO; same as above, but for latitude.

Julian Days since 1.1.1999
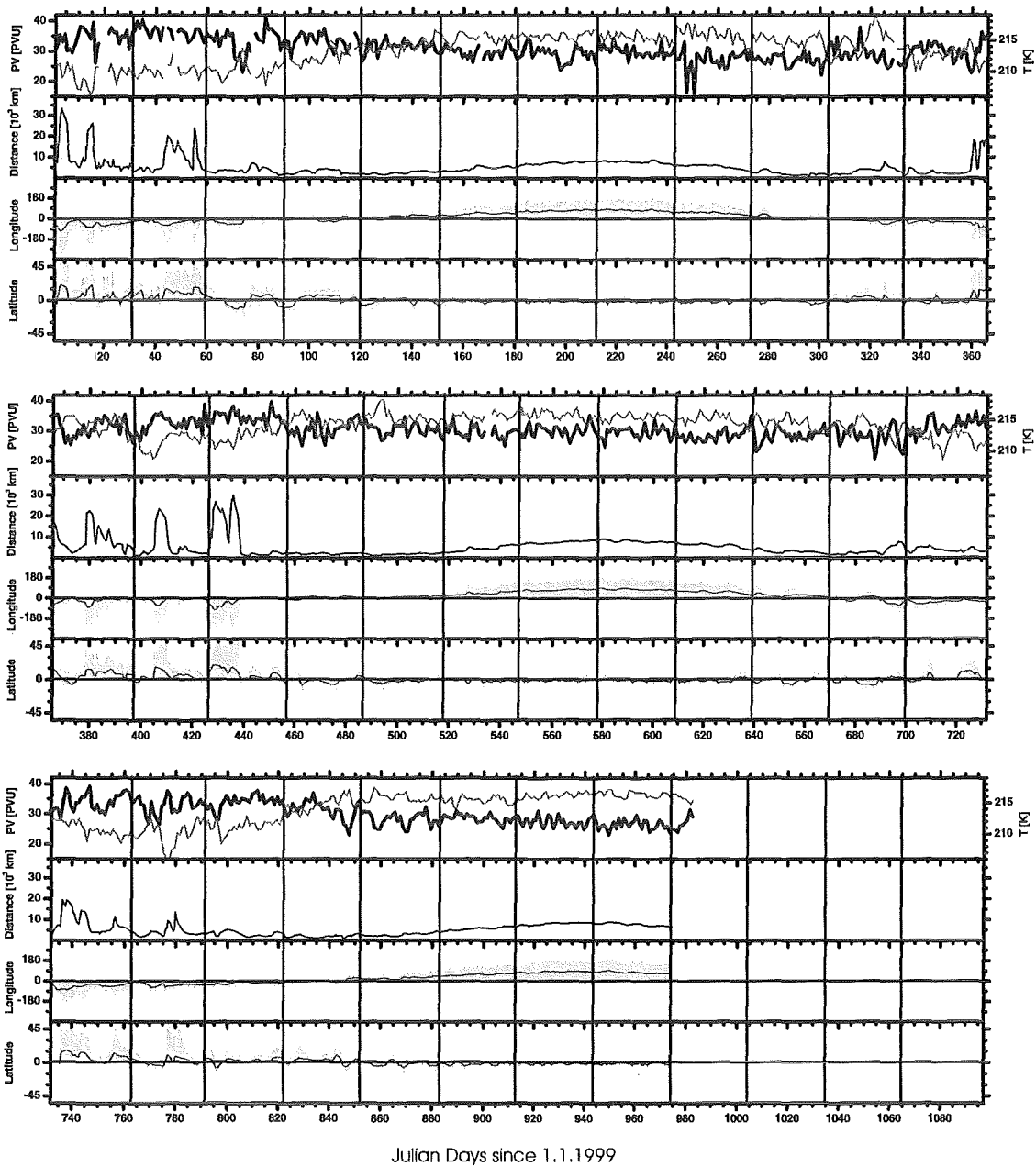
Fig. 4.6: Meteorological parameters for the 550 K isentrope from January 1999 until August 2001. Each panel shows from top to bottom: Potential vorticity (thick line and left scale) and temperature (thin line and right scale); total distance travelled by the airmass during the last 10 days before arriving at IZO; longitude region spanned by airmass during the last 10 days before arriving at IZO (shaded area), and the mean value (thin line) relative to IZO; same as above, but for latitude.

Chapter 5

Evaluation of the Spectra

This chapter describes how the trace gas profiles are derived from the measured spectra. In principle, a synthetic spectrum is iteratively improved by changing input parameters, like the trace gas profiles, in order to best fit the measured spectra. The mathematical procedure involved in this inversion process is presented briefly. Subsequently, the uncertainties of the derived profiles and column amounts shall be discussed. Finally, the evaluation process for each trace gas is considered in detail, i.e. typical residuals between the simulated and measured spectra, achievable height resolutions of the profiles, and error sources will be shown.

5.1 Remote Sensing of Atmospheric Trace Gases

5.1.1 Interaction between Matter and Radiation

The absorption spectrum of a gas consists of a complex array of lines that correspond to transitions between the discrete electronic, vibrational, rotational energy levels of molecules. Vibrational and rot-vibrational transitions occur in the microwave and IR region, while electronic transitions are stimulated by shorter wavelengths. At even higher photon energies a continuum of absorption occurs producing photodissociation and photoionization of molecules. For a more detailed consideration see e.g. [45].

Strength of Spectral Lines

The absorption coefficient κ_{nm} of a molecule with energy levels E_n and E_m for radiation with a frequency ν_{nm} is given by (e.g. [68]):

$$\kappa_{nm} = \frac{8\pi^2 n g_n}{3hcQ} \nu_{nm} \left|\mu_{nm}\right|^2 \left(e^{-E_m/k_B T} - e^{-E_n/k_B T}\right) \tag{5.1}$$

where g_n is the total degeneracy of the state at energy level E_n, Q the total internal partition function, n the total number density of the molecule regardless of the state, and μ_{nm} the electrical dipol matrix element for the transition between E_n and E_m.

Shape and Width of Spectral Lines

Different velocity components and interaction with other molecules, leads to a broadening of the absorption line of the molecules. Additionally in the IR, the vibrational transitions have rotational-translational fine structures that give rise to the characteristic appearance of a vibration-rotation band. Hence, absorption lines are not truly discrete and the absorption coefficient from equation 5.1 has to be extended by a normalized shape factor $f(\nu, \nu_{nm})$, which accounts for the line broadening and the fine structure of the absorption bands:

$$\kappa_{nm}(\nu) = \kappa_{nm} f(\nu, \nu_{nm}) \tag{5.2}$$

A fundamental source of line broadening is the natural broadening, which results from the finite radiation lifetime of excited states. From the point of view of quantum mechanics, natural line width is a consequence of the uncertainty principle. The natural broadening leads to a Lorentz line shape. The half width $\Delta\nu_N$ is the difference in frequency between the line center frequency and half maximum. Typical values for the IR region yield $\Delta\nu_N \approx 10^{-8}\,\mathrm{cm}^{-1}$. Natural line broadening in the IR region is unimportant compared to the following broadening mechanisms.

The molecular velocity components along any direction of observation produce Doppler broadening of the spectral lines, which has the shape of a Gaussian distribution:

$$f_D(\nu) = \frac{1}{\sqrt{\pi}\,\sigma_D} e^{-((\nu-\nu_{nm})/\sigma_D)^2} \tag{5.3}$$

with σ_D given by:

$$\sigma_D = \sqrt{\frac{2\,k_B\,T}{m\,c^2}}\,\nu_{nm} \tag{5.4}$$

where m is the molecule's mass, T the temperature and k_B is used as Boltzmann's constant. The dependence of σ_D on the frequency ν_{nm} of the center of the line provides for a dependence of the half width of the Doppler broadening $\Delta\nu_D$ on frequency:

$$\Delta\nu_D = 2\,\sigma_D\sqrt{ln2} = 2\,\nu_{nm}\,\sqrt{\frac{2\,k_B\,T}{m\,c^2}\,ln2} \tag{5.5}$$

A typical value (CO band at $2100\,\mathrm{cm}^{-1}$; $270\,\mathrm{K}$) is $\Delta\nu_D \approx 3 \times 10^{-3}\,\mathrm{cm}^{-1}$.

Pressure or collision broadening is due to disturbances by molecular collisions. These collisions affect the radiation lifetime. After the collision, the transition proceeds to completion, but this latter portion only bears a random phase relation to the original portion. Thus, the coherent lifetime is shorter than if undisturbed, and the radiated energy has a greater bandwidth. The caused line shape is similar to the natural one (Lorentz shape, see e.g. [3]):

$$f_p(\nu) = \frac{1}{\sqrt{\pi}} \frac{\Delta\nu_p}{(\nu - \nu_{nm})^2 + \Delta\nu_p^2} \tag{5.6}$$

where the the half width due to pressure broadening $\Delta\nu_p$ is related to the mean time between two collisions τ_{coll} by:

$$\Delta\nu_p = \frac{1}{2\,\pi\,\tau_{coll}} \sim p \tag{5.7}$$

Since $\tau_{coll} = \sqrt{m\,k_B\,T}/(4\,\sqrt{\pi}\,d^2\,p)$, $\Delta\nu_p$ is proportional to the pressure p (d represents the molecular diameter), typical values result in $\Delta\nu_p \approx 2 \times 10^{-2}\,\mathrm{cm}^{-1}$.

According to its temperature dependence, $\Delta\nu_D$ decreases slowly from the surface to the tropopause, and then it increases slightly through the stratosphere. In contrast to that, $\Delta\nu_p$ varies directly with p and inversely with $\sqrt{T}$. Hence, it decreases more or less exponentially with altitude. Thus, pressure broadening is more important at lower altitudes, while Doppler broadening predominates in the infrared in the middle stratosphere and above. One function suitable to describe the combined processes is the Voigt function, which is a convolution of the Doppler and Lorentz functions 5.3 and 5.6.

5.1.2   Radiative Transfer in the Atmosphere and the Simulation of Spectra

In the following sections we will neglect scattering processes, since they are relatively unimportant in the IR region. We further assume the radiation to traverse an atmosphere at local thermodynamic equilibrium (LTE).

Under these assumptions, the integrated form of the radiation transfer equation results in (e.g. [9]):

$$S(\nu, x_o) = \underbrace{B(\nu, T_{sun})\, e^{-\tau(\nu, x_o, \infty)}}_{solar\ radiation} + \underbrace{\int_{x=x_o}^{\infty} \kappa(\nu, x)\, B(\nu, T(x))\, e^{-\tau(\nu, x_o, x)}\, \mathrm{d}x}_{atmospheric\ radiation} \tag{5.8}$$

where Planck's function $B(\nu, T)$ is the source function for a black body at temperature T:

$$B_\nu(T) = \frac{2\,h\,\nu^3}{c^2}\,\frac{1}{e^{\left[\frac{h\,\nu}{k_B\,T}\right]} - 1} \tag{5.9}$$

and $\tau(\nu, x_o, x)$ is the optical depth at frequency ν for radiation originating from x and observed at x_o:

$$\tau(\nu, x_o, x) = \int_{x'=x_o}^{x} \kappa(x')\,\mathrm{d}x' \tag{5.10}$$

If we now further neglect the terrestrial atmosphere as a radiation source, since its intensity in the middle IR range relative to the corresponding intensity of the sun is approximately 1%, we can write:

$$S(\nu, x_o) = B(\nu, T_{sun})\,e^{-\tau(\nu, x_o, \infty)} \tag{5.11}$$

This incoming spectrum S will be transformed to the spectrum $\tilde{S}$ provided by the instrument, due to its instrumental characteristics discussed in chapter 3:

$$\tilde{S}(\nu, x_o) = \int_{\nu_0-\Delta\nu}^{\nu_0+\Delta\nu} (\mathcal{C}(\nu_0) + \mathcal{T}(\nu)\,S(\nu, x_o))\,\mathrm{ILS}(\nu_0 - \nu, \nu)\,\mathrm{d}\nu \tag{5.12}$$

Here, $\mathrm{ILS}(\nu_0 - \nu, \nu)$ is the value of the ILS function at wavenumber ν being $\nu_0 - \nu$ from its center peak position ν_0. The function $\mathcal{T}(\nu)$ describes spectral sensitivity of the instrument and $\mathcal{C}(\nu)$ stands for radiation emitted from the instrument itself.

The Karlsruhe Optimized and Precise Radiative Transfer Code (KOPRA)([31], [41], [70]) is used as radiative transfer model. Input data necessary for the transfer code are the location of the observation site, direction of the sun beam (elevation angle of the sun), height profiles of temperature and pressure, profiles of mixing ratios of the relevant gases, and instrumental parameters cited above. For numerical calculations both the optical path of the incoming sun beam and the spectrum are considered at discrete values only. The discrete analogue of 5.11 is:

$$S_i(x_o) = B(\nu_i, T_{sun})\,e^{-\sum_{j,k} \kappa_{jk}\,c_{jk}\,n_j\,d_j} \tag{5.13}$$

Whereas the index i stands for the spectral grid, j for the optical path grid (determined by the atmospheric layers), and k for the different relevant gases, d_j and n_j are the optical path length and the number density of the air molecules in the layer j, and κ_{jk} and c_{jk} are the specific absorption coefficient (absorption coefficient per number density) and the mixing ratio of gas k in layer j.

5.1.3   Inversion of Spectra

$S_i(x_o)$ from 5.13 can be separated into its contributions from the different layers j, i.e. $S_{ij}(x_o)$ is the contribution to $S_i(x_o)$ from layer j. Through κ, $S_{ij}(x_o)$ is

implicitly dependent on the temperature T_j, pressure p_j, and the number density c_{jk} of absorbing molecules in layer j. If we only consider terms of the order of one, we obtain a linear formulation of the radiative transfer equation:

$$
\begin{aligned}
S_{ij}(x_o, T_j, p_j, c_{jk}) \approx\ & S_{ij}(x_o, T_j^0, p_j^0, c_{jk}^0) \\
& + \frac{\partial S_{ij}(x_o, T_j, p_j^0, c_{jk}^0)}{\partial T_j}\,(T_j - T_j^0) \\
& + \frac{\partial S_{ij}(x_o, T_j^0, p_j, c_{jk}^0)}{\partial p_j}\,(p_j - p_j^0) \\
& + \sum_k \frac{\partial S_{ij}(x_o, T_j^0, p_j^0, c_{jk})}{\partial c_j k}\,(c_j k - c_j^0 k) \\
& + \cdots
\end{aligned}
\qquad (5.14)
$$

This equation can be written in the form of vectors and matrices:

$$
\mathbf{s} - \mathbf{s}^0 \approx \mathbf{A}^0 \cdot (\mathbf{f} - \mathbf{f}^0) \qquad (5.15)
$$

or,

$$
\begin{aligned}
\mathbf{A}^0 \mathbf{f} \approx\ & \mathbf{s} - \mathbf{s}^0 + \mathbf{A}^0 \mathbf{f}^0 \\
=\ & \Delta \mathbf{s}^0 + \mathbf{A}^0 \mathbf{f}^0
\end{aligned}
\qquad (5.16)
$$

Here $\mathbf{s}$ is a vector with i elements, i.e. its elements stand for the values at the respective spectral grid points, $\mathbf{f}$ contains the parameters that influence the spectra, e.g. T, p, and c for all layers. It consists of $N \times j + X$ elements, where N is the number of variables that influence the spectra and X stands for additional contributions to the spectra, like continuum absorption, indicated by the dots in equation 5.14. The elements of the Jakobi matrix $\mathbf{A}$ represent the partial derivatives of 5.14. These derivatives are also calculated by the radiative transfer code KOPRA. The indexes ^{0} stand for the start conditions and their respective simulated spectra and partial derivatives, i.e. $\mathbf{f}^0$ contains a priori T, p, and concentration profiles, $\mathbf{s}^0$ is the respective synthetic spectrum, and $\mathbf{A}^0$ describes the reaction of the synthetic spectrum $\mathbf{s}^0$ on variations of $\mathbf{f}^0$. Whereas $\mathbf{s}$ and $\mathbf{f}$ stand for the measured spectrum and the real parameters, $\Delta \mathbf{s}^0$ denotes the difference between measured and simulated spectra $\mathbf{s}^0$.

The system of linear equations 5.17 is overdetermined, if the number of spectral grid points exceeds the number of elements of vector $\mathbf{f}$. Therefore, it is looked for a solution that best fits to all linear equations in a least squares sense:

$$\left| \mathbf{A}^0\mathbf{f} - \Delta\mathbf{s}^0 - \mathbf{A}^0\mathbf{f}^0 \right|^2 = [\mathbf{A}^0\mathbf{f} - \Delta\mathbf{s}^0 - \mathbf{A}^0\mathbf{f}^0]^T[\mathbf{A}^0\mathbf{f} - \Delta\mathbf{s}^0 - \mathbf{A}^0\mathbf{f}^0] \qquad (5.17)$$

The solution of this problem is:

$$\mathbf{f} = [\mathbf{A}^{0T}\mathbf{A}^0]^{-1}\mathbf{A}^{0T}(\Delta\mathbf{s}^0 - \mathbf{A}^0\mathbf{f}^0) \qquad (5.18)$$

The linear approximation (5.14) is only valid for small variations of $\mathbf{f}$. Therefore, various iterations are necessary. The formulation of 5.18 for the ith iteration is:

$$\mathbf{f}^{i+1} = [\mathbf{A}^{iT}\mathbf{A}^i]^{-1}\mathbf{A}^{iT}(\Delta\mathbf{s}^i - \mathbf{A}^i\mathbf{f}^i) \qquad (5.19)$$

Additionally, a lot of equations of the system 5.15 show a linear dependence on each other, i.e. there is only little information in the spectrum, which allows to distinguish between the different layers. As a result, it is impossible to determine a non-ambiguous solution. In the case of ground based measurements the ambiguity can only be removed by imposing additional conditions (regularization). Measurements from satellites, airplanes or balloons additionally allow limb scanning of atmospheric layers which provides for a better information about the height distribution of the trace gases.

We used the inversion code PROFFIT [27] for the retrieval of the trace gas profiles. It allows to choose between two regularization methods: The Optimal Estimation Method ([60]) and the Tikhonov-Phillips Method ([49], [72]). We always applied the latter one, which additionally enables to impose two kinds of constraints of the form $\mathbf{B}\mathbf{s} = \mathbf{r}$. These constraints require a certain vicinity among the absolute values (subsequently referred to as absolute regularization) or between the slopes (subsequently determined as slope regularization) of a start profile and the retrieved profile. In analogy to 5.17 it is tried to minimize the Tikhonov-Phillips functional:

$$\left| \mathbf{A}^i\mathbf{f}^{i+1} - \Delta\mathbf{s}^i - \mathbf{A}^i\mathbf{f}^i \right|^2 + \gamma^2 \left| \mathbf{B}\mathbf{f}^{i+1} - \mathbf{r} \right|^2 \qquad (5.20)$$

The parameter γ is called regularization parameter. It can be varied from 0 to ∞, where $\gamma = 0$ would lead to the pure least squares minimization 5.19 and $\lim_{\gamma \to \infty}$ would try to best fit the additional conditions ($\mathbf{B}\mathbf{s} = \mathbf{r}$). The solution for 5.20 is:

$$\mathbf{f}^{i+1} = ([\mathbf{A}^{iT}\mathbf{A}^i] + \gamma^2[\mathbf{B}^T\mathbf{B}])^{-1}[\mathbf{A}^{iT}(\Delta\mathbf{s}^i - \mathbf{A}^i\mathbf{f}^i) + \gamma^2\mathbf{B}^T\mathbf{r}] \qquad (5.21)$$

Using the Tikhonov-Phillips approach, PROFFIT allows to perform the whole inversion procedure on a logarithmic scale. This avoids negative VMR values, and it was applied for all results presented here. It is possible to invert various profiles simultaneously by PROFFIT. Additionally, it allows a simple scaling of a given start profile (climatological profile), which is often done for interfering gases.

5.2 Error Analysis

In this section, we estimate the accuracy of our results by considering the uncertainties of the parameters used in the retrieval. We have to consider uncertainties in the temperature profile, the solar zenith angle (SZA), instrument parameters (ILS and the nonlinearity of the detectors), and in spectroscopic line data. Spectral noise and interfering species may also influence the results. Special attention is paid to the error caused by uncertainties in the SZA, which is more important at IZO than at high latitudes due to the higher velocity of the change of the SZA per time at low latitudes.

5.2.1 Spectral Noise

If the profiles to be retrieved were only scaled during the inversion, it is evident that the uncertainty of this scaling factor would be proportional to the uncertainty of the line strength. And if we further assume the uncertainty of the line strength to be proportional to the uncertainty of the depth of the absorption line with respect to its surrounding continuum, we can estimate the error due to spectral noise:

$$err_{\text{noise}} = \frac{\sigma}{S_0 \sqrt{N}} \tag{5.22}$$

where σ stands for the standard deviation of the spectrum from its mean (the noise on the spectrum) and N is the number of independent spectral grid points within the half width of the absorption line. Therefore, $\sigma/\sqrt{N}$ is the error of the spectral continuum value that surrounds the absorption line, which divided by the depth of the absorption line S_0, yields the error in the line strength and the error of the scaling factor and, hence, of the ZCA. Typical values for strong absorbers (O_3, HCl, HF, N_2O, CH_4) are less than 1.5%, whereas for weak absorbers this uncertainty can exceed 12% (NO_2, $ClONO_2$).

5.2.2 Offset in the Spectra

An offset signal in the spectrum may be mainly due to nonlinearity of the detector (shown in Figure 3.2). For a simple scaling retrieval and with $\Delta S/S$ being the offset relative to the continuum, the respective error can be estimated by:

$$err_{\text{offset}} = \frac{1}{1 - \Delta S/S} \tag{5.23}$$

While the photovoltaic InSb detector is assumed to work nearly linearly the photoconductive MCT detector shows nonlinearities. The offset typically is 1% of the continuum signal as seen in Figure 3.3, which results in an error of approximately 1%. Since these nonlinearities were measured regularly and consequently corrected, its error is far below 1% and, hence, it can be neglected.

5.2.3 Solar Zenith Angle
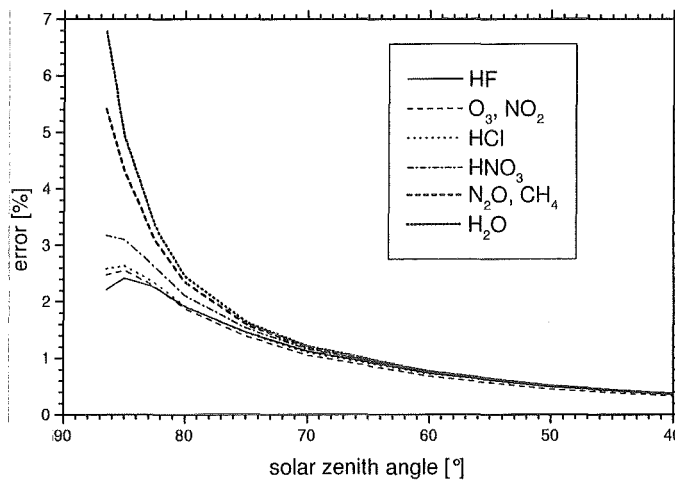
Fig. 5.1: Deviation from the real ZCA for a sun tracker mismatch of 0.25° versus the solar zenith angle. Curves represent the values calculated for typical profiles of the gases shown in the legend.

Since the solar zenith angle directly influences the spectrum simulated by the radiative transfer code, it should be determined with high accuracy. The solar zenith angle used for the simulation of the spectrum must correspond to the angle of the sun beam analyzed by the spectrometer. In principle, there are two reasons for disagreement between these angles. Firstly, the sun tracker may not track exactly the center of the sun and, secondly, the sun angle used in the radiative transfer code may be calculated erroneously due to incorrect input parameters, like geographical position or time. While an incorrect geographical position of the ground-based instrument can be excluded, it is sometimes difficult to determine the exact time of a measurement, since it can last up to 12 minutes (4 forward and 4 backward scans).

We now first examine the effect of a poorly pointing sun tracker. For a sun tracker pointing above the sun's center, the path of the sun beam through the Earth's atmosphere used in the radiation transfer code exceeds the path of the actually analyzed sun beam. This results in stronger absorptions in the simulated spectrum compared to the measured one and fitting the spectrum yields a smaller ZCA. A sun
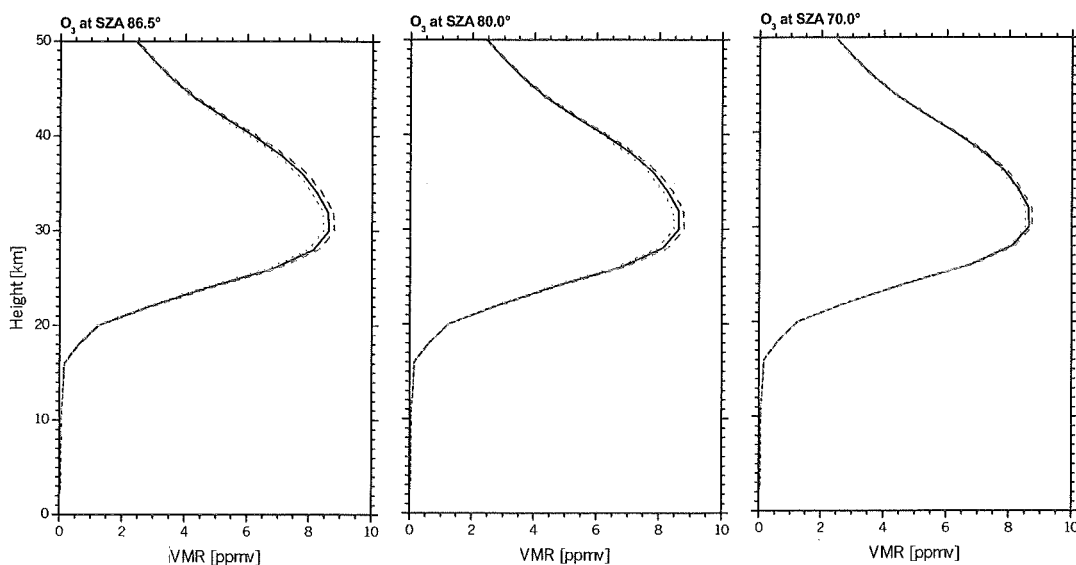
Fig. 5.2: Influence of sun tracker mismatch of 0.25° on O_3 profiles at different
solar zenith angles. Solid lines represent the real profile (no mismatch),
dashed lines show profile with sun tracker tracking 0.25° below center
of the sun, and dotted lines show profile with sun tracker tracking 0.25°
above center of the sun.

tracker pointing below the sun's center is expected to produce erroneously greater
ZCAs. The largest possible mismatch for the sun tracker still pointing any region of
the solar disc is 0.25°, since this is its radius. Hence, for the worst error estimation
we calculated three different spectra for several SZAs. One spectrum corresponds
to the nominal SZA, the second one to a 0.25° smaller SZA, and the third one
to a 0.25° greater SZA. Subsequently, these simulated spectra were all inverted
with the nominal SZA as input parameter. Figure 5.1 shows the deviations of the
ZCAs derived from the spectrum calculated with incorrect SZAs from the ZCA
derived from the correct spectrum. In particular, for SZA higher than 80° and for
tropospheric gases, this error becomes relevant and can reach 7% at a SZA of 86°.
Figures 5.2 and 5.3 show the influences on the profiles of a poorly pointing sun
tracker. We chose O_3 to show the typical influence on profiles of stratospheric gases
and N_2O for tropospheric gases, respectively. Whereas for stratospheric gases, the
resulting error in the mixing ratio is less than 2% at all altitude levels even for SZA
above 80°, it can exceed 8% for tropospheric gases at high SZA.

As mentioned above, a typical measurement with 4 forward and 4 backward scans
lasts approximately 12 minutes, i.e the measured spectrum contains information
spanning a rather long time and wide SZA interval. The radiative transfer code,
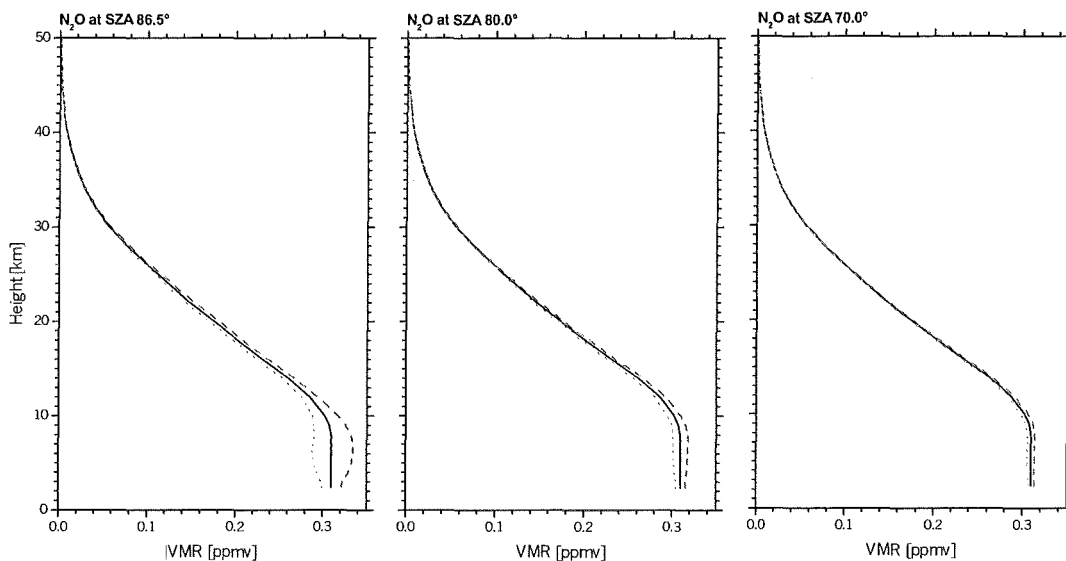
Fig. 5.3: Same as Figure 5.2, but for N_2O.

on the other hand, requires a single SZA for its calculations, for which the SZA corresponding to the mean time $((t_{start} + t_{end})/2)$ of the measurement is commonly used. At high latitudes, where the SZA changes rather slowly, this approximation is justified. At a low-latitude site like Izaña, however, the situation may be different. Figure 5.4 shows the change of SZA per minute versus SZA at Izaña. During morning and afternoon, the sun moves roughly $0.2°$ per minute. This is valid for all seasons. At noon, the change of ZCA reverses. In summer, this happens rather quickly, whereas in winter the sun decelerates and accelerates gradually from sunrise to noon and from noon to sunset, respectively. Hence, during a measurement of 12 minutes the SZA at Izaña changes by $2.5°$, and it should be analyzed whether the simple use of a mean SZA value corresponding to the mean time of the measurement influences the results. This may be especially important at low SZA and for tropospheric gases, since there is no linear relation between the detected slant column amount and time, i.e. the surplus of slant column amount detected during the scans performed before the mean time does not necessarily balance the lack of slant column amount detected during the scans after the mean time. For an error estimation, we calculated several spectra around the mean time of a thought measurement in steps of $100\,s$, which is a typical scan time. Since a measurement is given by the averages of the scans, averaging these spectra would better simulate the measured spectrum than a spectrum simply calculated for a single SZA corresponding to the mean time of the measurement. Subsequently, the spectrum built up by averaging and the spectrum calculated for the mean time SZA were inverted with the mean time
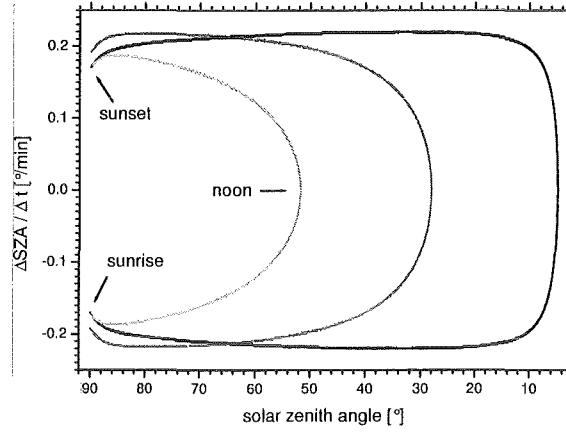
Fig. 5.4: Velocity of change of SZA versus SZA for 21/12, solstice, and 21/6.
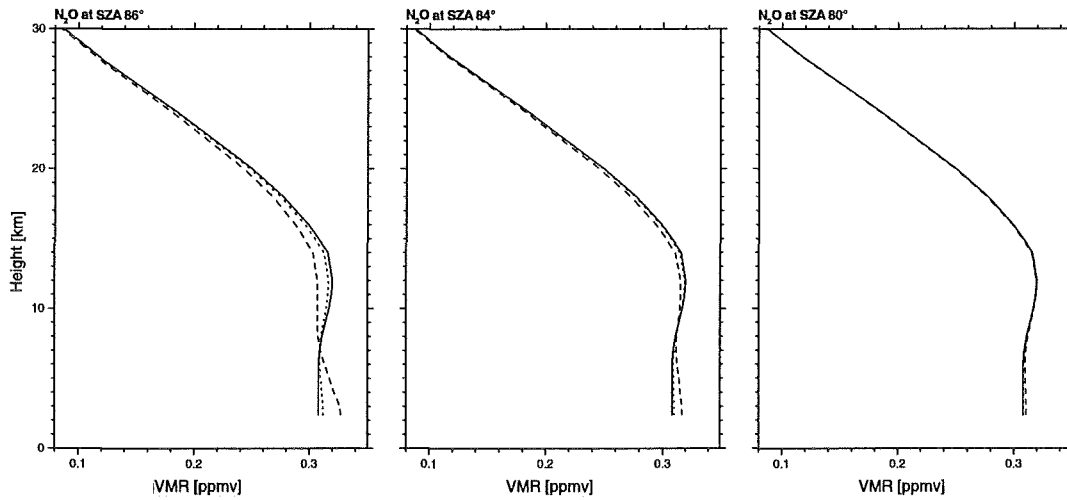
Fig. 5.5: Influence of applying a simple meantime of the measurement on the N_2O
profile. The solid line depicts the profile used for spectra simulation
(mean profile as derived from the FTIR measurements), the dotted line
shows profile retrieved from averaging single scan spectra, which together
span the time needed for 4 scans (400s), dashed line show the profile
retrieved by considering 8 scans (averaging 8 spectra).

SZA as input parameter. It is obvious that for the mean time SZA spectrum, the retrieval yields the nominal profile which was used for the spectrum simulation. But the profile retrieved with the average spectrum showed significant deviations from the nominal profile. However, Figure 5.5 demonstrates that the deviations are limited to high SZA and measurements spanning more than 5 minutes. For a measurement performed at an SZA of 86° and consisting of 8 scans, this effect can yield an error of 7% in the mixing ratio at certain altitudes, but already half the measurement time limits the error to 1%. For SZAs below 80°, the difference is very small even for long-lasting measurements. This effect has a negligible influence on the ZCAs, it only affects the shape of the profile. For stratospheric trace gases this effect could be neglected (less than 1%) at all SZAs. This error source was ruled out by only allowing measurements with a maximum of 4 scans for SZAs above 80° and with a maximum of 2 scans for SZAs above 85°.

Finally, it should be mentioned that the time elapsed during one scan (100 s) may also influence the results. In particular for high ZCA, when the detected air-masses change rapidly. At the beginning of a forward scan, the sampled information contributes mainly to the intensity of the spectra, whereas at the end of the scan highly resolved features of the spectrum are sampled.

5.2.4 Instrumental Line Shape

The ILS also influences the results, especially the shape of the VMR profiles. In [27] it was shown that its influences are greatest at altitudes, where the Doppler broadening becomes more important (above 20 km). A change of modulation efficiency during one scan of 5% with a maximum optical path difference of 250 cm would lead to a shift in the height profiles of approximately 1 km. The influences on the ZCAs can be neglected. As depicted in Figure 3.5, the regular determination of the ILS shows little variations, and since the measured ILS is applied in the retrieval, the assumption of the uncertainty in the modulation efficiency lying below 5% should be met ([27]).

5.2.5 Temperature Profiles

We use the temperature profile measured by the meteorological radiosondes launched twice a day (at 00 UT and 12 UT) from the meteorological center situated in the Island's capital Santa Cruz. These sondes generally ascend to approximately 34 km. Above this height, data taken from the Goddard automailer system are applied. They are based on the analysis of the National Centers for Environmental Prediction and available up to 45 km. From 45 km onward, we used the US standard atmosphere (US-76). The temperature sensors of the radiosonde have a precision of 0.2° and since they are calibrated before the launch, their accuracy should be at least within a
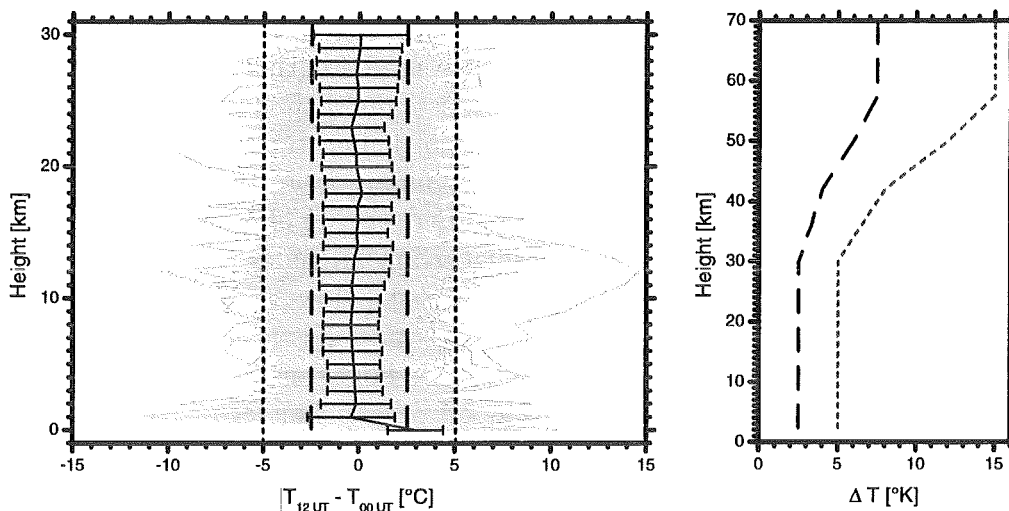
Fig. 5.6: Uncertainty in the temperature profile. Left part shows the temperature difference between profiles of 00 UT and 12 UT from the same day (grey lines) and a mean value with standard deviation (black line with error bars). Right part depicts two scenarios for temperature uncertainty. Scenario 1 (dashed line) describes the mean uncertainty of the temperature profile, whereas scenario 2 (dotted line) illustrates a worst case scenario.

$0.5°$ range. The Goddard and standard data applied above approximately 34 km are less accurate than the measured ones. We assume an typical error of 2% at 50 km and up to 6% at 70 km (see also [27]). Temperature analysis and measurements generally are performed for 12 UT, whereas the FTIR measurements are conducted at any time during daylight. This introduces another source of uncertainty. To estimate the typically short time variations of temperature, we compared the sonde data measured at 12 UT with those measured at 00 UT on the same day. Figure 5.6 shows these variations for all sondes from 1999-2001 (until August). In the average the temperature over one day varies by $\leq 2.5°C$ for all levels between 1 and 30 km without any preferred direction, i.e. both lower and higher temperatures at 00 UT compared to 12 UT have the same probability. Merely the level closest to the surface shows significantly higher temperatures at 12 UT compared to 00 UT. To rate the impact of incorrect temperatures, we first simulated a spectrum using a certain temperature profile and subsequently made a profile retrieval by applying a slightly changed temperature profile. The retrievals were made with two different temperature variations shown on the right of Figure 5.6. Scenario 1 (dashed line) describes the typical uncertainty of a temperature profile, whereas scenario 2 (dotted line) may be considered a worst case scenario. Figures 5.7 and 5.8 depict the influence of a temperature uncertainty according to scenario 1 on the trace gas
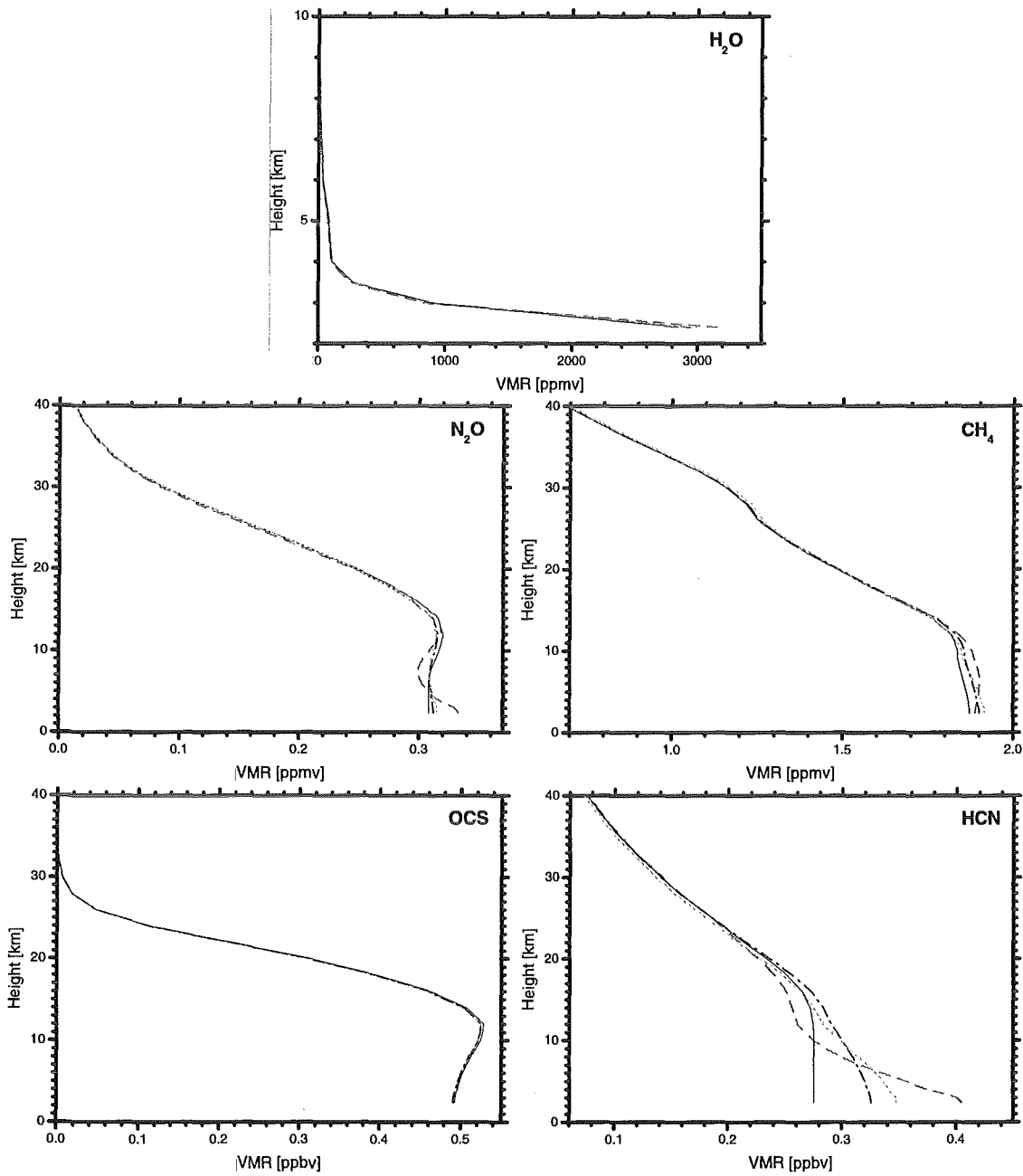
Fig. 5.7: Influence of temperature uncertainty on H_2O, N_2O, CH_4, OCS, and HCN profiles. In each panel, the original profile (solid line) and retrievals made for scenario 1 (mean temperature uncertainty, dashed line in Figure 5.6) at different SZA (dashed line: 86°; dotted line: 60°; dashed-dotted line: 6°) are shown.
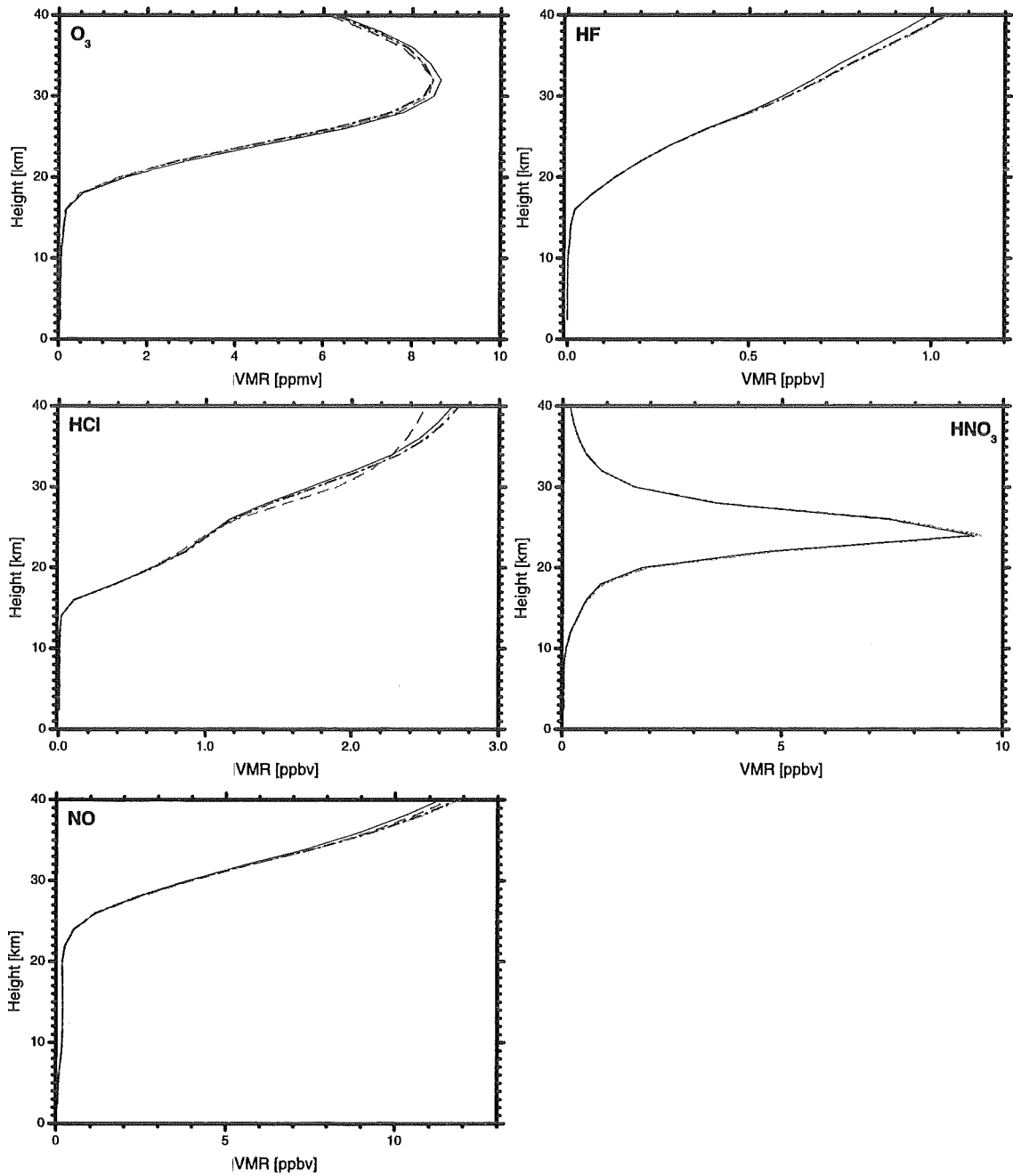
Fig. 5.8: Same as Figure 5.7, but for O_3, HF, HCl, HNO_3, and NO.

profiles.

The observed impacts on the profiles are caused by different effects. Firstly, a changed temperature profile will slightly change the temperature related to a certain pressure level, which, according to the ideal gas law, changes the number density of air molecules. In our scenarios, we increased the temperatures, which resulted in lower number densities. Since the absorption features in the spectrum are not changed by this effect, higher VMR are retrieved. This influences the retrieved VMR profile. The total column amount is affected slightly only due to changes in the shape of the profile. Secondly, the temperature dependence of the line strength yields uncertainties in the retrieved ZCA. These influences depend on each line and can weaken (N_2O, OCS, O_3, $ClONO_2$) or strengthen the absorption for rising temperatures (H_2O, CH_4, HCN, HNO_3, HF, HCl, NO_2, NO). Thirdly, interferences with other gases may influence the retrieved profile of the target gas, since the simulated signature of an interfering gas depends among other things on the applied temperature profile. This might be a reason for the strong impact of the applied temperature profile on the HCN profile as shown in Figure 5.7. Figure 5.13 indicates that a wrongly calculated CO_2 absorption at $3287.15\,cm^{-1}$ may influence in the wings of the HCN line and hence provide for an artefact in the VMR profile at lower altitudes.

For HCN and $ClONO_2$ a strong temperature dependence of the derived column amounts (14% and 18% for scenario 1) was observed. Like HCN, $ClONO_2$ may be influenced by a interfering CO_2 absorption line (see also Figure 5.17). For all other components analyzed these variations are less than 2% (scenario 1). In the next section, the uncertainties for both scenarios are listed for each trace gas in Tables 5.1 to 5.12.

Further temperature-based influences on the ZCA and profiles are due to the temperature dependence of the pressure and the Doppler broadening. However, both influences are negligible considering the rough height resolution of the profiles.

5.2.6 VMR Profile

The weak absorption features used for the determination of NO_2 and $ClONO_2$ contain too few information to derive profiles. For $ClONO_2$ the applied spectroscopic data do not include any pressure dependence. Hence, in these cases only scaling of an assumed profile is performed. The shape of the chosen profiles is somehow arbitrary, which introduces an additional error of approximately 5 % ([27]) and 8 % ([37]), respectively.

5.2.7   Interfering Species

The influences of interfering gases are difficult to evaluate. The problems are due to their unknown profiles and uncertainties in their spectroscopic data. For the assumed correct spectroscopic data, the impact is generally negligible ([37]). However, in combination with erroneous temperature profiles, interferences can be important. This is shown above for HCN and ClONO2, whose absorption features overlap with CO_2 lines (see Figures 5.13 and 5.17). The strong dependence of column amounts of both gases on the temperature profile as retrieved above, may be partly due to interference from CO_2.

5.2.8   Spectroscopic Data

The absorption coefficients and their temperature and pressure dependence were obtained from laboratory measurements, which are only possible up to a certain accuracy. Our evaluation was made with spectroscopic data of HITRAN 96 (High Resolution Transmission Molecular Absorption Database, [61]). The relative uncertainty of the line strength is directly transmitted to the relative error in the ZCA and the VMR (in the sensible height regions). It depends on the trace gas and the considered band and varies between 2% and 15%.

Spectroscopic errors lead to systematic deviations from a real profile or ZCA and should therefore be considered independently of the uncertainty associated with the trace gas retrieval.

5.3   Data Analysis for Each Trace Gas

In this section, the evaluation procedure of each trace gas is considered in detail. The parameters relevant in the retrieval procedures are specified. We present the chosen spectral interval and typical differences between measured and simulated spectra (residual spectra). Also shown are typical height resolutions for each trace gas, where profiling was applied. The error sources for the ZCAs are discussed and listed for each trace component (Table 5.1). The error due to uncertainties in the temperature profile is given for scenario 1 (typical) as well as for scenario 2 (worst case, in brackets).

Due to the large amount of measurement days (approximately 200 from February 1999 to July 2001) it was necessary to partly automatize the evaluation procedure. Therefore, within this work, same small programs were created. They reduced the work involved in the calibration of the spectra, in the implementation of the actual radiosonde data, and in the creation of input files. These input files include the SZA of the measurement, the wavenumber range where the target gas absorbs,

regularization parameters, climatological profiles, ILS, etc. and they have to be created individually for each single retrieval.

5.3.1 H_2O

H_2O is evaluated in the spectral region of 2662.39-2664.17 cm^{-1}. There are also absorption features of CO_2 and CH_4. In particular, the latter ones are relatively strong. Hence, the CH_4 absorption features are considered by scaling of a climatological CH_4 profile, whereas for CO_2 the corresponding climatological profile is kept unchanged during the fitting process. The H_2O profile is retrieved by absolute regularization (regularization against absolute values of a start profile). Comparison with sonde data (see next chapter) shows that this kind of regularization is better suited for the detection of extraordinary profile features, which mainly consists in a second maximum apart from the one present at the surface, than the slope regularization (regularization against the slope of a start profile). The information included in the spectrum typically allows to differentiate between two layers below 12 km (Figure 5.9). The uncertainty in the ZCA is dominated by uncertainties of the SZA, in particular at high SZA.

5.3.2 N_2O

The spectral interval used for the evaluation of N_2O (2481.28-2482.49 cm^{-1}) also shows major absorption lines of CO_2 and CH_4. The former is considered by slope regularization. The latter is simply fitted by applying a fixed climatological profile as well as the minor absorbers H_2O and O_3. As shown in Figure 5.10, three independent height levels typically are resolved. For the target gas N_2O slope regularization is used. Especially for high SZA, the total error in the ZCA is dominated by errors due to uncertainties in the SZA.

5.3.3 CH_4

For the retrieval of CH_4 two spectral intervals are used. The first ranging from 2835.53 cm^{-1} to 2835.80 cm^{-1} does not contain any major additional absorption features, while the second covering wavenumbers between 2903.60 cm^{-1} and 2904.25 cm^{-1} also includes a relatively strong absorption line of HCl at 2904.10 cm^{-1} and is influenced by the wing of an H_2O line. It also contains some minor O_3 absorption features. CH_4 is retrieved using slope regularization. The HCl absorptions are also considered by slope regularization, while the lines of H_2O and O_3 are only taken into account by scaling. Three independent layers can be distinguished (see Figure 5.11). As for the other tropospheric components, the total error in the ZCA is dominated by errors due to uncertainties in the SZA.
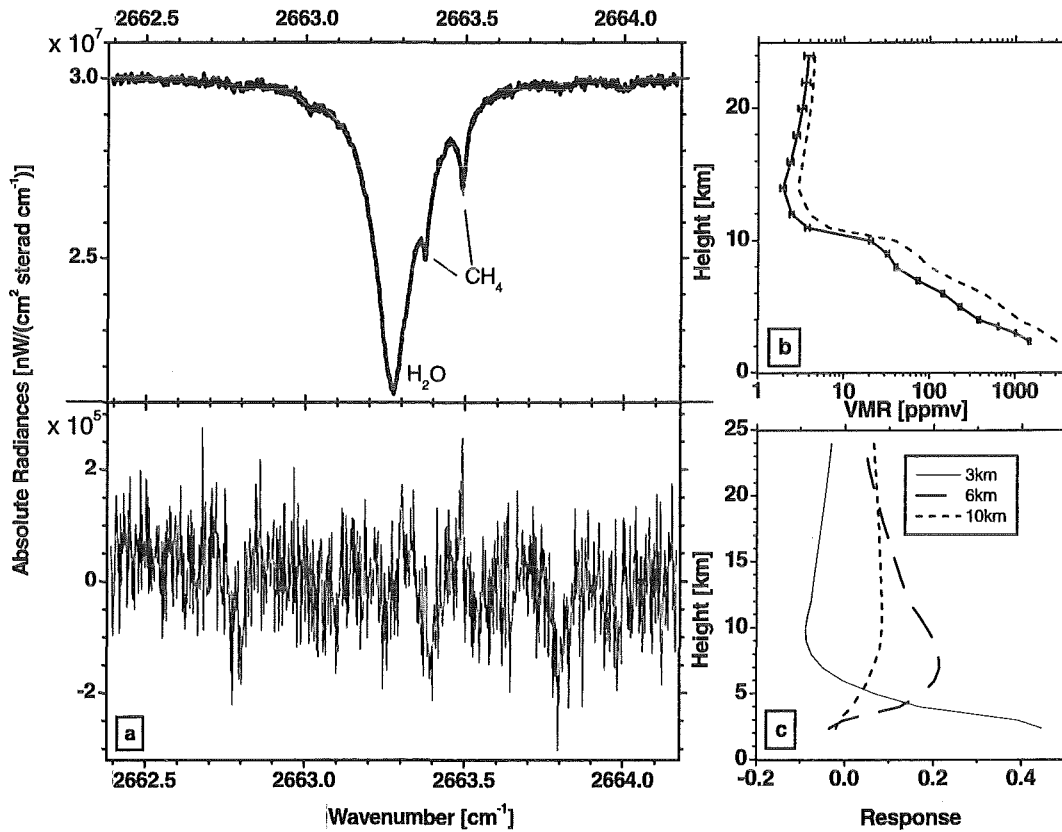
Fig. 5.9: Typical evaluation of H_2O. a: Upper part shows the measured spectrum (thick line) and simulated spectrum (thin line), lower part shows the difference between both spectra; b: Applied start profile (dotted line) and retrieved profile (solid line); c: Averaging kernels for some selected heights as described in the legend.

noise	0.3%
SZA	$\leq 6\%$
T profile	0.6% (1.3%)
total	**6%**
spectroscopic data	undefined

Table 5.1: Error budget for ZCAs of H_2O.
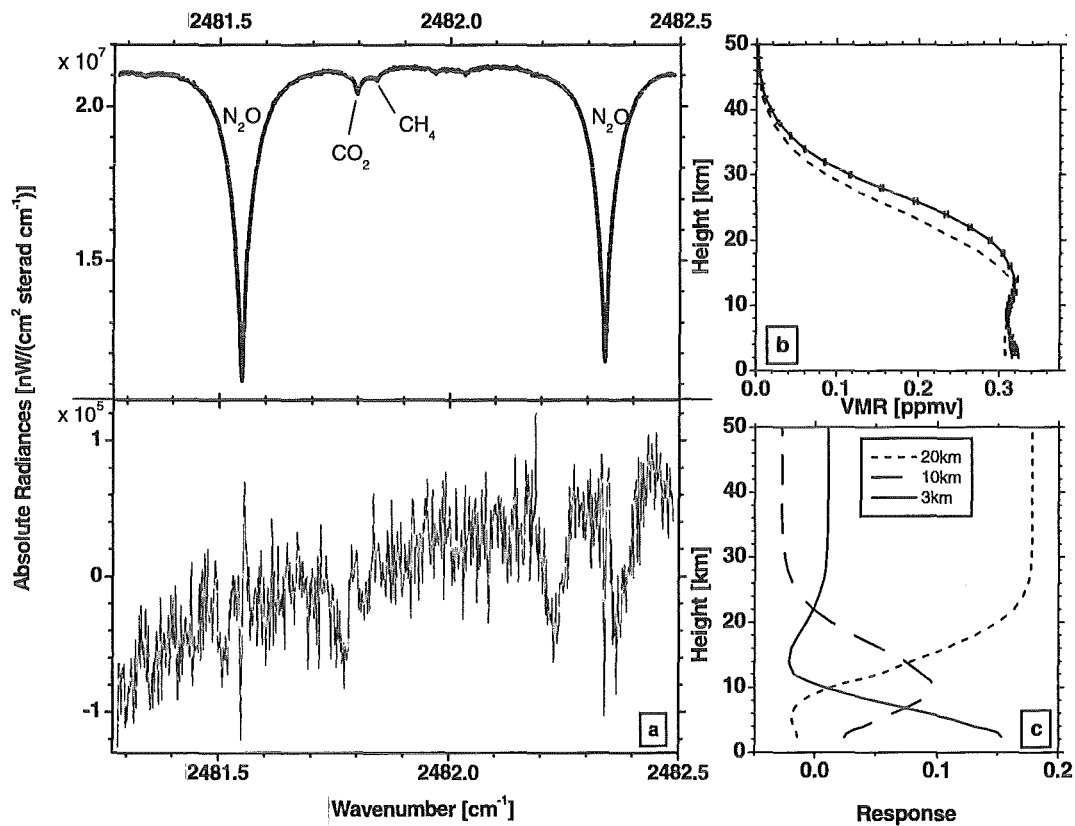
Fig. 5.10: Typical evaluation of N_2O. a: Upper part shows the measured spectrum (thick line) and simulated spectrum (thin line), lower part shows the difference between both spectra; b: Applied start profile (dotted line) and retrieved profile (solid line); c: Averaging kernels for some selected heights as described in the legend.

noise	$\leq 0.3\%$
SZA	$<5\%$
T profile	$<0.25\%$ ($<0.5\%$)
total	**5%**
spectroscopic data	undefined

Table 5.2: Error budget for ZCAs of N_2O.
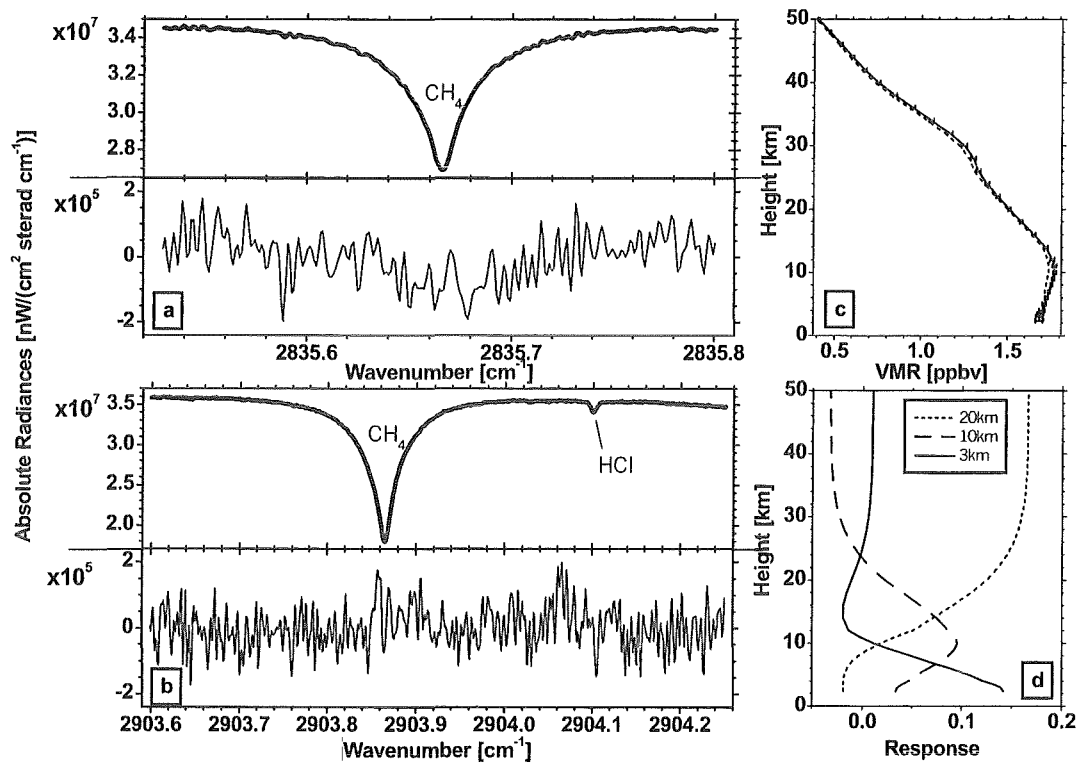
Fig. 5.11: Typical evaluation of CH_4. a+b: The two applied spectral intervals
are shown, whereby the upper parts show the measured spectrum (thick
line) and simulated spectrum (thin line), and the lower parts show the
difference between both spectra; c: Applied start profile (dotted line)
and retrieved profile (solid line); d: Averaging kernels for some selected
heights as described in the legend.

noise	$\leq 1\%$
SZA	$< 5\%$
T profile	0.5% (1%)
total	**5%**
spectroscopic data	5-10%

Table 5.3: Error budget for ZCAs of CH_4.
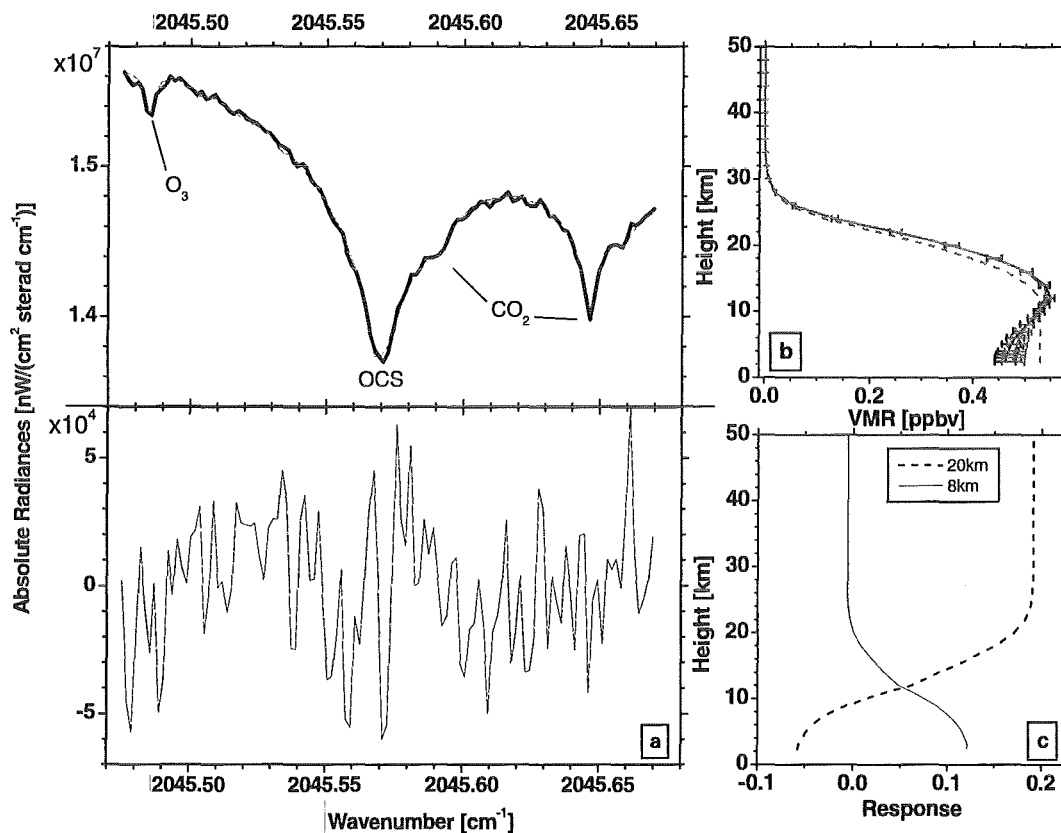
Fig. 5.12: Typical evaluation of OCS. a: Upper part shows the measured spectrum (thick line) and simulated spectrum (thin line), lower part shows the difference between both spectra; b: Applied start profiles (dotted lines) and retrieved profile (solid lines with error bars); c: Averaging kernels for some selected heights as described in the legend.

noise	$\leq 2\%$
SZA	$<5\%$
T profile	1.4% (2.8%)
VMR start profile	$<1\%$
total	**5.5%** (6%)
spectroscopic data	undefined

Table 5.4: Error budget for ZCAs of OCS.

5.3.4   OCS

OCS is retrieved in the region between $2045.48\,\mathrm{cm}^{-1}$ and $2045.67\,\mathrm{cm}^{-1}$, where additionally H_2O (wings), CO_2, O_3, and CO (wing) absorb. While the CO signature is calculated from a fixed profile, scaling is performed for H_2O and O_3, and for CO_2 slope regularization is applied. For the retrieval of the OCS profile also slope regularization is applied. In Figure 5.12b two nearly identical FTIR profiles (lines with error bars) are shown. They were retrieved with two start profiles (also depicted in figure 5.12b as dashed lines), which only differ below 10 km. The first start profile has a constant tropospheric VMR of 0.53 ppbv and is similar to that applied by [22]. The second one is a mean profile from all retrieved FTIR profiles and it decreases from 0.53 ppbv at 10 km to 0.49 ppbv at 2.5 km. The decrease from 10 km to 2.5 km as observed in the FTIR profiles may also be due to interferences with the CO_2 line at $2045.59\,\mathrm{cm}^{-1}$. However, similar tropospheric gradients were also reported by [34]. Since the retrieved profiles and column amounts depend only weakly on the applied start profile (less than 1 % difference in the corresponding column amounts), and since the height resolution for OCS is sparse (see Figure 5.12c) uncertainties in the applied start profiles represent only a secondary error source. For the OCS data presented here the mean of all retrieved FTIR profiles was applied as start profile. The total error is dominated by noise and uncertainties in the SZA.

5.3.5   HCN

The HCN spectral interval (3286.40-$3287.35\,\mathrm{cm}^{-1}$) also contains absorption features of H_2O, CO_2, and some minor absorptions of C_2H_2 and O_3. The signatures of O_3 and C_2H_2 are merely considered by a fixed profile. For H_2O, scaling is performed and for CO_2 and the target gas HCN slope regularization. The height resolution is limited to two layers (see Figure 5.13). The line strength of the HCN absorption feature shows a strong temperature dependence, which may be partly due to interferences from the CO_2 absorption line at $3287.15\,\mathrm{cm}^{-1}$.
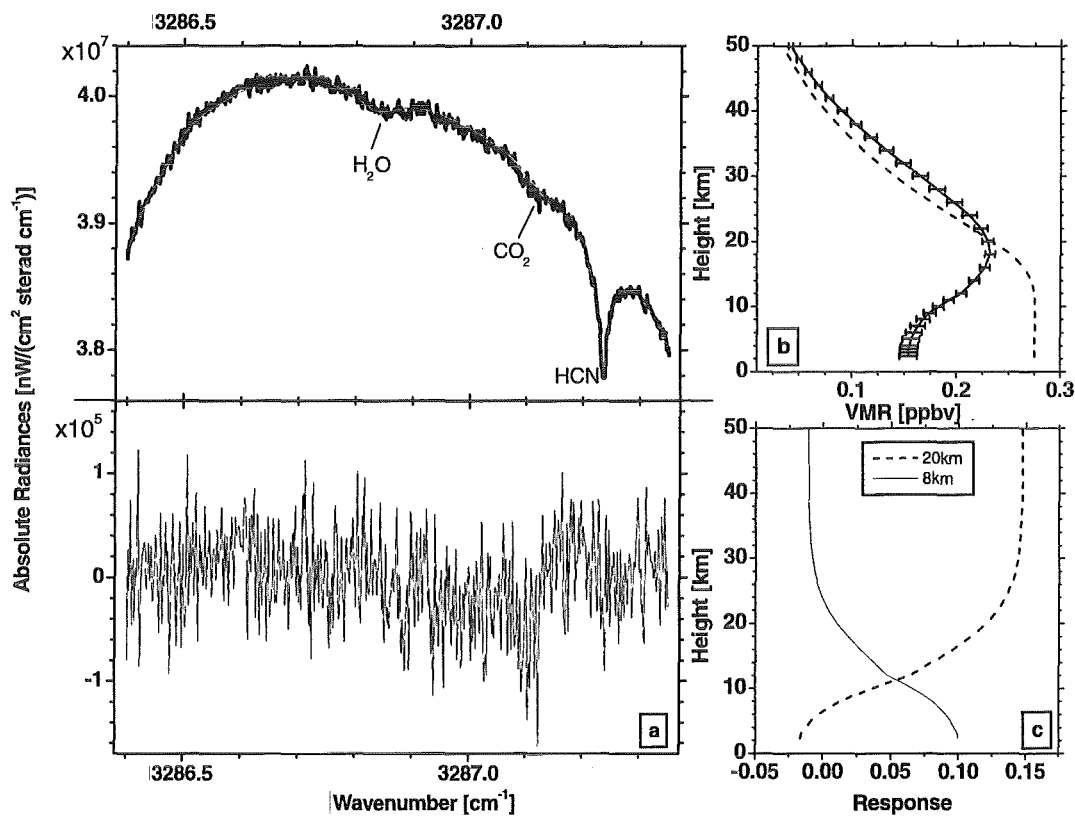
Fig. 5.13: Typical evaluation of HCN. a: Upper part shows the measured spectrum (thick line) and simulated spectrum (thin line), lower part shows the difference between both spectra; b: Applied start profile (dotted line) and retrieved profile (solid line); c: Averaging kernels for some selected heights as described in the legend.

noise	5%
SZA	<5%
T profile	10.3-14.2% (20.6-28.1%)
total	**12-16% (21-29%)**
spectroscopic data	undefined

Table 5.5: Error budget for ZCAs of HCN.
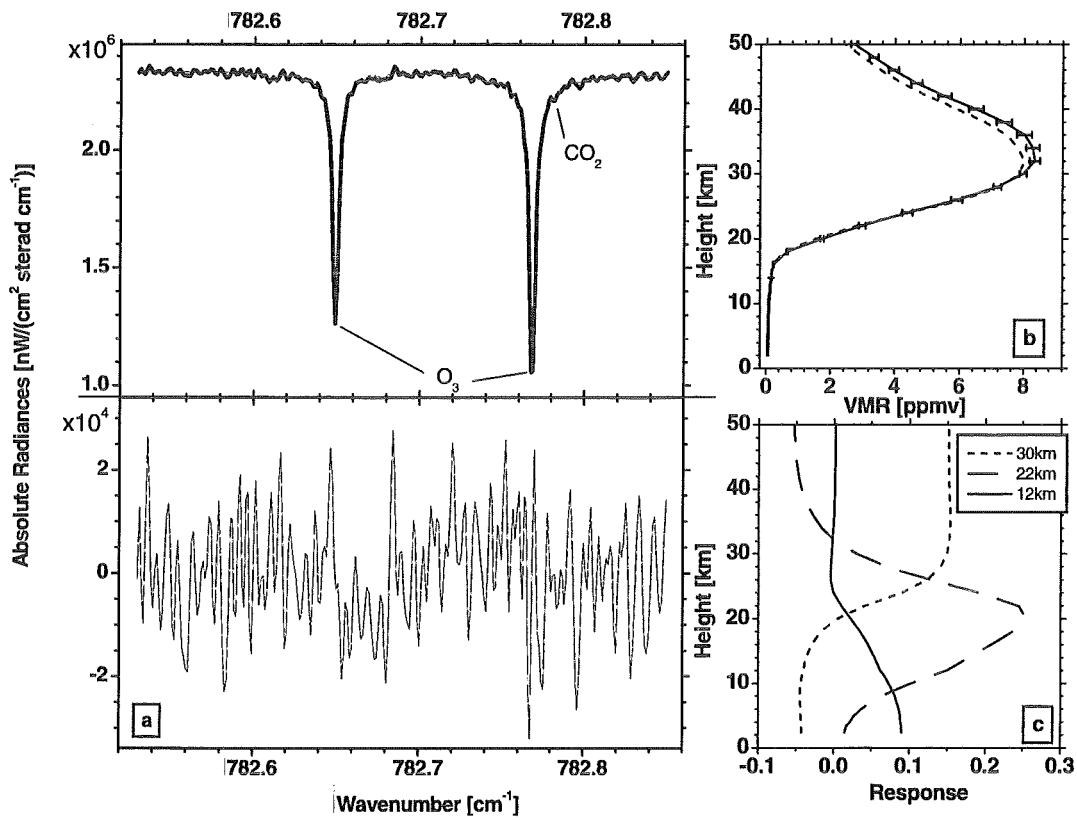
Fig. 5.14: Typical evaluation of O_3. a: Upper part shows the measured spectrum (thick line) and simulated spectrum (thin line), lower part shows the difference between both spectra; b: Applied start profile (dotted line) and retrieved profile (solid line); c: Averaging kernels for some selected heights as described in the legend.

noise	1%
SZA	$<2.5\%$
T profile	1.4% (2.5%)
interfering species	0.02% [37]
total	**3% (3.7%)**
spectroscopic data	5%

Table 5.6: Error budget for ZCAs of O_3.

5.3.6 O_3

O_3 is evaluated between $782.53\,\mathrm{cm}^{-1}$ and $782.85\,\mathrm{cm}^{-1}$. This region additionally shows weak absorption features of H_2O (wing) and CO_2. Both signatures are considered by scaling. The O_3 profile retrieval is performed by slope regularization and additionally for layers below $10\,\mathrm{km}$ by absolute regularization. It is possible to distinguish three independent layers (see Figure 5.14).

5.3.7 HF

HF is retrieved in the spectral region between $4038.85\,\mathrm{cm}^{-1}$ and $4039.05\,\mathrm{cm}^{-1}$, where additionally H_2O (wing) and CH_4 (minor signatures) exhibit absorption features. Especially at high SZA, the H_2O spectroscopic data aggravate the evaluation. In the evaluation procedure, the CH_4 signature is considered by a fixed profile only and for H_2O scaling is applied. The target gas HF is retrieved by slope regularization and for layers above $40\,\mathrm{km}$ additionally by absolute regularization in order to avoid a trend towards unrealistically high values in these regions. Three independent layers are typically retrieved.

5.3.8 HCl

HCl was evaluated by fitting two spectral intervals ($2775.69\text{-}2775.84\,\mathrm{cm}^{-1}$ and $2925.76\text{-}2926.04\,\mathrm{cm}^{-1}$) simultaneously. In the former region, also H_2O, CO_2, O_3, N_2O, CH_4, and NO_2 show absorption features with the one of O_3 being the most important. The latter is influenced mainly by the wings of a strong CH_4 line. Profiles of CO_2, N_2O, and NO_2 are kept fixed and for H_2O, O_3, and CH_4 slope regularization is applied. The target gas HCl is retrieved by slope regularization. In analogy to HF, absolute regularization is additionally used at higher altitudes in order to prevent the profile from tending towards unrealistically high values above $40\,\mathrm{km}$. The retrieval provides three independent layers.
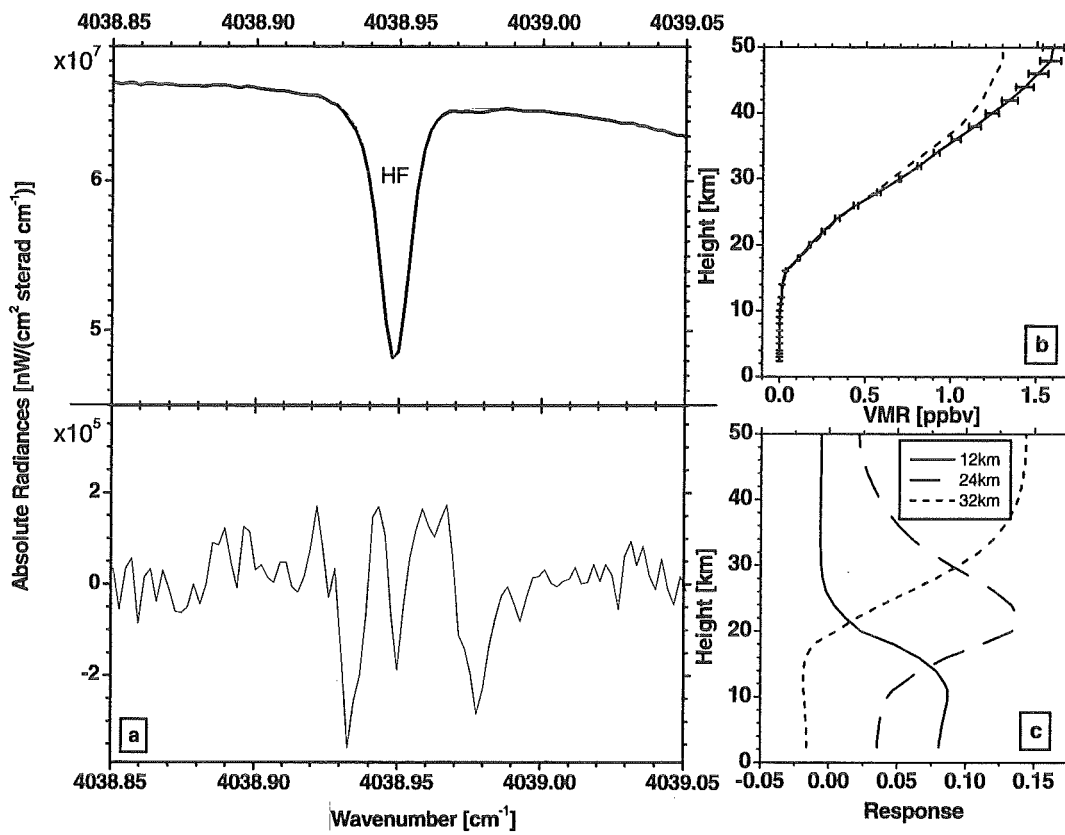
Fig. 5.15: Typical evaluation of HF. a: Upper part shows the measured spectrum (thick line) and simulated spectrum (thin line), lower part shows the difference between both spectra; b: Applied start profile (dotted line) and retrieved profile (solid line); c: Averaging kernels for some selected heights as described in the legend.

noise	≤0.4%
SZA	<2.5%
T profile	0.9% (1.7%)
interfering species	0.5%
total	**2.7%** (3.1%)
spectroscopic data	5%

Table 5.7: Error budget for ZCAs of HF.
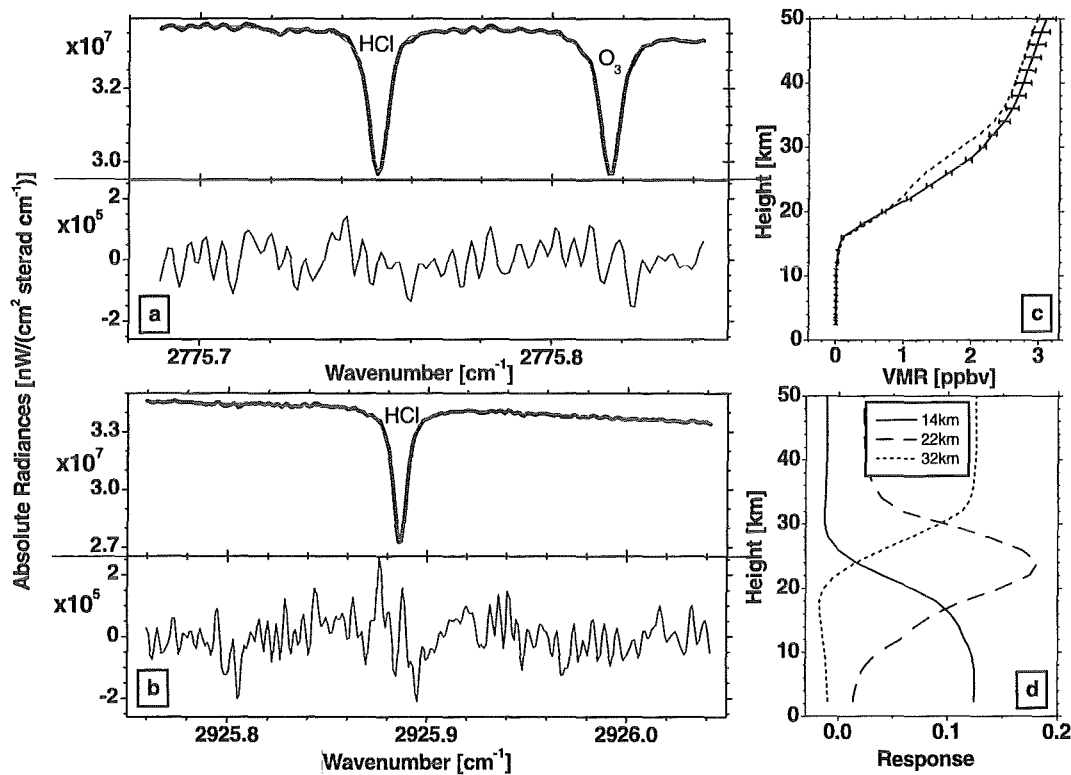
Fig. 5.16: Typical evaluation of HCl. a+b: The two applied spectral intervals are shown, whereby the upper parts show the measured spectrum (thick line) and simulated spectrum (thin line), and the lower parts show the difference between both spectra; c: Applied start profile (dotted line) and retrieved profile (solid line); d: Averaging kernels for some selected heights as described in the legend.

noise	1.5%
SZA	<2.5%
T profile	0.5% (1%)
interfering species	0.5% [37]
total	**3%**
spectroscopic data	5%

Table 5.8: Error budget for ZCAs of HCl.
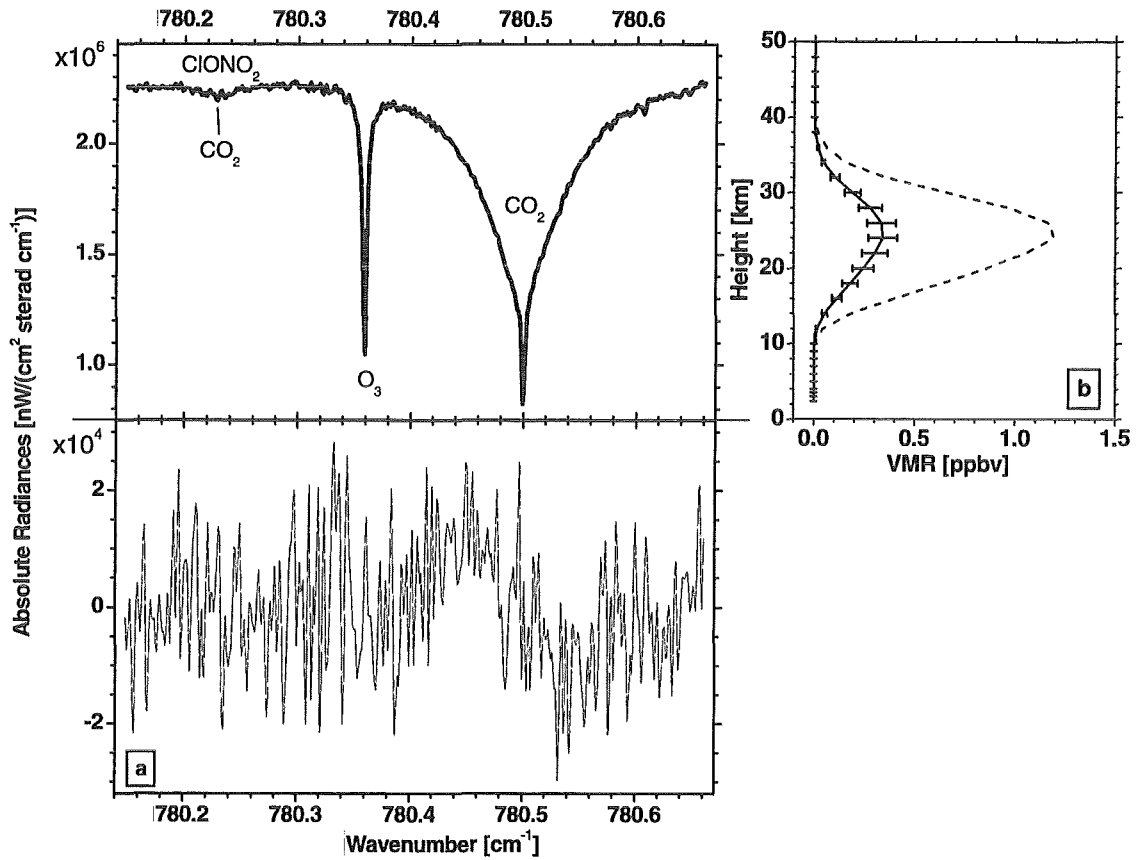
Fig. 5.17: Typical evaluation of $ClONO_2$. a: Upper part shows the measured spec-
trum (thick line) and simulated spectrum (thin line), lower part shows
the difference between both spectra; b: Applied start profile (dotted line)
and retrieved profile (solid line).

noise	12%
SZA	<2.5%
T profile	17-18% (33-36%)
VMR profile	8% [37]
interfering species	0.5% [37]
total	**23% (39%)**
spectroscopic data	10-15% [2]

Table 5.9: Error budget for ZCAs of $ClONO_2$.

5.3.9 $ClONO_2$

$ClONO_2$ is a relatively weak absorber and its absorption feature shows a strong temperature dependence. As total error we estimated 23%. It is dominated by noise and uncertainties in the temperature profile. Additionally, its absorption coefficients are subject to relatively great uncertainties (10-15%) and no pressure-dependent absorption coefficients are applied ([2]). For these reasons, merely scaling of an assumed profile is performed. This somehow arbitrary profile introduces an additional uncertainty. A spectral interval ranging from $780.15\,cm^{-1}$ to $780.66\,cm^{-1}$ was applied, where H_2O, CO_2, O_3, HNO_3, and C_2H_2 also show absorption features. While the latter two are considered by fixed profiles, the others are all dealt with by slope regularization. The significant temperature dependence determined above for $ClONO_2$ may be partly due to the interfering CO_2 line.

5.3.10 HNO_3

HNO_3 is evaluated by fitting two spectral intervals ($867.45\text{-}868.85\,cm^{-1}$ and $872.70\text{-}874.10\,cm^{-1}$) simultaneously. Other trace gases like H_2O, CO_2, OCS only show weak signatures in these regions. The spectroscopic data of HNO_3 are subject to relatively high uncertainties (15%). The signatures of CO_2 are taken into account by a fixed profile, while H_2O and OCS profiles are scaled. Slope regularization was performed to retrieve HNO_3 profiles from the FTIR measurements. Typically, three independent layers are detectable.

5.3.11 NO_2

NO_2 is a weak absorber. It is evaluated in the region between $2914.55\,cm^{-1}$ and $2914.73\,cm^{-1}$. Additional absorbers are H_2O, O_3, and CH_4. The latter has the greatest influence on this spectral region with wings belonging to lines centered at $2914.49\,cm^{-1}$ and $2914.91\,cm^{-1}$. O_3 is considered in the fitting process by a fixed profile and H_2O, CH_4 by scaling. Due to its weak signature, scaling of a NO_2 climatological profile is allowed only. Its accuracy is limited mainly by spectroscopic noise.
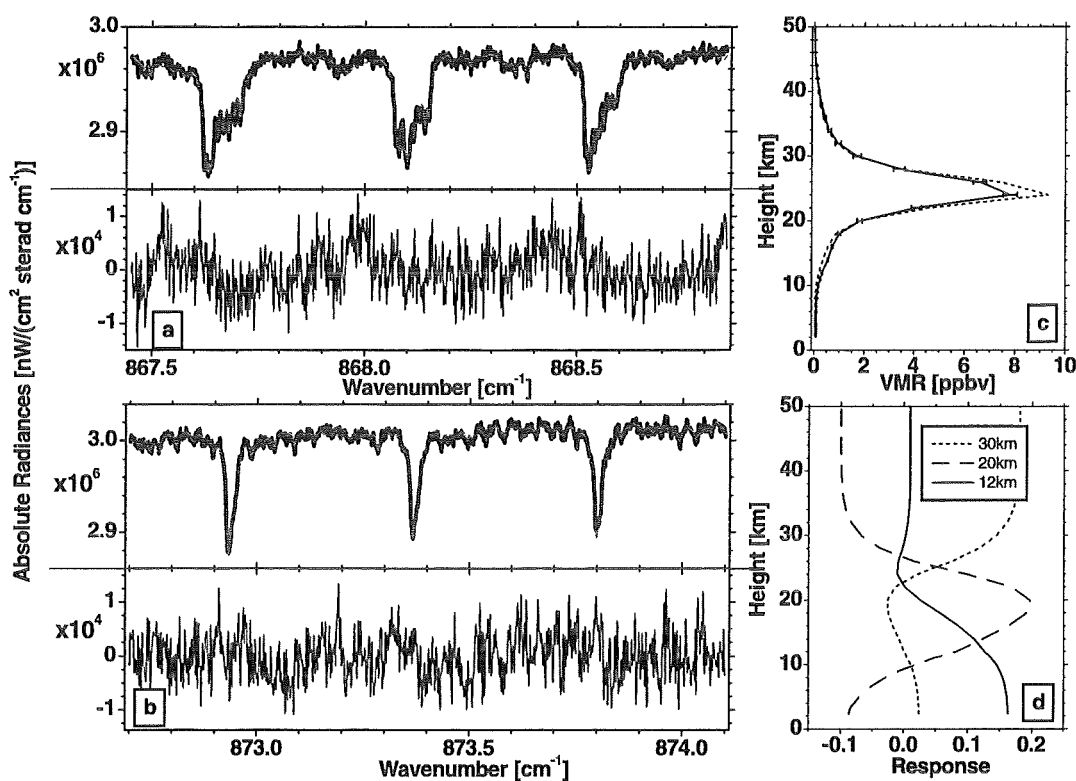
Fig. 5.18: Typical evaluation of HNO_3. a+b: The two applied spectral intervals
are shown, whereby the upper parts show the measured spectrum (thick
line) and simulated spectrum (thin line), and the lower parts show the
difference between both spectra; c: Applied start profile (dotted line)
and retrieved profile (solid line); d: Averaging kernels for some selected
heights as described in the legend.

noise	2%
SZA	<3%
T profile	1.3% (2.5%)
interfering species	0.04% [37]
total	**3.8%** (4.4%)
spectroscopic data	15%

Table 5.10: Error budget for ZCAs of HNO_3.
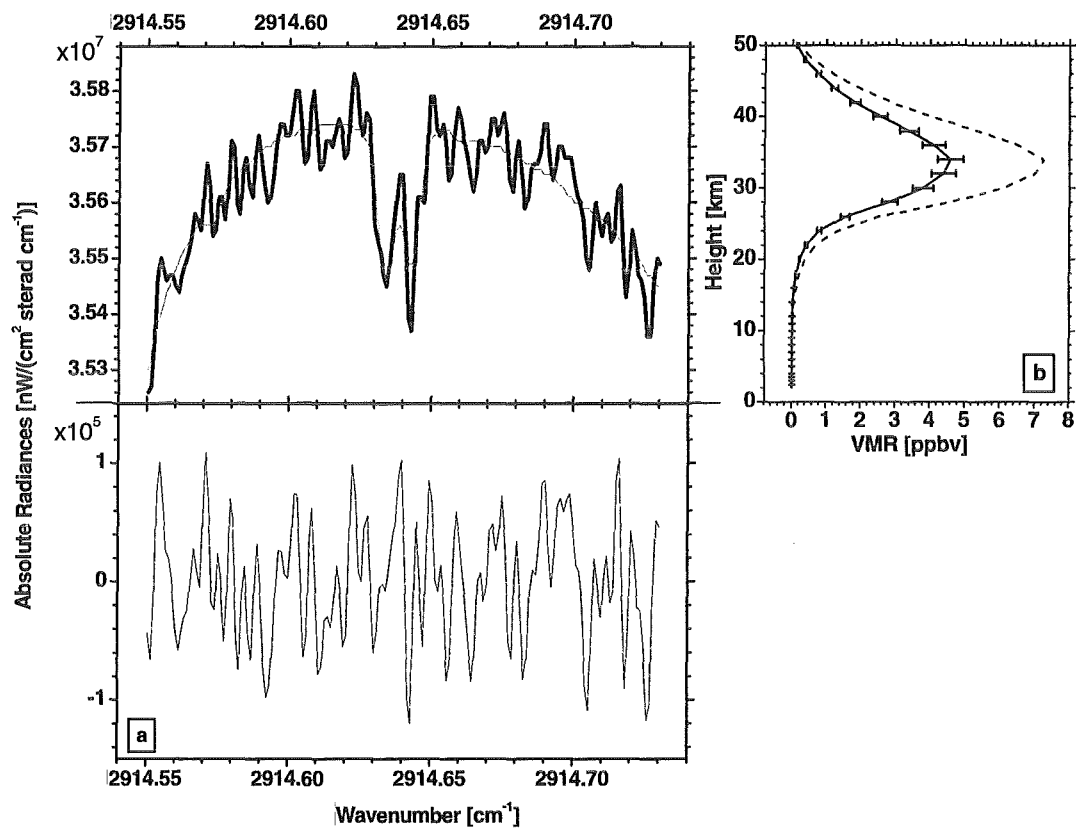
Fig. 5.19: Typical evaluation of NO$_2$. a: Upper part shows the measured spectrum (thick line) and simulated spectrum (thin line), lower part shows the difference between both spectra; b: Applied start profile (dotted line) and retrieved profile (solid line).

noise	12%
SZA	<2.5%
T profile	1.6% (2.8%)
VMR profile	5% [27]
interfering species	1%
total	**13.5%**
spectroscopic data	5%

Table 5.11: Error budget for ZCAs of NO$_2$.
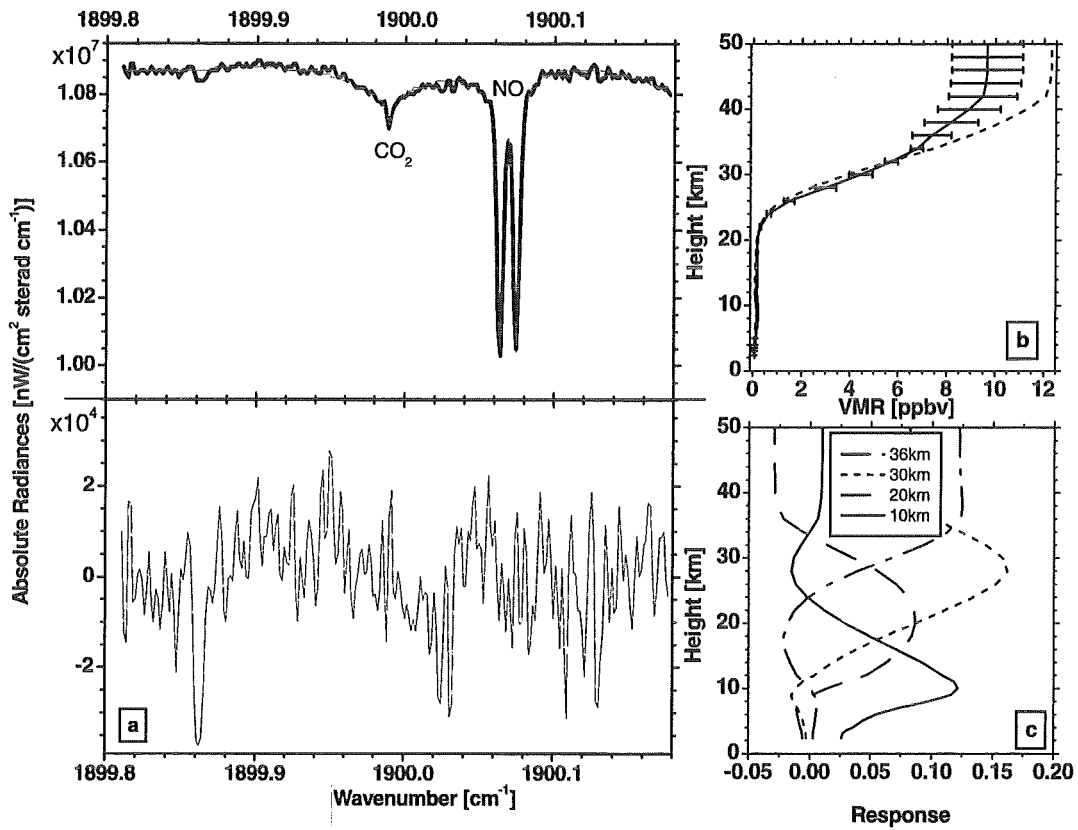
Fig. 5.20: Typical evaluation of NO. a: Upper part shows the measured spectrum
(thick line) and simulated spectrum (thin line), lower part shows the
difference between both spectra; b: Applied start profile (dotted line)
and retrieved profile (solid line); c: Averaging kernels for some selected
heights as described in the legend.

noise	1.5%
SZA	<2.5%
T profile	0.8% (1.9%)
interfering species	0.5% [56]
correction of solar line	7% (up to 20%)
total	**7.5%** (up to 20%)
spectroscopic data	5%

Table 5.12: Error budget for ZCAs of NO.

5.3.12 NO

For the evaluation of NO, we used the wavenumber interval between $1899.81\,\mathrm{cm}^{-1}$ and $1900.12\,\mathrm{cm}^{-1}$. Absorptions of other trace gases (H_2O (weak wing), CO_2, and N_2O) interfere with the NO signature (around $1900.09\,\mathrm{cm}^{-1}$). Additionally, there is a solar CO line at approximately $1900.03\,\mathrm{cm}^{-1}$, which makes the evaluations quite complicated. The solar line is corrected manually by means of the software NOKORR [27]. This procedure, however, does not always remove the solar absorption feature completely and, hence, represents a major error source in NO retrieval. For an error estimation, various spectra were corrected twice with the corrections being made independently of each other. Subsequently, both corrected spectra were inverted. Figure 5.21 shows a worst case example of these studies. The correction of the left spectrum is obviously better, yet both corrections still are acceptable. The resulting profiles and ZCA, however, differ significantly (see right panel of Figure 5.21). The left correction yields a ZCA of $3.47 \times 10^{15}\,\mathrm{cm}^{-2}$ and the right one a ZCA of $4.20 \times 10^{15}\,\mathrm{cm}^{-2}$ due to the higher tropospheric content. For the retrieval, H_2O and N_2O are kept fixed and scaling is allowed for CO_2. For NO, slope and absolute regularizations are applied simultaneously, the regularization being enforced at lower altitudes in order to limit the influences of a poorly corrected solar line. The resolution of three or even four layers, as shown in Figure 5.20, is due to strong absorption lines. But the tropospheric NO is strongly dependent on the performed correction of the solar line and, therefore, it should be questioned.
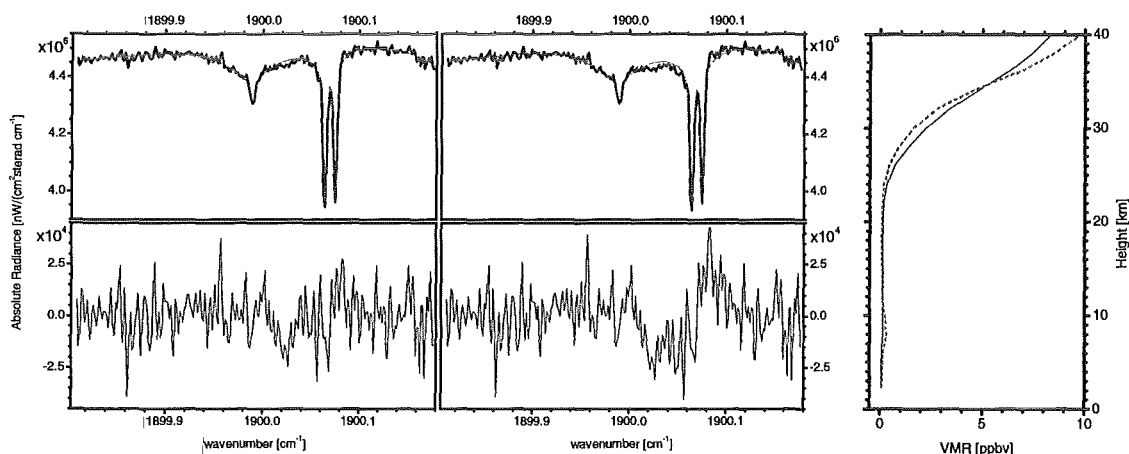
Fig. 5.21: Influence of solar line (at $1900.03\mathrm{cm}^{-1}$) on NO retrieval. Depicted are from left to right two corrections of the same raw spectrum and the resulting profiles. The solid line in the profile plot corresponds to the left spectrum, the dotted line to the right spectrum.

Chapter 6

Results

In this chapter, time series of column amounts and profiles of the retrieved trace gases from February 1999 to July 2001 are presented. The long measurement period allow to observe typical annual cycles of these gases. A classification into tropospheric and stratospheric trace gases is made. The retrieved tropospheric components are H_2O, N_2O, CH_4, OCS, and HCN. Among stratospheric trace gases, results for O_3, HF, HCl, $ClONO_2$, HNO_3, NO_2, and NO are presented. The column amounts and profiles provided by the FTIR measurements are compared with results of other instruments installed at IZO, which detect the same components. In December 1999, the POLARSTERN research vessel of the German Alfred-Wegener Institute with an FTIR spectrometer onboard passed the Canary Islands. This allows to compare all stratospheric components detected by the two instruments during that period. Additionally, the retrieved profiles and column amounts are compared to calculations of the 3-D CTM (3-dimensional chemical transport model) KASIMA (Karlsruhe simulation model of the middle atmosphere) ([62], [63]).

6.1 Time Series of Tropospheric Trace Gases

6.1.1 H_2O

Owing to its involvement in radiative processes, cloud formation, and in exchanges of energy with the oceans, H_2O plays an important role in the atmosphere. It tends to be concentrated in the lowest 2 km of the atmosphere and it decreases with altitude. This reflects its release at the Earth's surface, mainly over warm ocean surfaces, and its redistribution by atmospheric circulation and destruction at higher altitudes and at middle and high latitudes through condensation and precipitation. The abundance of H_2O at a fixed location is quite variable. It depends on the history of the air parcel residing at that location, and on the processes that
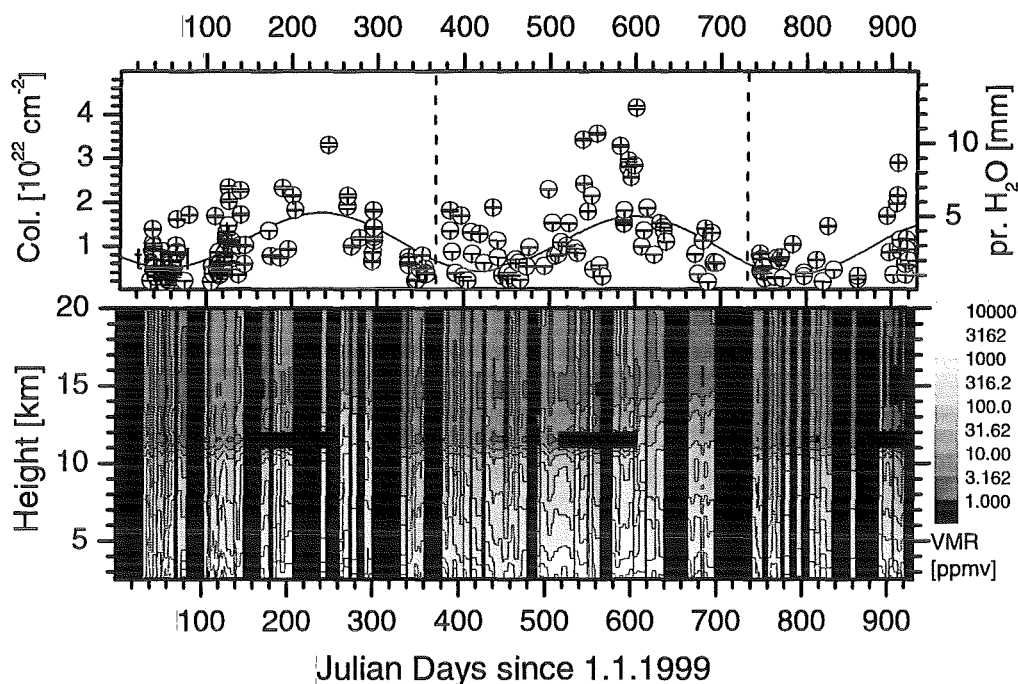
Fig. 6.1: H_2O results from February 1999 to July 2001. Above: Columns (hollow circles) and annual cycle (line) derived by fitting a sine function to the data. Below: Profiles between 2.5 and 20 km. Black means no data or VMR values below 1.0 ppmv.

influenced this air parcel. Figure 6.1 shows the retrieved H_2O column amounts and profiles from February 1999 to July 2001 above IZO and demonstrates their high variability. Highest values are reached in summer, when Earth surface and atmospheric temperatures are highest and convection is strongest. The profiles in the lower panel of Figure 6.1 are depicted in the logarithmic scale, and they demonstrate that the total column amounts are nearly solely determined by the concentrations below 5 km.

The H_2O results are additionally compared to radiosonde data. These soundings are performed twice a day (12 UT and 00 UT) from the Meteorological Center situated in the island's capital Santa Cruz de Tenerife. As shown in the preceding chapter the spectrum used for H_2O retrieval typically allows to resolve two independent levels below 10 km. The height resolution capability of the radiosonde is much better. For a reasonable comparison the original radio-profile is smoothed in order to obtain a profile with the same height resolution as the FTIR profile. For smoothing, a synthetic spectrum using the measured radiosonde H_2O profile is calculated. Subsequently, the synthetic spectrum is analyzed using exactly the same
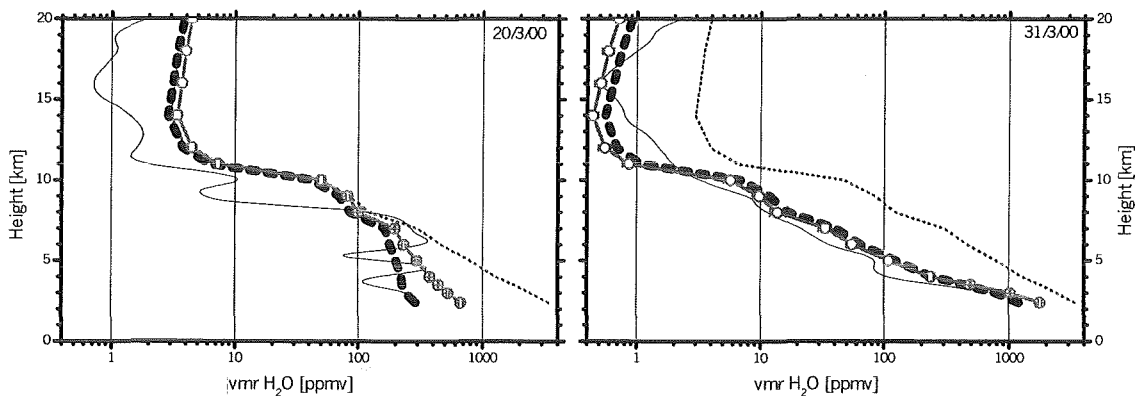
Fig. 6.2: H_2O profiles of 20/3/00 and 31/3/00. Shown are for each day original ra-
diosonde profile (thin line), radiosonde profile smoothed on FTIR height
resolution (thick dashed line), the applied start profile for FTIR retrieval
(dotted line), and the retrieved FTIR profile (solid line/open circles).

parameters and constraints as applied for analyzing the measured FTIR profile. In
Figure 6.2 the smoothed and original radiosonde profiles are compared for two dif-
ferent days (20/3/00 and 31/3/00). Those days have been chosen to demonstrate
the quality of the FTIR profiles, since on both days nearly the same column amount
was measured (3.08×10^{21} cm^{-2} and 3.15×10^{21} cm^{-2} respectively), but the height
distribution was fairly different. While on 20/3/00 there was a much lower amount
of H_2O below 4 km than on 31/3/00, the H_2O concentration above 5 km on 20/3/00
exceeded that on 31/3/00. These differences in the height distribution of H_2O is
also clearly seen in the FTIR profiles. On both days, radiosonde and FTIR profiles
are in good agreement.

Moreover a statistics was drawn up for the comparison between FTIR profiles
and the smoothed radiosonde profiles. The left panel of Figure 6.3 shows the devi-
ation between profiles for all days (152 days), where radiosonde measurements and
FTIR measurements coincide. The thick line represents a statistics of all those com-
parisons. It suggests that there is no significant difference between the radiosonde
and FTIR data, but that, at the lowest levels, FTIR values tend to exceed the ra-
diosonde values, while between 3 km and 9 km the radiosonde values exceed FTIR
values. A reason of these differences may be the difference in measurement time for
FTIR and radiosonde, since H_2O amounts could change quite rapidly. In the data
shown, there is a time difference of up to 8 h between the respective measurements.
Another explanation of the higher FTIR values on the lowest levels could be that
the sonde is launched from sea level, i.e. its profile above 2km is not influenced by
the earth surface. The FTIR instrument on the other hand is based at 2400 m a.s.l..
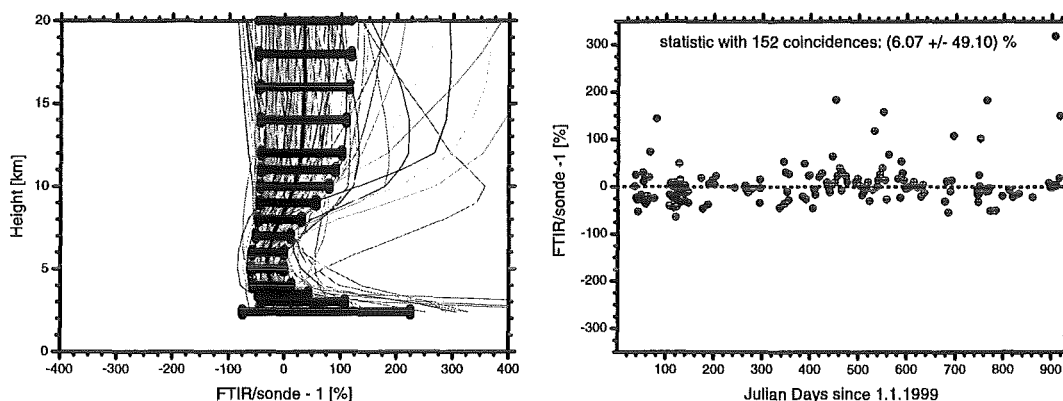
Fig. 6.3: Comparison of H_2O data from the FTIR and radiosonde. Left panel: Comparison of all coinciding FTIR and smoothed radiosonde profiles (thin lines), and a statistics of these deviations (thick lines, error bars are standard deviations from the mean). Right part: Comparison of H_2O column amounts of FTIR and radiosondes.

Therefore, topographic and surface influences on its measured H_2O up to 4 km are still expected. For example, the temperature on the lowest levels above IZO is assumed to be higher than in the free atmosphere, which probably will lead to higher H_2O abundances. In the right panel of Figure 6.3 the difference of the column amounts derived with the FTIR and by the sondes is depicted. On the average, the FTIR values are larger than the radiosonde values. However, the standard deviation from the mean (49.1%) is so large that the difference is not significant. From 6.3, it becomes evident that on some days the FTIR column amounts are more than 200% larger than the radiosonde column amounts. These days are mainly responsible for the large standard deviation from the mean. These large differences may be explained by the greater topographic and surface influences on the lowest levels of the FTIR amount and the time and spatial difference between the measurements as discussed above.

6.1.2 N_2O

N_2O is produced primarily by natural means related to bacterial processes in soils. Anthropogenic sources include nitrogen fertilizers and combustion of fossil fuel. N_2O is long-lived and, therefore, well mixed in the troposphere. In the stratosphere, it decreases with altitude due to dissociation by solar radiation or reaction with $O(^1D)$ to NO. It represents the primary source of stratospheric NO which can destroy ozone catalytically. N_2O also acts as greenhouse gas, but much less than CO_2. Figure 6.4 demonstrates the time series of the column amounts and profiles of

FTIR and KASIMA. The total column amount FTIR data exhibit a strong day-to-day variability in particular during 1999 and 2001. These variations mainly come from the troposphere, as is suggested by the more defined time series of the column amount above 11 km. Since especially in the first part of 1999, measurements were conducted in a wide range of SZA (including very high SZA) a mismatch of the sun tracker (as described in chapter 5) may partly be responsible for these variations. On the other hand, in situ measurements of e.g. CH_4, CO_2, and O_3 performed at IZO also show strong diurnal variations ([67]), which are attributed to local upward blowing winds, which penetrate the inversion layer below the Observatory. This occurs especially during wintertime, when the inversion layer is weak. As a result, the measurement site is often influenced by local biogenic or anthropogenic activities taking place in the lowland areas surrounding the Observatory. In 2000, all measurements were performed at similar SZA and no strong variations in the total column amount are observed. The stratospheric column amount peaks in late summer and has a minimum in winter/spring, which could be explained by enhanced upwelling in summertime, which is confirmed by the rising VMR isolines in the plotted profiles. The stratospheric column amount of KASIMA and FTIR are in good agreement, both concerning its absolute values and its annual cycle. Both KASIMA and FTIR profiles show an annual cycle with ascending VMR isolines from May to October and isolines situated at a relative low altitude in winter (November to April). The winter period is also characterized by a high variability of those isolines which is due to transport processes (see also chapter 2). The KASIMA profiles show the same characteristics. However, as demonstrated by the lowest panel of Figure 6.4 KASIMA retrieves generally lower VMR values as the FTIR below 20 km. Above 28 km, the KASIMA VMR values are generally higher than the FTIR ones.
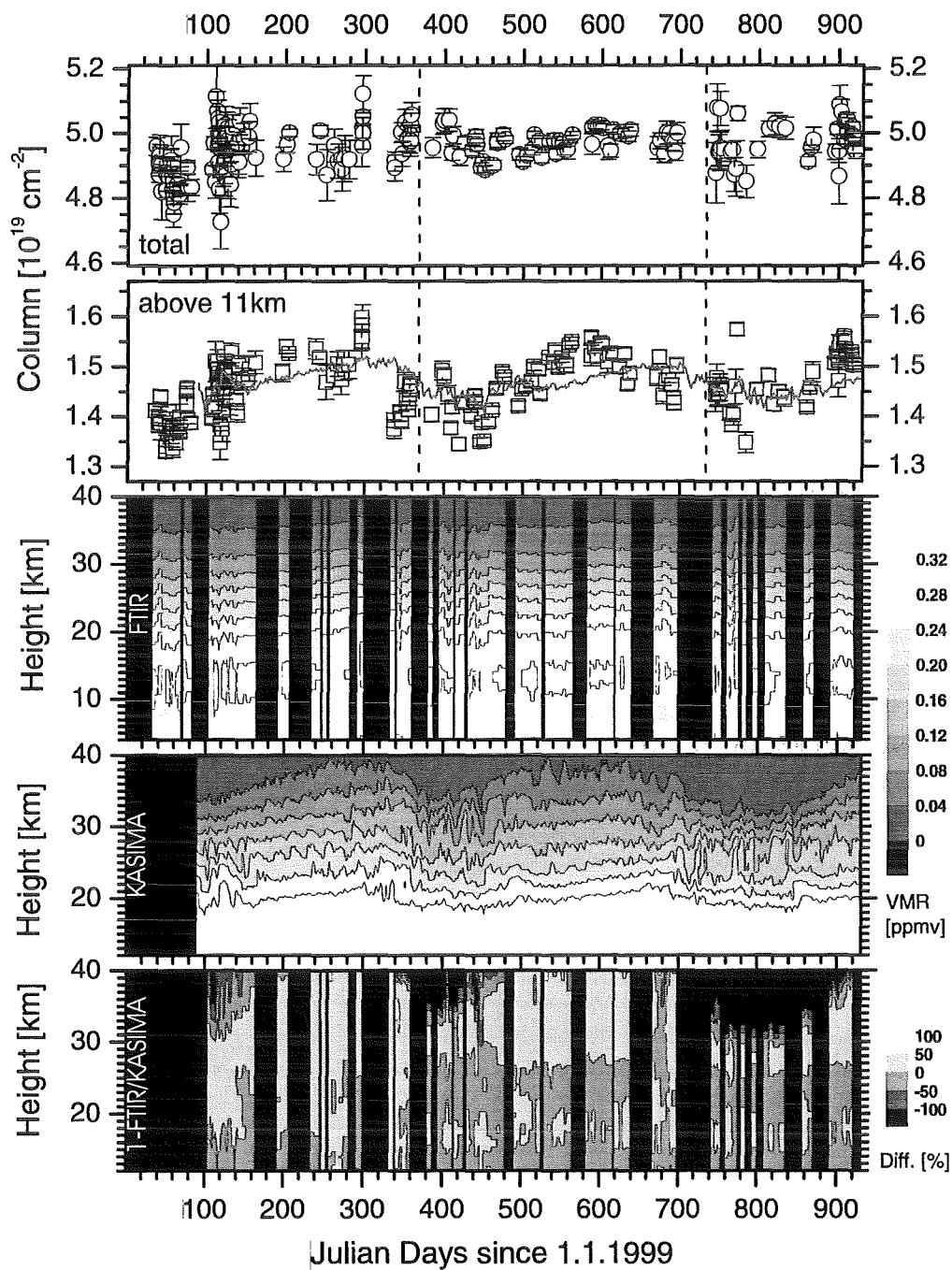
Fig. 6.4: N$_2$O results from February 1999 to July 2001. From above to below:
Total column amounts of FTIR (open circles); stratospheric column
amounts of FTIR (open squares) and KASIMA (solid line); FTIR pro-
files from 4-40 km; KASIMA profiles from 12-40 km; difference between
KASIMA and FTIR profiles from 12-40 km. Black means no data.
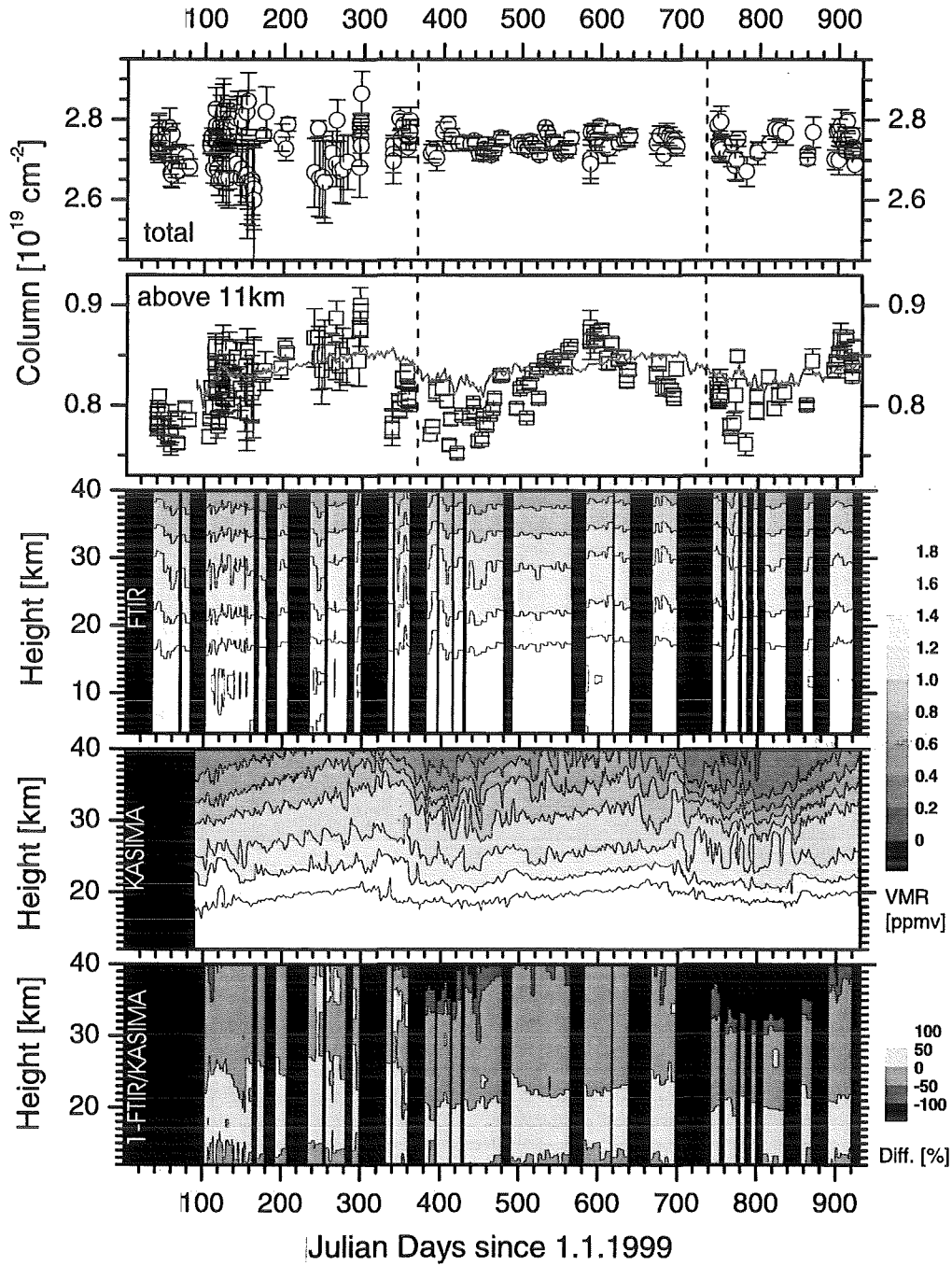
Fig. 6.5: CH$_4$ results from February 1999 to July 2001. From above to below: Total column amounts of FTIR (open circles); stratospheric column amounts of FTIR (open squares) and KASIMA (solid line); FTIR profiles from 4-40 km; KASIMA profiles from 12-40 km; difference between KASIMA and FTIR profiles from 12-40 km. Black means no data.

6.1.3 CH_4

Like N_2O, methane (CH_4) is primarily produced by bacterial and surface processes that occur naturally. However, anthropogenic sources such as mining, industrial activities or intensive agriculture may constitute as much as 35% of CH_4 production. It is also long-lived and, therefore, well mixed in the troposphere. In the stratosphere, it decreases with altitude as a result of oxidation, which ultimately leads to the formation of stratospheric H_2O. In Figure 6.5 time series of column amounts and profiles of CH_4 are shown. As for N_2O, strong variability is seen in the total column amount, and comparison to the stratospheric column amount suggests that these variations are also caused in the troposphere. They are also due to instrumental uncertainties and local diurnal atmospheric alterations. Stratospheric column amounts show a similar cycle as in the case of N_2O with highest values in late summer/fall and lowest values in winter/spring. Columns of FTIR and KASIMA are in good agreement. Profiles of CH_4 behave very similarly to profiles of N_2O: Gradual ascent of isolines in summer (May to October) and relatively low values during the winter period (November to April). As before, this is due to enhanced upwelling during summer. There also is a higher variability in winter, caused by stronger wave activity during this period. In contrary to N_2O, CH_4 profiles of KASIMA show a higher VMR below 20 km and a lower VMR above 24 km.

6.1.4   OCS

The principal sources of OCS are oceans, soils, wetlands, and biomass burning, and the major sinks represent uptake by vegetation and atmospheric oxidation. Since OCS is rather inactive in the troposphere, it represents a major reservoir of sulfur. In the troposphere it is distributed uniformly and in the stratosphere its amount decreases with height. There, it is oxidized via SO_2 to sulfate aerosols which are supposed to potentially cause catalytic ozone loss on a global scale [69]. Figure 6.6 shows the column amounts and profiles of OCS from February 1999 to July 2001. The observed increase of the VMR values with height in the troposphere may be artificially produced due to interferences with a CO_2 absorption line as discussed in section 5.3.4. A fitted sine function suggests an annual cycle with maximum values in late spring and lowest values in late autumn. This differs from [22], where the analysis of 905 measurements conducted in Lauder (New Zealand) and Wollongong (Australia) between 1993 and 1997 provides a cycle peaking in the late southern hemisphere summer (January/February). There, it is also demonstrated that the cycles are partly an artifact variation due to spectral fitting, when seasonal changes in the shape of the profile are disregarded, i.e. when the same profile is used for all seasons. As described in the preceding chapter, the OCS data shown here were retrieved with the profiling option, as a result of which this kind of artifact should
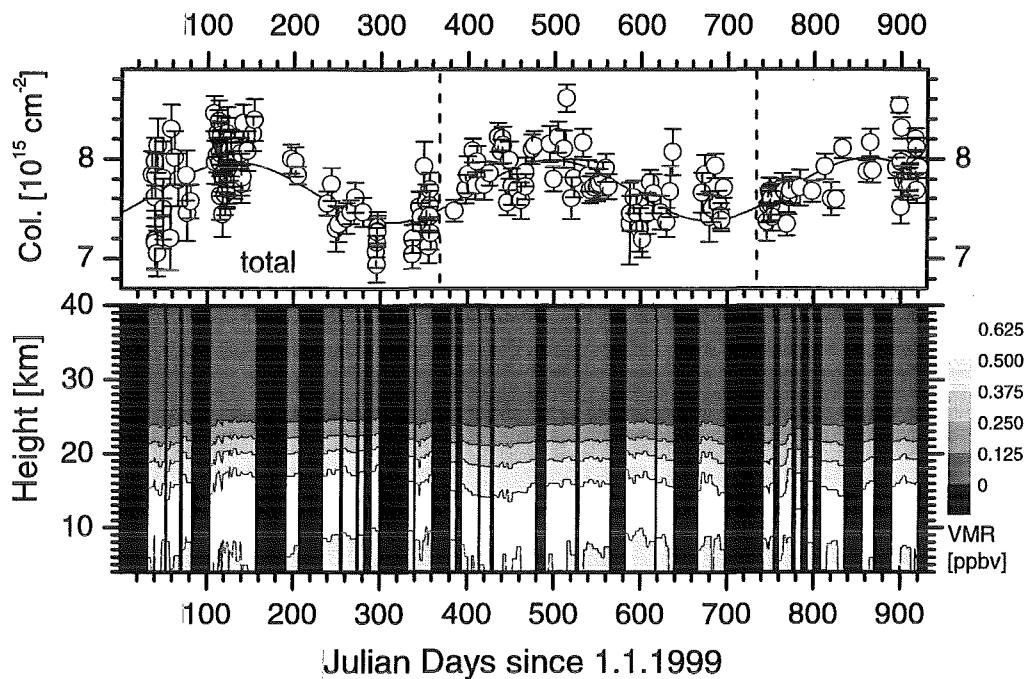
Fig. 6.6: OCS results from February 1999 to July 2001. Above: Columns (hollow circles) and annual cycle (line) derived by fitting a sine function to the data. Below: Profiles between 4 and 40 km. Black means no data.

be reduced. And indeed, the profiles demonstrate the same seasonal behavior as the N_2O and CH_4 profiles, which have a better height resolution. The ascent in summer and the descent in the winter are due to variations in long-term upwelling patterns and changes in the height of the tropopause. In the next chapter, it is additionally shown that the 0.5 ppbv isoline of OCS at roughly 16 km correlates with the tropopause height. As can be seen in the lower panel of Figure 6.6, the derived OCS profiles suggest an OCS cycle of tropospheric VMR with highest values from March to June. A combination of the two cycles (variations in upwelling and tropospheric VMR) determines the observed long-term variation of the total column amount. The peak of the tropospheric cycle from March to June may be partly due to a warm ocean source combined with winds from the Atlantic region southwest of Tenerife, which are more frequent in the troposphere in this season. The minimum from July to October may then be explained by a land-based sink of OCS, since in this season winds from the African continent are more frequent (see Figure 4.5). Both ocean source and land sink are also discussed in [22].
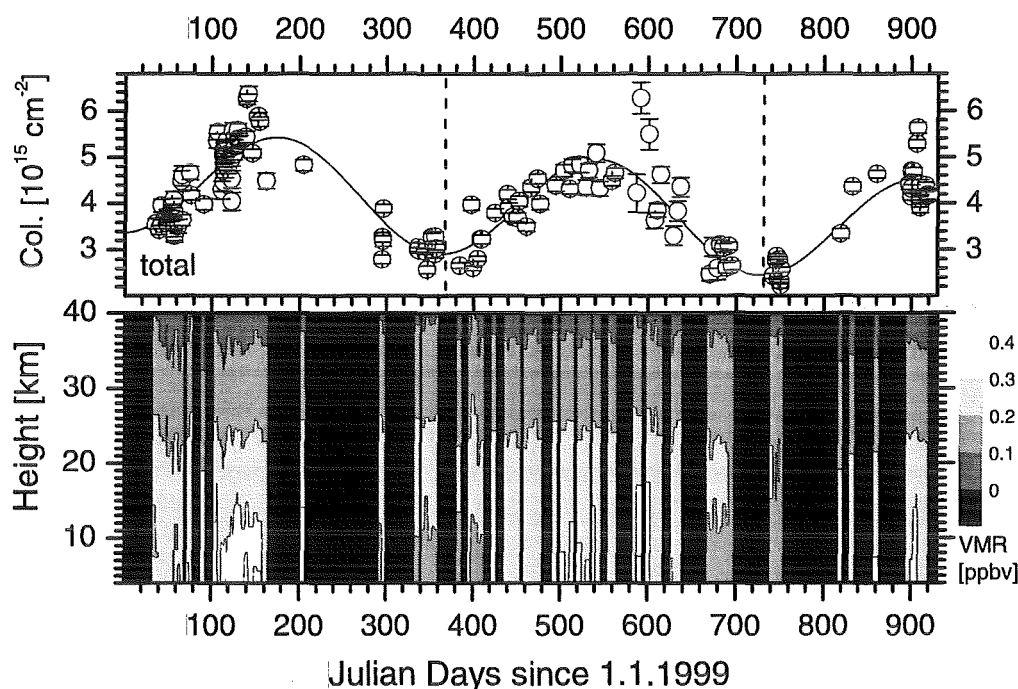
Fig. 6.7: HCN results from February 1999 to July 2001. Above: Columns (hollow circles) and annual cycle (line) derived by fitting a sine function to the data. Below: Profiles between 4 and 40 km. Black means no data.

6.1.5 HCN

HCN is also produced by plants and fungi, but the major source is believed to be biomass burning. Recently, it was demonstrated that HCN shows strong variability in the upper troposphere [58]. In the stratosphere, it decreases with height. In Figure 6.7, the column amounts and profiles of HCN from February 1999 to July 2001 are shown. A fitted sine function indicates a seasonal cycle that peaks in late spring/summer. This is in agreement with other measurements (see e.g. [52] and references herein). The profiles indicate that this is caused by enhanced upwelling (e.g. from March to June 1999, the 0.2 ppbv isoline ascends) and by higher concentrations in the troposphere. Sometimes, there are abrupt increments in ZCA (e.g. late May 1999 or August 2000). The profiles suggest that the reason may be a sudden change in tropospheric concentrations, which may be due to transport to IZO of airmasses that have been influenced by biomass burning. But we also have to keep in mind that uncertainties in the temperature profile may also be responsible for these high VMR values in the troposphere (see preceding chapter). Additionally, we observed a gradual decrease of the column amount of HCN from February 1999

to July 2001. However an observation time of $2\frac{1}{2}$ years only might be too short for deriving trends.

6.2   Time Series of Stratospheric Trace Gases

6.2.1 O_3

Figure 6.8 shows the evolution of the column amounts and profiles of O_3 during the measurement period. The sine function fitted to the total column amount data peaks in April/May and shows a minimum in October. The stratospheric column amounts describe a similar cycle, but with a lower day-to-day variability. KASIMA and FTIR stratospheric column amounts are in good agreement. The differences at the beginning of the modelled time series may be attributed to initialization problems of the model. As for the other gases, the FTIR O_3 profile shows a gradual, smooth increase of isolines in the lower stratosphere from May to October and a decrease from November to April, which is due to enhanced upwelling in summer. The ascent of VMR isolines in summer is also observed in the KASIMA profiles. Although the stratospheric column amounts of KASIMA and FTIR are in good agreement, the profiles show constant differences (lowest panel of Figure 6.8): From 18 to 25 km, where the concentration maximum of O_3 is located, KASIMA derives lower VMR values as the FTIR. Around the VMR maximum, however, which is the altitude region where O_3 is produced by photodissociation of O_2 (Chapman cycle, equations 2.14-2.17), KASIMA values exceed FTIR values. In order to test if these differences are only an artifact due to the lesser height resolution of the FTIR profile as compared to the KASIMA profile, we also made a comparison with the profiles measured by the O_3 sonde, which are certainly better resolved than the KASIMA data. The result is shown in Figure 6.9. It confirms the observations made by the FTIR data, i.e. between 18 and 25 km both sonde and FTIR exhibit higher VMR values than KASIMA.
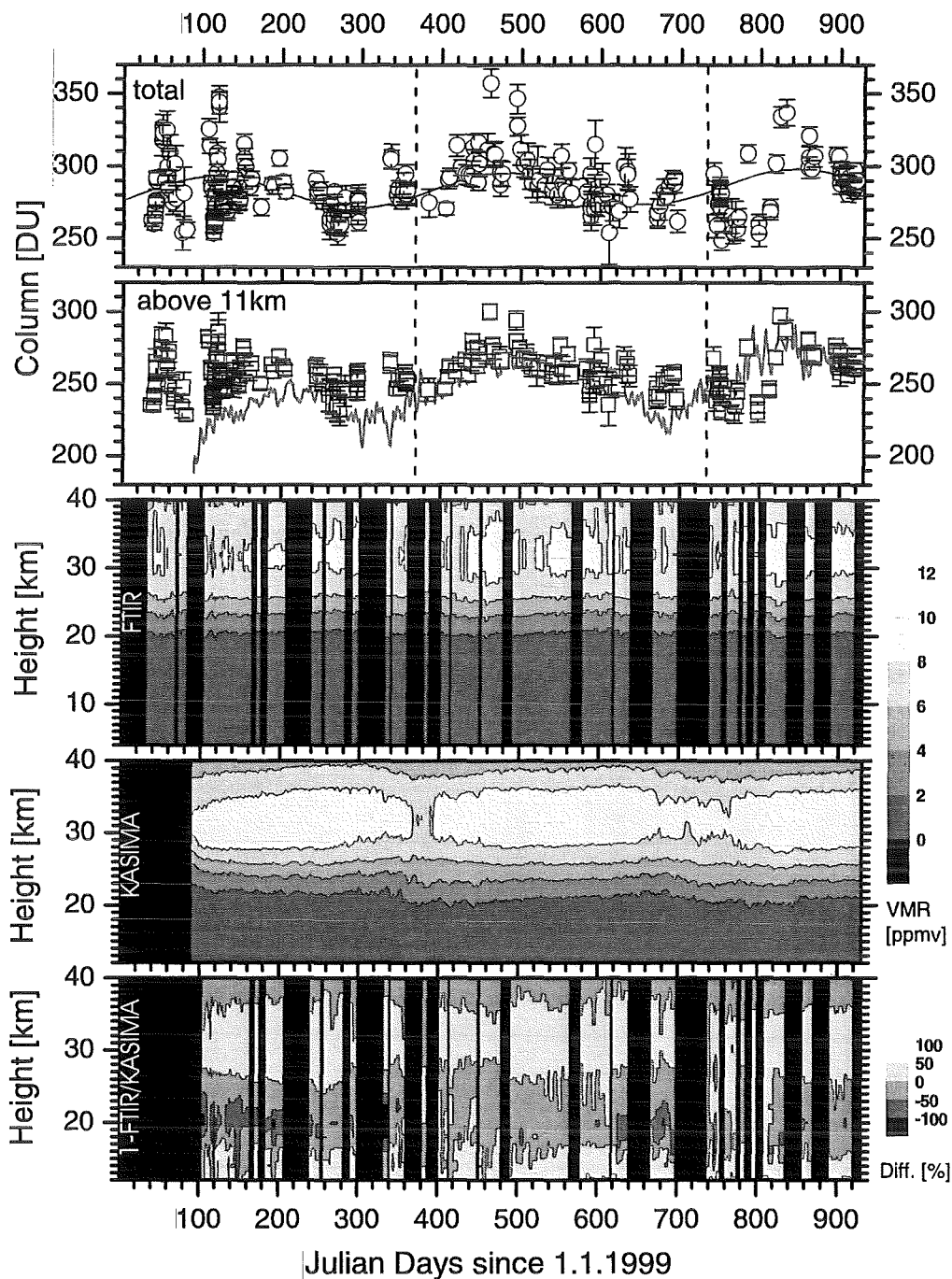
Fig. 6.8: O_3 results from February 1999 to July 2001. From above to below: Total column amounts of FTIR (open circles) and fitted sine function (solid line); stratospheric column amounts of FTIR (open squares) and KASIMA (solid line); FTIR profiles from 4-40 km; KASIMA profiles from 12-40 km; difference between KASIMA and FTIR profiles from 12-40 km. Black means no data.
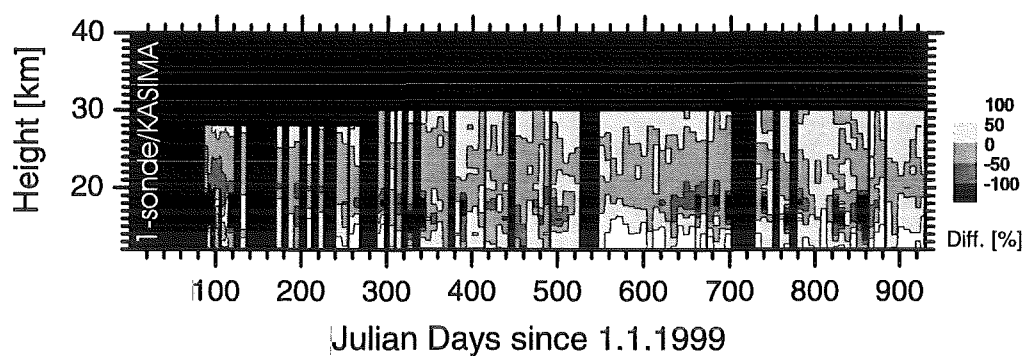
Fig. 6.9: Comparison of the KASIMA and the sonde O_3 profiles from February
1999 to July 2001 (same scale as in lowest panel of Figure 6.8). Black
means no data.
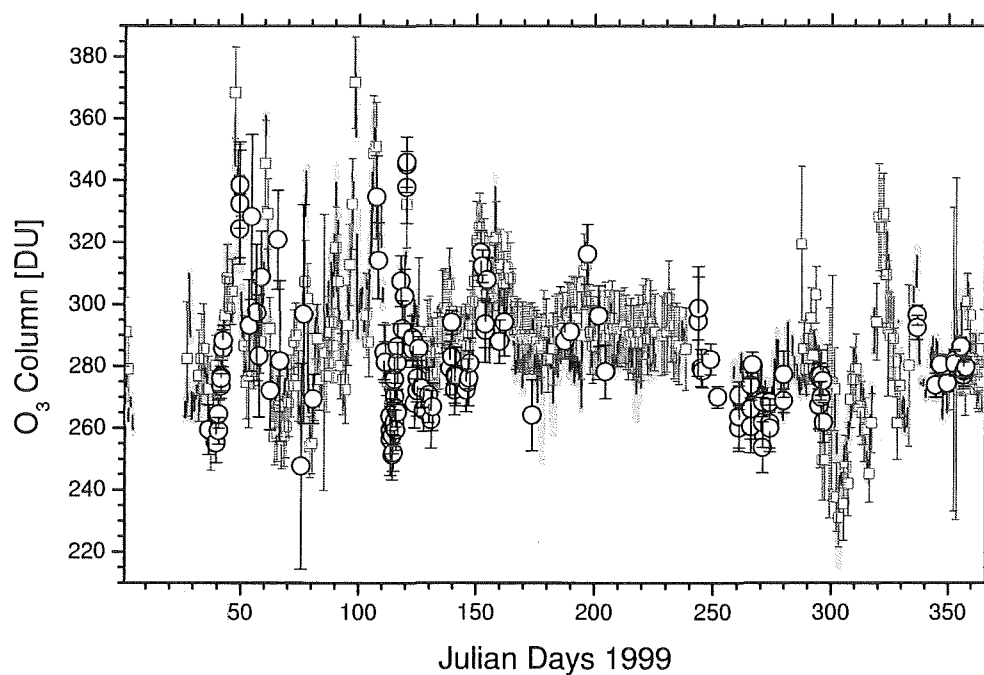
Fig. 6.10: Columns of O_3 derived by Brewer (thin line, grey area around the line
represents the error), column amounts of O_3 derived from DOAS mea-
surements (hollow squares) and from FTIR measurements (hollow cir-
cles).

Besides the FTIR, other instruments also measure the total column amount of O_3. These are a Brewer spectrometer and a DOAS (Differential Optical Absorption Spectroscopy) spectrometer. Additionally, the ozone sondes launched weekly could be used to determine the total ozone column amount. We compared the column amounts derived by these measurements with the results of the FTIR measurements. As an example, Figure 6.10 shows the column amounts determined in 1999 by the Brewer, the DOAS, and the FTIR. The three measurements are in good agreement. A statistics of the comparison over the whole period strongly supports this. In Figure 6.11, the normalized differences between the FTIR and Brewer results and between the FTIR and DOAS results, respectively, are depicted. On 204 occasions, FTIR and Brewer measurements coincide and a statistics provides a mean difference of $(1.03 \pm 3.95)\%$, i.e. the two values do not differ significantly. The comparison with DOAS data was made on 161 coincidences and yields a mean difference of $(1.03 \pm 4.73)\%$, which also means that there is no significant difference between the DOAS and FTIR results.
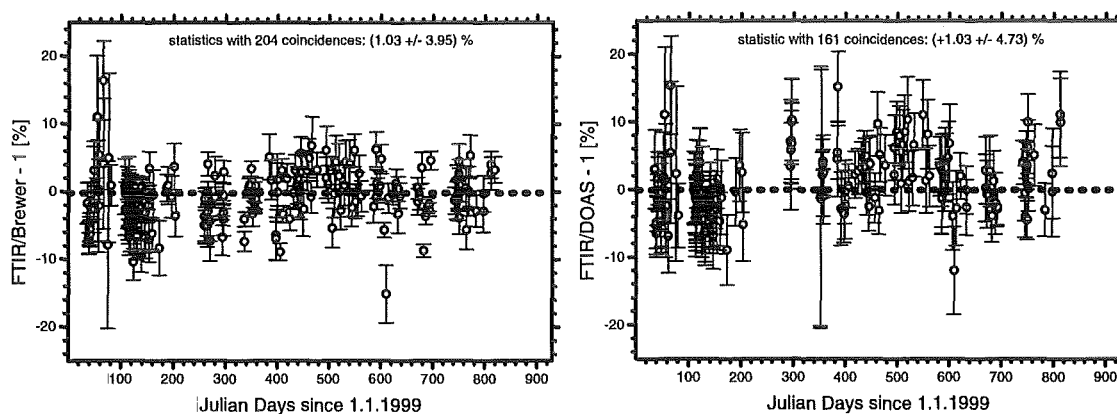
Fig. 6.11: Left panel: Differences between the FTIR and the Brewer O_3 data. Right panel: Differences between the FTIR and the DOAS O_3 data.

As in the case of H_2O, where daily radiosondes were used, we compared the O_3 sonde and the FTIR O_3 data. The FTIR measurements allow to distinguish between three independent levels, as shown in the previous chapter, whereas the resolution of the sonde is much better. For comparison, it is therefore necessary to smooth the sonde profiles. This was done in analogy to the H_2O radiosonde profiles, i.e. calculation of a synthetic spectrum with the sonde profile as input, and subsequent evaluation of this spectrum with the same parameters as in the case of the measured spectrum provides a sonde profile that corresponds to the FTIR profile in terms of height resolution. In Figure 6.12, profiles for 16/4/99 and 23/4/99 measured by an O_3 sonde and determined by the FTIR instrument are depicted. For

both situations, sonde and FTIR profiles are in good agreement. Both indicate an ascent of the tropopause between 16/4/99 and 23/4/99.
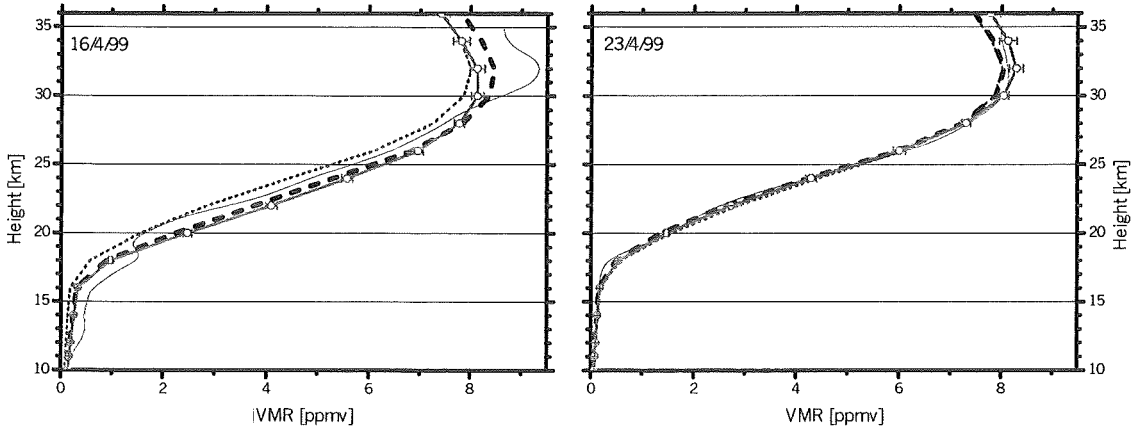
Fig. 6.12: O_3 profiles for 16/4/99 and 23/4/99. Shown are for each day original sonde profile (thin line), sonde profile smoothed on FTIR height resolution (thick dashed line), the applied start profile for FTIR retrieval (dotted line), and the retrieved FTIR profile (solid line/open circles).
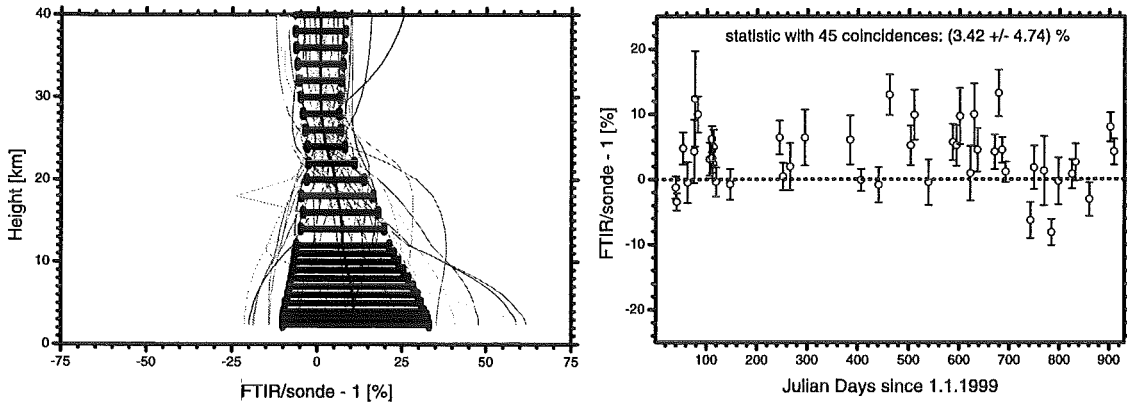
Fig. 6.13: Comparison between sonde and FTIR O_3. Left panel: Differences between all coinciding FTIR and sonde profiles (thin lines) and statistics (thick line). Right panel: Differences between the O_3 column amounts derived from sonde data and FTIR.

As shown in the left panel of Figure 6.13, the agreement between the FTIR and the smoothed sonde profiles is good. Although in the troposphere the FTIR profiles show as a mean 10% higher VMR values than the sonde profiles the statistics with

all 45 comparisons during the measurement period does not suggest any significant differences on any level. Finally, O_3 column amounts were calculated from the sonde data. For this purpose O_3 values above the sonde's peak altitude were approximated to climatological satellite data. In the right panel of Figure 6.13, the FTIR and sonde column amounts are compared. This comparison also does not reveal any significant difference between the two techniques, however, as a mean the FTIR column amounts are about 3.5% higher than the sonde values.

6.2.2   HF

HF is produced in the stratosphere following the photodissociation of fluorine-containing source gases, such as chlorofluorocarbons (CFCs). In the stratosphere, HF is long-lived and the only known sink is transport to the troposphere, followed by rainout. The long lifetime of HF prevents fluorine chemistry, in contrast to chlorine chemistry, from being a significant sink for stratospheric ozone. HF therefore is an useful tracer of stratospheric motion and frequently employed as a reference for chemically more active tracers. Figure 6.14 depicts the column amounts and profiles derived from the FTIR measurements and from KASIMA. Similar to O_3 the total column amount peaks in late spring and shows minimum values in autumn. A very small amount of HF can be found in the troposphere only and, hence, its total and stratospheric column amounts are nearly the same. Comparison of the latter with KASIMA data shows a good agreement. The FTIR profiles indicate that the annual cycle is mainly due to an ascent of the HF VMR isolines from May to October and a descent from November to April. The ascent of isolines is due to enhanced upwelling in the summer period. But besides this dynamic process there is a further process responsible for the low HF values in the lower stratosphere in summer: From May to October the stratosphere above IZO is tropically influenced, and since transport from the troposphere into the stratosphere occurs mainly in the tropics, it is composed of relatively young airmasses during this period. Hence, there still is a decisive amount of fluorine in the form of the CFC reservoirs, which gradually decompose to HF only. The winter period (November to April) is characterized by a high variability, and both the lowest and highest values registered fall into this period. This variability is mainly due to horizontal transport processes. Both tropical airmasses (e.g. low values in February 2001) and polar airmasses (e.g. high values in February 1999) are observed during this period. But also the tropopause height which is quite variable in those latitudes from November to May contributes to this variability. In the following chapter, we have a closer look on these horizontal and vertical transport processes. KASIMA provides very similar profiles. The difference between KASIMA and FTIR of more than 100 % below 16 km is somehow misleading, since the absolute values are very small.
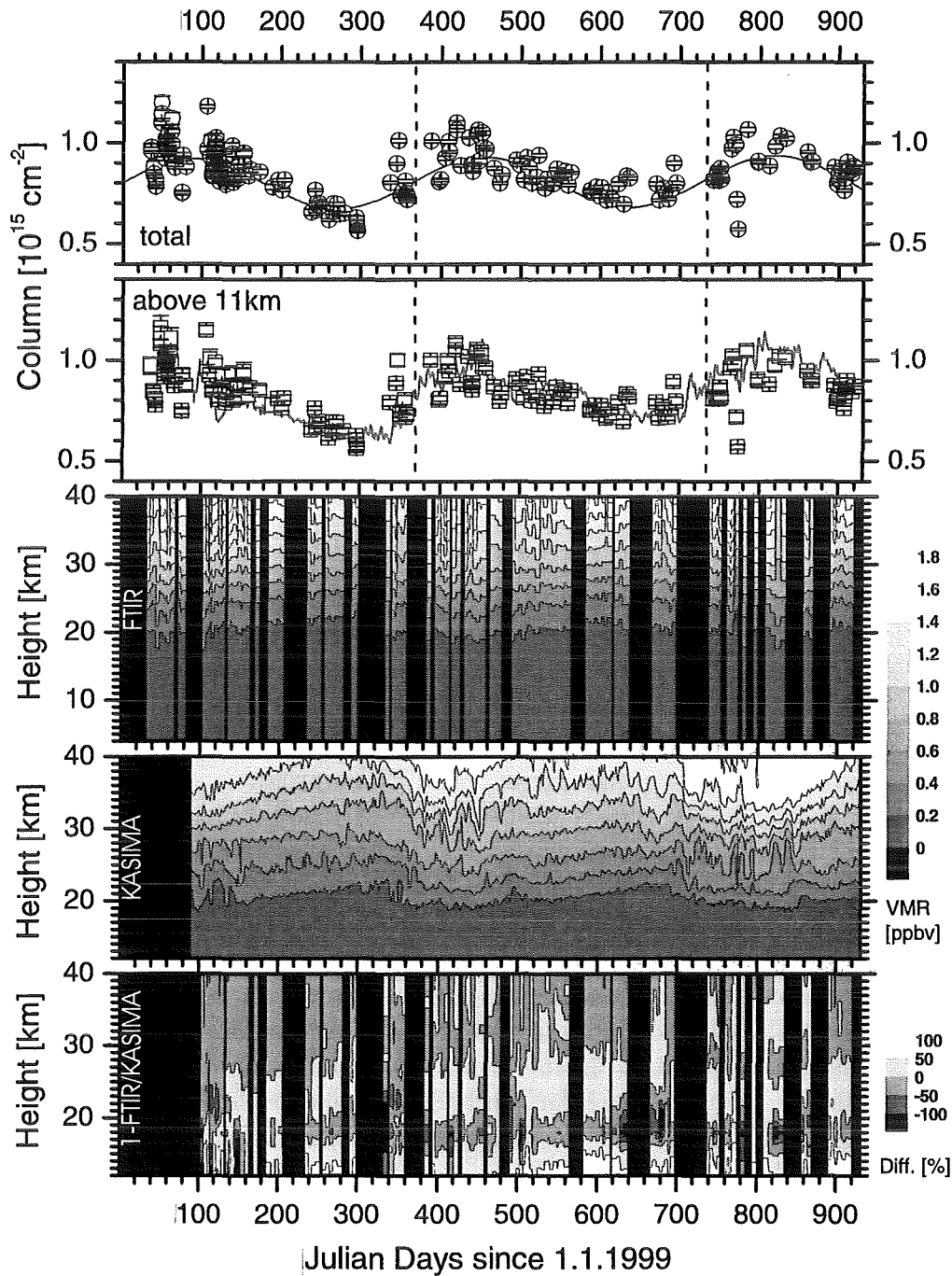
Fig. 6.14: HF results from February 1999 to July 2001. From above to below:
Total column amounts of FTIR (open circles) and fitted sine function
(solid line); stratospheric column amounts of FTIR (open squares) and
KASIMA (solid line); FTIR profiles from 4-40 km; KASIMA profiles from
12-40 km; difference between KASIMA and FTIR profiles from 12-40 km.
Black means no data.
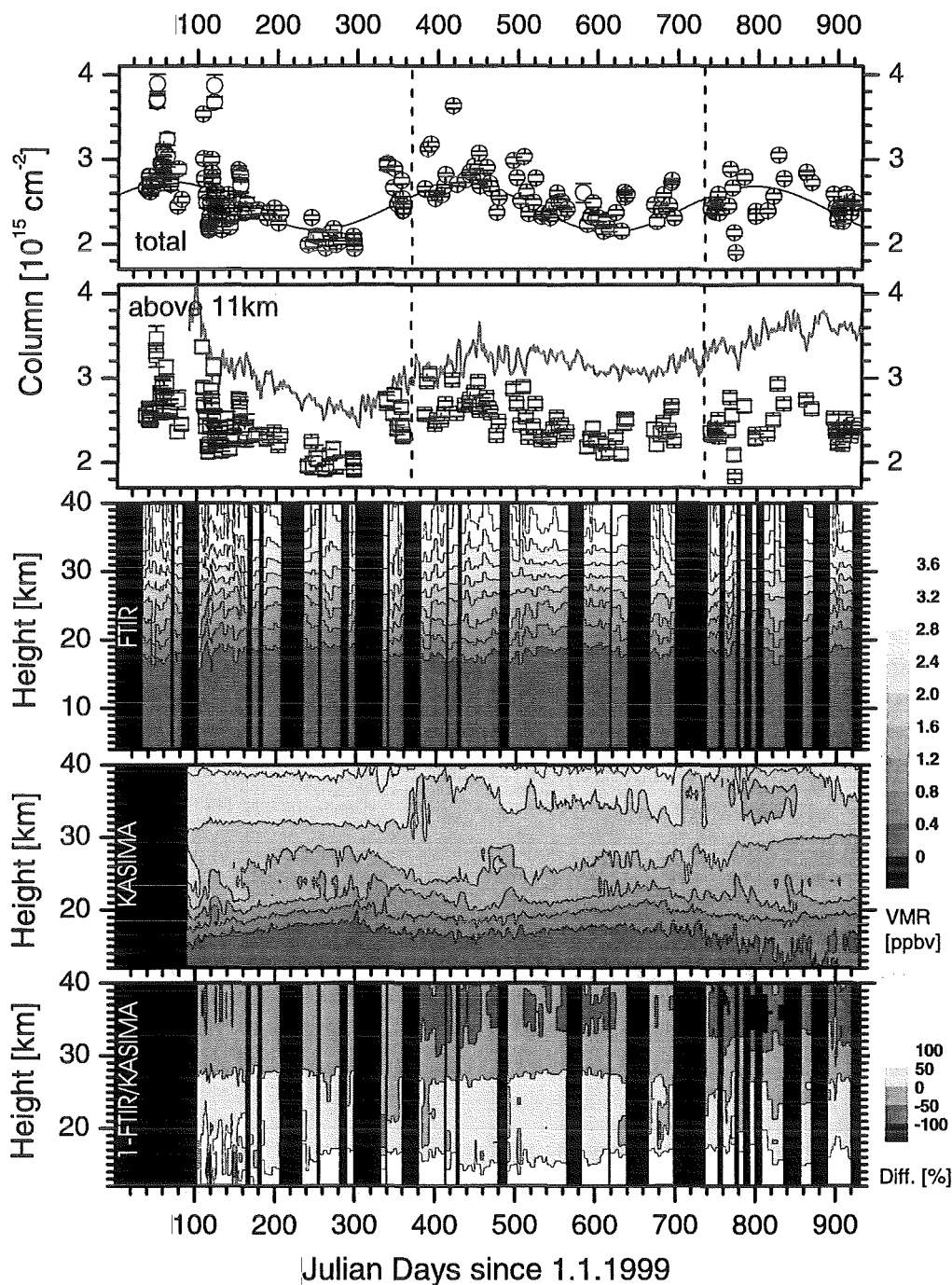
Fig. 6.15: HCl results from February 1999 to July 2001. From above to below: Total column amounts of FTIR (open circles) and fitted sine function (solid line); stratospheric column amounts of FTIR (open squares) and KASIMA (solid line); FTIR profiles from 4-40 km; KASIMA profiles from 12-40 km; difference between KASIMA and FTIR profiles from 12-40 km. Black means no data.

6.2.3   HCl

Similar to HF, HCl is produced in the stratosphere by photodissociation of CFCs. But in contrast to fluorine species, HCl might be released in the troposphere already by oxidation with the OH radical of CH_3Cl and CH_3CCl_3. HCl represents the terminal sink of chlorine and due to the global circulation scheme it is accumulated in the lower polar stratosphere, where it finally enters the troposphere and is eliminated by rainout. Chlorine chemistry is an important stratospheric ozone sink. In a pure gas phase chemistry already does it provide for the Cl radical for the chlorine catalytic cycle due to reaction 2.25 (the fluorine counterpart of 2.25 is endothermic), not to mention its importance to polar ozone depletion due to heterogeneous reactions on PSCs. Figure 6.15 shows the results for HCl. Its behavior is very similar to that of HF, i.e. the annual cycle which peaks in May is mainly due to enhanced upwelling in summer and the strong variability in winter, which might be caused by horizontal transport and short-term variations of the tropopause height. One difference should be mentioned, however. The amplitude of the annual cycle is smaller than in the case of HF (peak to peak for HF: 30%; HCl: 17%), which is probably due to the relative rate of release of chlorine and fluorine from the CFC reservoirs entering the stratosphere. Considering just $CFCl_3$ and CF_2Cl_2 (the major sources of chlorine and fluorine), $CFCl_3$ is photolyzed more rapidly and chlorine is initially released more quickly than fluorine [12]. This indicates that in summer the stratosphere above IZO is influenced by the tropical stratosphere, where most transport from the troposphere into the stratosphere occur. This difference to HF is also observed in the FTIR and KASIMA profiles: The ascent of VMR isolines in summer is much weaker for HCl than for HF. Although the modelled column amount shows the same annual cycle as the measurements, the amounts retrieved are constantly higher. A comparison of the profiles (lowest panel of 6.15) shows that these differences are due to quite higher KASIMA values below 28 km. It seems that these differences increse during the modelled period.

6.2.4   ClONO$_2$

ClONO$_2$ is an important reservoir gas for the stratospheric Cl radical. This is especially true for polar winter when no photodissicoation (reaction 2.23) occurs. The amounts of ClONO$_2$ and HCl or their ratio to HF $(([ClONO_2] + [HCl])/[HF])$ are often used to deduce chlorine activation, which would be present in case of very low values of $([ClONO_2] + [HCl])/[HF]$ (see reactions 2.39, 2.40, and 2.42). Figure 6.16 shows the stratospheric column amounts determined by the FTIR measurements. As pointed out in the previous chapter ClONO$_2$ is a week absorber and its determination is a difficult task, especially at the relatively low solar zenith angles present at the low-latitude site of Izaña. Nevertheless, an annual cycle peaking in
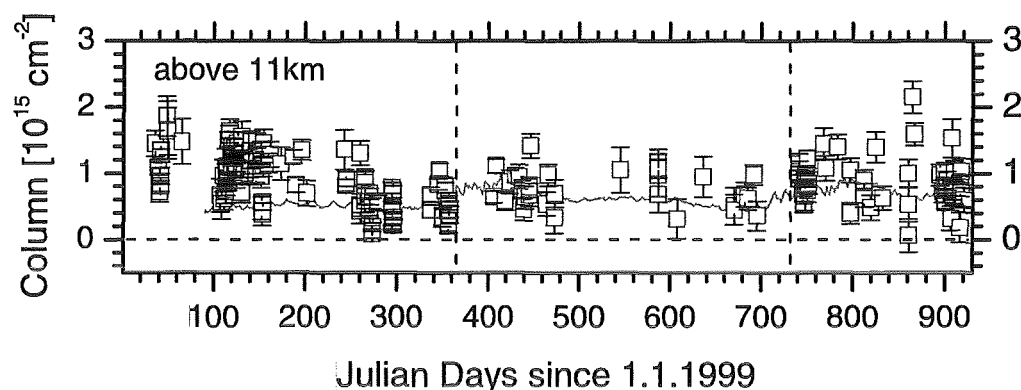
Fig. 6.16: $ClONO_2$ results from February 1999 to July 2001. Stratospheric column amounts of FTIR (open squares) and KASIMA (solid line).

late spring is observed. This is also expected and due to transport of airmasses rich in $ClONO_2$ from polar regions to lower latitudes after the breakdown of the polar vortex. It should be mentioned, however, that in analogy to HF and HCl, the amount of $ClONO_2$ may also decrease due to enhanced upward motion during summer. As an average over the whole measurement period KASIMA yields slightly lower stratospheric column amounts than the FTIR. However, due to the uncertainties involved in the $ClONO_2$ measurement as described in chapter 5 this difference lies still within the measurement uncertainties.

6.2.5 NO_2

Stratospheric NO_2 results from oxidation of NO by O_3. It is, in turn, subject to photolysis, as a result of which NO is regenerated:

$$NO_2 + h\nu \quad \rightarrow \quad NO + O \tag{6.1}$$

$$O + O_2 + M \quad \rightarrow \quad O_3 + M \tag{6.2}$$

$$NO + O_3 \quad \rightarrow \quad NO_2 + O_2 \tag{6.3}$$
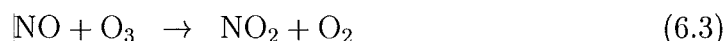
At altitudes below 40 km, these reactions mainly determine the ratio between NO_2 and NO, since these reactions are rather quick compared to other reactions affecting NO_2 and NO, i.e. during daytime a photostationary steady state exists (the reaction of NO with ClO is neglected due to the generally low concentrations of ClO at subtropical latitudes). Another important source of NO_2 is the photodissociation of N_2O_5 (reaction 2.31), which is responsible for its increase during daylight, e.g. in summertime the total column amount of NO_2 in the late afternoon exceeds the
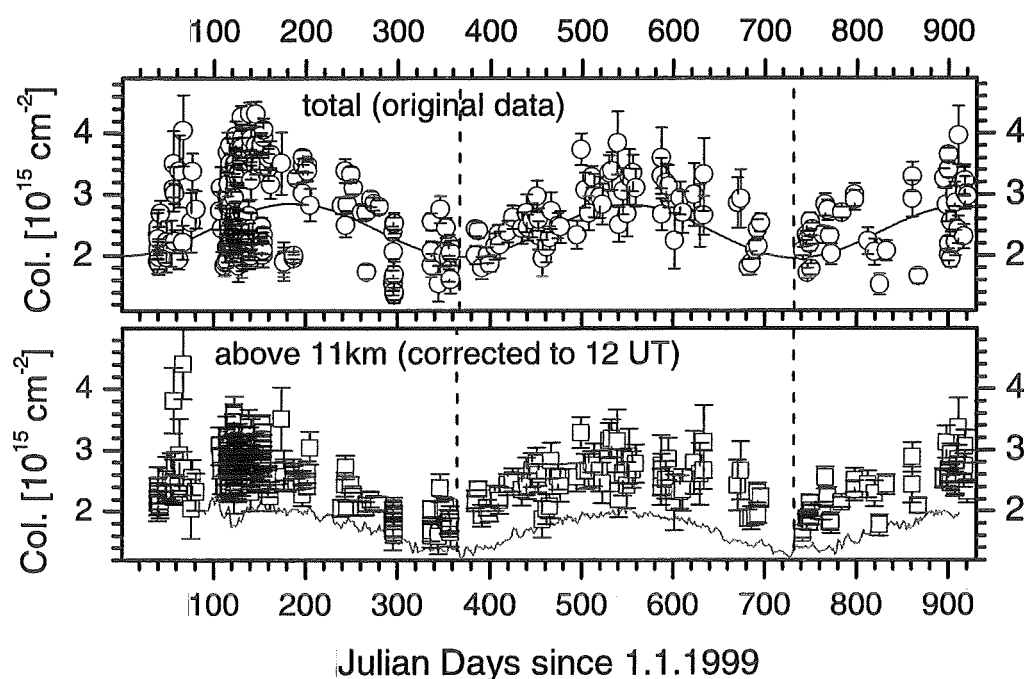
Fig. 6.17: NO$_2$ results from February 1999 to July 2001. Above: Total column amounts of FTIR measured at different times during day (open circles) and fitted sine function (solid line); Below: Stratospheric column amounts of FTIR corrected to 12 UT (open squares) and KASIMA for 12 UT (solid line).

morning value by about 40 %. At sunset, the photostationary state shifts towards NO$_2$ caused by diminished ultraviolet fluxes, and NO$_2$ increases rapidly. At sunrise, however, it decreases abruptly due to enhanced photodissociation to NO. During night, it is converted gradually to N$_2$O$_5$ (reactions 2.29 and 2.30). A variety of publications describing the diurnal variation of NO$_2$ is available (e.g. [65], [50]). The main sink of nitrogen oxides is transport into the troposphere at high latitudes.

The diurnal variation makes the presentations of the NO$_2$ time series more difficult, since the measurements were conducted at different times during the day. The upper part of Figure 6.17 demonstrates this problem. In May 1999, for instance, both measurements were conducted in the early morning and in late afternoon.

To separate the diurnal variation from day-to-day variability, we used total NO$_2$ column amounts measured by the DOAS spectrometer, at sunset, as a reference for the day-to-day variability. The left part of Figure 6.18 shows the dependence of the difference in percent between DOAS and FTIR on the time difference between the two measurements. The difference of the column amounts increases linearly with
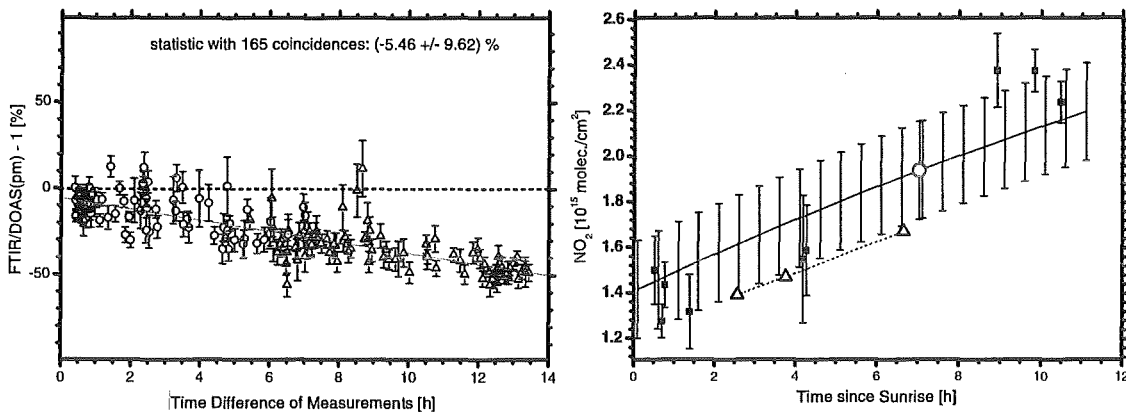
Fig. 6.18: Left part: Difference between FTIR NO_2 column amounts and DOAS NO_2, determined for the same day at different times during the day versus their respective time difference. DOAS column amounts are determined during sunset, FTIR column amounts in the morning (open circles) or in the afternoon (open squares). Right part: Comparison of measured diurnal variations (solid squares) and calculated variations (lines) for 21 - 23/10/99. The large open circles show the measured column amount, on which the calculations are based. For further explanation of the calculated variation, see text. Also shown is the diurnal variation modelled by KASIMA (open triangles).

increasing time difference of the measurements. This allows to relate the column amount measured at time t ($[NO_2]_t$) to its respective value at time t' ($[NO_2]_{t'}$):

$$[NO_2]_{t'} = [NO_2]_t + (t - t')\, a\, [NO_2]_{sunset} \qquad (6.4)$$

where a is the coefficient of change of $[NO_2]$ per time derived by the comparison with DOAS sunset values. It should be noted that the diurnal variation is eliminated by using FTIR results only. The DOAS values where solely used to determine the universal linearity coefficient a. As a first step, the FTIR sunset values ($[NO_2]_{sunset}$) have to be determined. This is done by applying 6.4 iteratively. In the first iteration, the measured value $[NO_2]_t$ is used for $[NO_2]_{sunset}$ on the right hand side of 6.4. Its result then serves as improved $[NO_2]_{sunset}$ for the following step. After several iterations, $[NO_2]_{sunset}$ remains unchanged. By means of these sunset values, NO_2 amounts for any time may be derived according to equation 6.4. The corrected FTIR values corresponding to $[NO_2]_{12\,UT}$ are shown in the lower part of Figure 6.17. The annual cycle with a maximum in summer and a minimum in winter is due to the chemical partitioning of the NO_x species (NO, NO_2, and HNO_3): In summer,
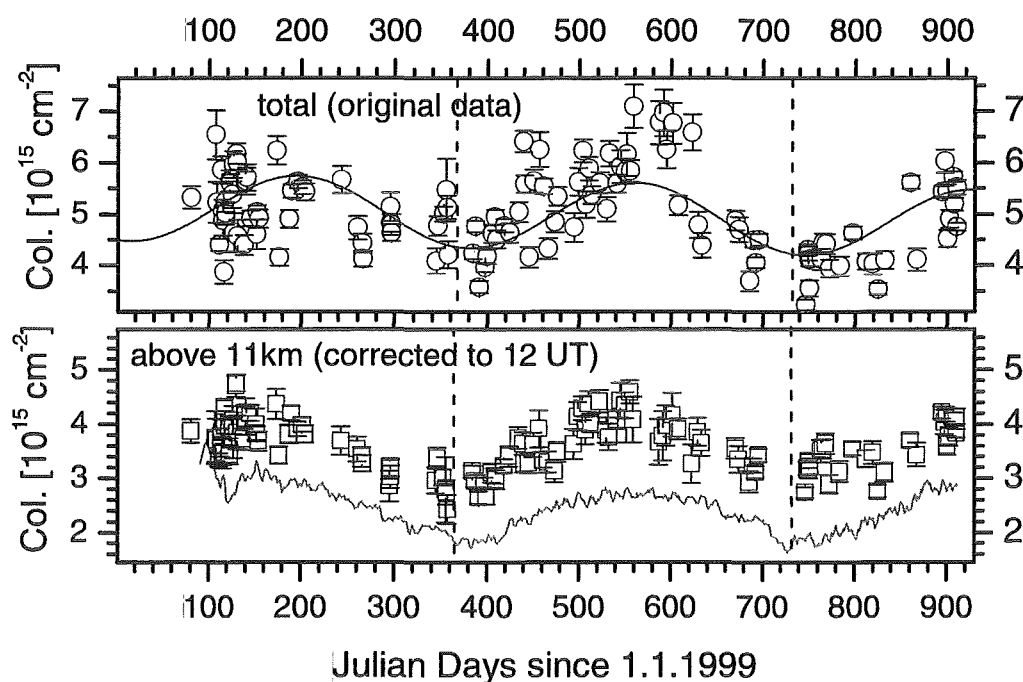
Fig. 6.19: NO results from February 1999 to July 2001. Above: Total column amounts of FTIR measured at different times during day (open circles) and fitted sine function (solid line); Below: Stratospheric column amounts of FTIR corrected to 12 UT (open squares) and KASIMA for 12 UT (solid line).

relatively more NO_x exists in the form of NO and NO_2 than in winter. KASIMA shows the same annual cycle, but also constantly lower amounts.

The right part of Figure 6.18 demonstrates, as an example, a comparison of the diurnal variation measured or calculated as described above and KASIMA data. They are all in good agreement. The deviation of the FTIR measurement points from the linear regression line in Figure 6.18 also serves to compare DOAS and FTIR values. As a mean of the 165 coincidences, the values differ by 5.46 % with the DOAS column amounts being higher. However this difference lies within the standard deviation from the mean and therefore, it is not significant.

6.2.6   NO

Oxidation of N_2O by the reaction with $O(^1D)$ is the most important source of stratospheric NO. The $O(^1D)$ oxygen atoms arise primarily from the photodissociation of O_3 at 25 to 35 km altitude in the tropics. NO is also produced in the thermo- and

mesosphere from ionized air molecules. The ionization is caused by the solar wind
and the shortwave electromagnetic radiation . The photostationary steady state of
NO and NO_2 already is described above. NO also shows strong diurnal variations.
Due to this diurnal variations and the uncertainties involved in the correction of the
solar line as discussed in chapter 5, we present column amounts only. The upper
part of Figure 6.19 depicts the retrieved NO column amounts with an uncorrected
diurnal variation.
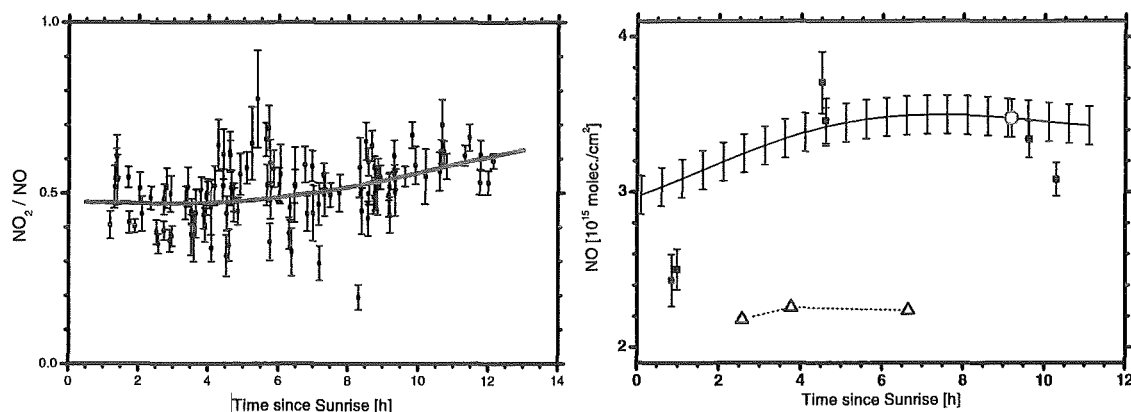
Fig. 6.20: Left part: NO_2/NO ratio versus time since sunrise and function $F(h)$
(thick line). Right part: Comparison of measured diurnal variations
(solid squares) and calculated variations (lines) for 21 - 23/10/99. The
large open circles show the measured column amount, on which the cal-
culations are based. For further explanation of the calculated variation,
see text. Also shown are KASIMA data (open triangles).

Since NO is not measured by other instruments at IZO, the diurnal variability
cannot be separated from the day-to-day variability in similarity to NO_2. It was
therefore attempted to correct the NO column amounts by means of the photosta-
tionary steady state between NO and NO_2. The left part of Figure 6.20 shows the
ratio between NO and NO_2 versus time since sunrise. For an accurate calculation of
the ratio, the respective NO_2 column amounts were determined for the time of the
NO measurement according to equation 6.4. The absolute value of the $[NO_2]/[NO]$
ratio and its slight increase during daytime, as seen in Figure 6.20, is consistent with
other measurements (e.g. [33]). Only measurements for solar zenith angles below
75° are shown in Figure 6.20. They were used to derive a function $F(h)$ which de-
scribes the average $[NO_2]/[NO]$ ratio versus time since sunrise for all measurements
made from March 1999 to July 2001. This selection was made since rapid changes in
the photolysis frequency of NO_2 at high solar zenith angles may disturb the steady
state and change the $[NO_2]/[NO]$ ratio rapidly. The function $F(h)$ allows to relate

the variation of NO to the known variation of NO_2:

$$\left|\Delta[\text{NO}] = \frac{1}{F(h)} \, \Delta[\text{NO}_2] - \frac{[\text{NO}_2]}{F(h)^2} \, \Delta F(h) \right. \tag{6.5}$$

The lower part of Figure 6.19 shows the stratospheric NO column amounts (above 11km) corrected to 12 UT according to equation 6.5. Similar to NO_2, the observed annual cycle peaks in summer and is due to the partitioning of nitrogen species. KASIMA derives a similar cycle, but with considerably lower absolute values compared to the measurements.

This correction according to equation 6.5 eliminates part of the diurnal variations, as seen in Figure 6.19. However, the rather idealized assumption of a universal diurnal evolution of the $[\text{NO}_2]/[\text{NO}]$ ratio for all days between March 1999 and July 2001 (function $F(h)$) makes this correction less accurate than in the case of NO_2. This can also be seen in the right part of Figure 6.20, where the calculated diurnal variation is compared with the measured ones for 21 - 23/10/99. The rough diurnal evolution of NO, i.e. relatively rapid increase in the morning and slow decrease in the afternoon, is described by the simplified correction, but the actual extent of the increase and decrease is underestimated. The KASIMA calculations depicted on the right of Figure 6.20 show the same diurnal variation, but their absolute values are much lower than the measured ones. In our simple correction, a change in the $[\text{NO}_2]/[\text{NO}]$ ratio due to the time elapsed since sunrise was considered only. For a better correction, further parameters have to be taken into account. These are mainly the O_3 concentration and temperature profiles. Hence, a reasonable correction of the NO amounts can only be made by means of a photochemical model.

6.2.7 HNO_3

HNO_3 arises from the interaction of NO_2 with OH radicals (see reaction 2.26). At altitudes below 25 km, the time constant for the photodissociation of HNO_3 (reaction 2.27) is high. Hence, HNO_3 is relatively stable and provides for the major reservoir of NO_x (i.e. NO + NO_2) in the troposphere and lower stratosphere. As O_3, HF, HCl, and the nitrogen oxides, it undergoes poleward transport. It is accumulated in the lower polar stratosphere and finally mixed into the troposphere. Heterogeneous reactions of N_2O_5 or $ClONO_2$ on PSCs to HNO_3 (reaction 2.35 - 2.38) and subsequent sedimentation of these particles may cause denoxification in polar winters, which enforces ozone destruction (see chapter 2). Figure 6.21 shows time series of the column amounts and profiles of HNO_3. Similar to all stratospheric gases, the annual cycle peaks in late spring and shows minimum values in October. The stratospheric column amounts exhibits less day to day variability, which suggests that tropospheric HNO_3 occasionally contributes significantly to the total

column amount. KASIMA yields continuously lower column amounts than FTIR. This, together with the observations made for NO_2 and NO, means that more reactive nitrogen is measured than modelled, which was already observed by comparison with other measurements (e.g. [27]). Similar to the other gases, the HNO_3 FTIR profiles also indicate enhanced upwelling in summer. The VMR maximum is most pronounced in winter, due to a less effective photodissociation of HNO_3 (reaction 2.27). For the same reasons lower amounts of NO_2 and NO are detected during this period. The KASIMA profiles confirm this general behavior, but their VMR maximum is located at lower values compared to the FTIR results.
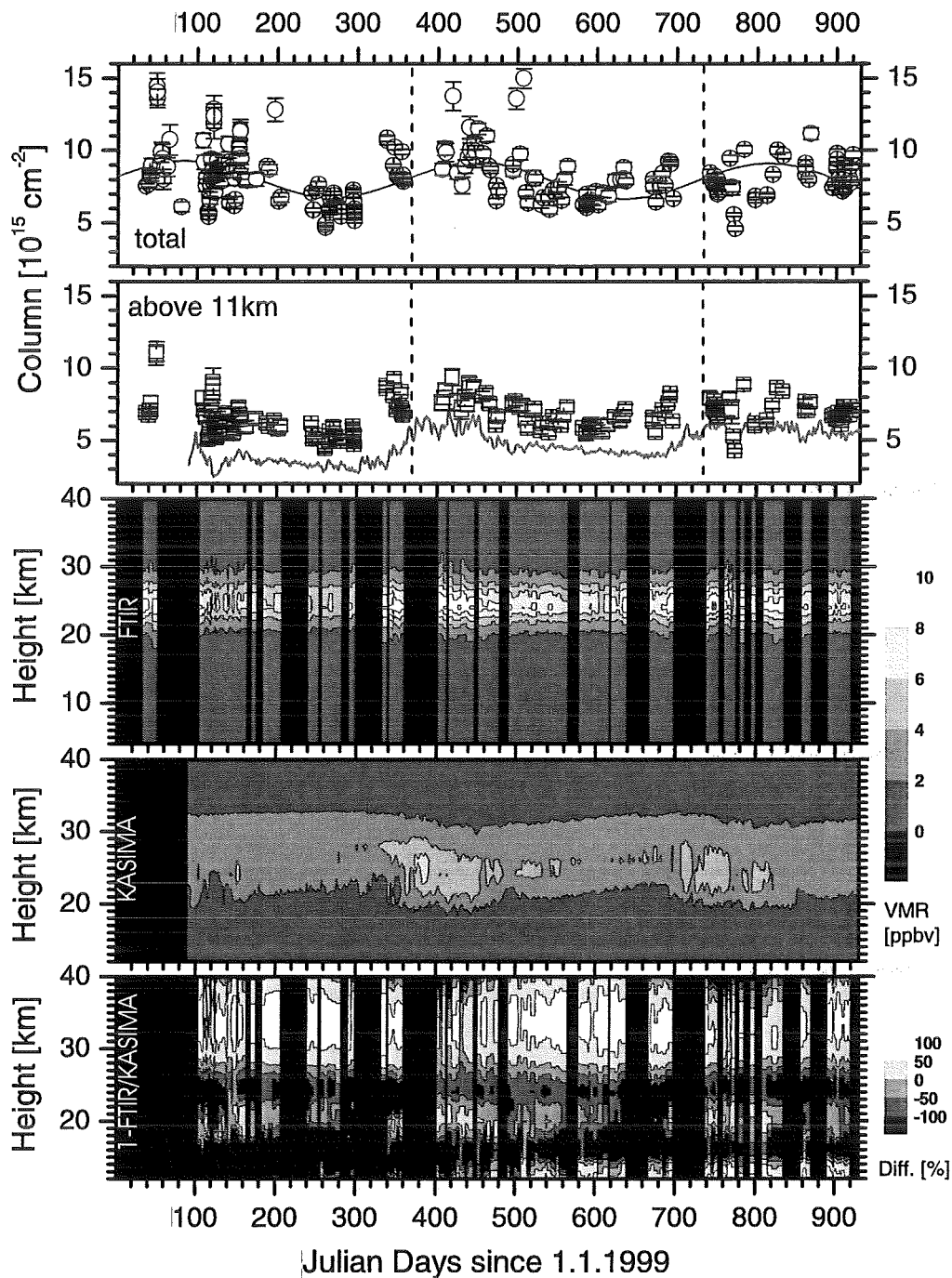
Fig. 6.21: HNO$_3$ results from February 1999 to July 2001. From above to below: Total column amounts of FTIR (open circles) and fitted sine function (solid line); stratospheric column amounts of FTIR (open squares) and KASIMA (solid line); FTIR profiles from 4-40 km; KASIMA profiles from 12-40 km; difference between KASIMA and FTIR profiles from 12-40 km. Black means no data.

6.3 Summary of the FTIR-KASIMA Comparison

Generally, the KASIMA data show annual evolutions similar to those of the FTIR data with enhanced upwelling in summer and higher variability in winter. However, some significant differences exist. The observed differences and agreements shall be summarized and discussed below.

While the stratospheric column amounts of N_2O and CH_4 agree well with the FTIR data, differences are found between their respective profiles: In the case of N_2O, the KASIMA VMR values are constantly lower than the FTIR VMR values below 25 km. Above 25 km, the opposite is observed, i.e. KASIMA values are higher than FTIR values. This is in contrary to CH_4, where higher KASIMA values are calculated below 25 km and lower values above 25 km. Similar observations have already been made for comparisons of KASIMA and FTIR profiles of high latitudes ([64]). A reason might be the lower height resolution of the FTIR compared to KASIMA.

Stratospheric O_3 column amounts of KASIMA and FTIR are in good agreement. Only, during the first months of the modelled period, are greater deviations found which may be attributed to the initialization of the model. The profiles demonstrate that these differences can be attributed to lower KASIMA VMR values between 18 and 25 km as compared to the FTIR values. Although these differences decrease in the first months of the modelled period, a certain underestimation of the VMR values between 15 and 28 km remains during the whole period. It seems, as if KASIMA models stronger upwelling than detected by the FTIR. On the other hand, the KASIMA values exceed the FTIR values between 28 and 38 km, where the VMR maximum is located and O_3 production takes place in the tropics. The data from the O_3 sondes confirm these observation. All these differences indicate that the stratosphere modelled by KASIMA is stronger tropically influenced than the one detected by the FTIR.

For HF the stratospheric column amounts are in good agreement. Greater differences are only observed in the VMR values between 15 and 22 km, which are lower for KASIMA than for the FTIR. This can also be explained by a modelled stratosphere which is more influenced by the tropics than suggested by the measurements.

Modelled and measured HCl column amounts exhibit large differences. Stratospheric column amounts of KASIMA are approximately 35 % larger than the corresponding FTIR column amounts. Comparison of the profiles reveals that these differences are due to higher KASIMA VMR values below 28 km as compared to the FTIR VMR values. These differences may be attributed to the initialization of the model. In contrast to O_3, however, the modelled HCl does not tend from the initialization profile applied towards the profiles actually present. This difference to O_3 can be explained by the lifetime of HCl, which is about 3 orders of magnitude larger than the one of O_3 in the lower stratosphere. A modelled stratosphere with

strong tropical influences would also explain the KASIMA HCl results: A stronger tropically influenced stratosphere supplies relatively more HCl, since the tropics are the source region of stratospheric HCl. This overestimation of HCl supply is indicated by the constantly increasing differences between the KASIMA and FTIR data during the modelled period. This interpretation is supported by the comparison of the stratospheric column amounts of $ClONO_2$. Although they still agree within the limits of the measurement uncertainty, on the average, the modelled $ClONO_2$ is lower than the measured one, which is consistent with the younger stratospheric air due to an overestimated tropical influence in the model.

KASIMA stratospheric column amounts of HNO_3, NO_2, and NO are smaller than those retrieved by the FTIR. This has already been demonstrated by comparisons between KASIMA and FTIR data for high latitudes (e.g. [27]). For NO and NO_2 this is due to the production of NO in the thermo- and mesosphere by the ionization of air caused by the solar wind and shortwave radiation, which is not considered in the model. For HNO_3, however, it may additionally be due to a boundary effect of the model, since relatively high HNO_3 amounts in the upper troposphere, i.e. below the model's boundary, are not considered and, hence, the upper troposphere as a source region for stratospheric HNO_3 is underestimated. This is obvious from the comparisons of the HNO_3 profiles, which clearly show lower KASIMA VMR values below 18 km than FTIR values. The HNO_3 VMR maximum around 25 km is less pronounced for KASIMA than for the FTIR, which may be also due to a modelled stratosphere with strong tropical influences.

6.4   Comparison with POLARSTERN Data

In this section our results are compared to column amounts derived by measurements also conducted with a Bruker IFS 120M FTIR spectrometer. This instrument was installed onboard the POLARSTERN research vessel. The route of the POLARSTERN at the end of December 1999 is shown in Figure 6.22. From 21 - 23/12/99, the ship was located close to the Izaña Observatory and during these days both instruments detected similar airmasses.

All POLARSTERN spectra were analyzed by using the nonlinear least square software GFIT ([73]). Also a measured ILS was used for the retrieval. The column amounts were derived by scaling a start profile only. For further experimental details, see [47] and references herein.

Since the POLARSTERN data set merely consisted of total column amount data and since the two instruments were located at different altitudes (sea level vs. 2400m a.s.l.), only a comparison of stratospheric constituents is meaningful. Figure 6.23 shows the column amounts of O_3, NO_2, HF, HCl, and HNO_3, detected at Izaña (FTIR, DOAS (O_3, NO_2), Brewer(O_3)) and from the POLARSTERN. Both data
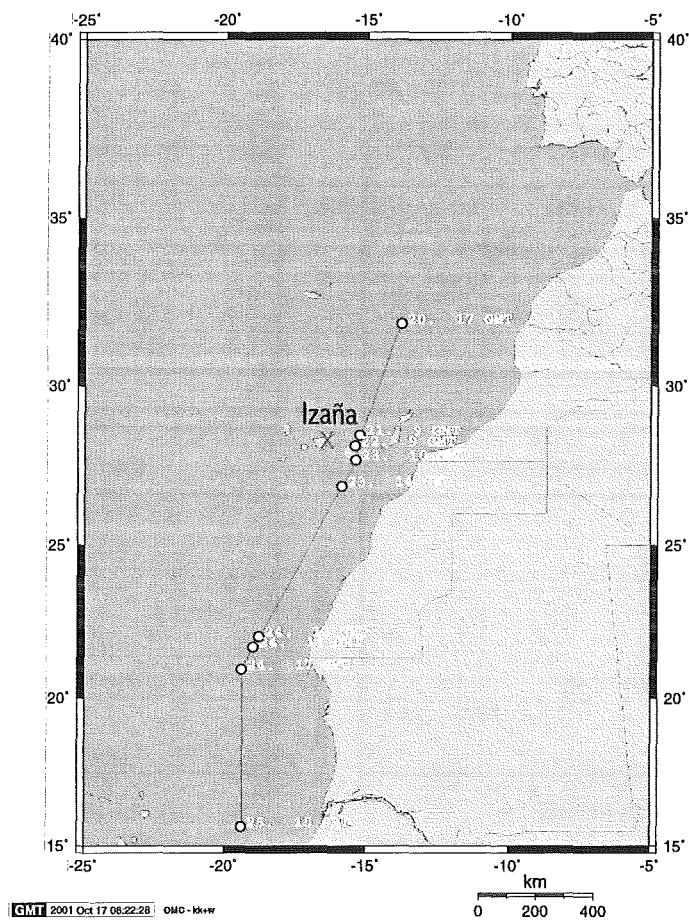
Fig. 6.22: Route of the research vessel POLARSTERN while passing the Canary Islands at the end of December 1999.

sets are generally in good agreement, in particular if one considers that two different evaluation procedures have been applied. The ZCA of HCl and HNO_3 are generally smaller at IZO. Since both gases are also present in the troposphere, this may be explained by the altitude difference of the instruments' locations.
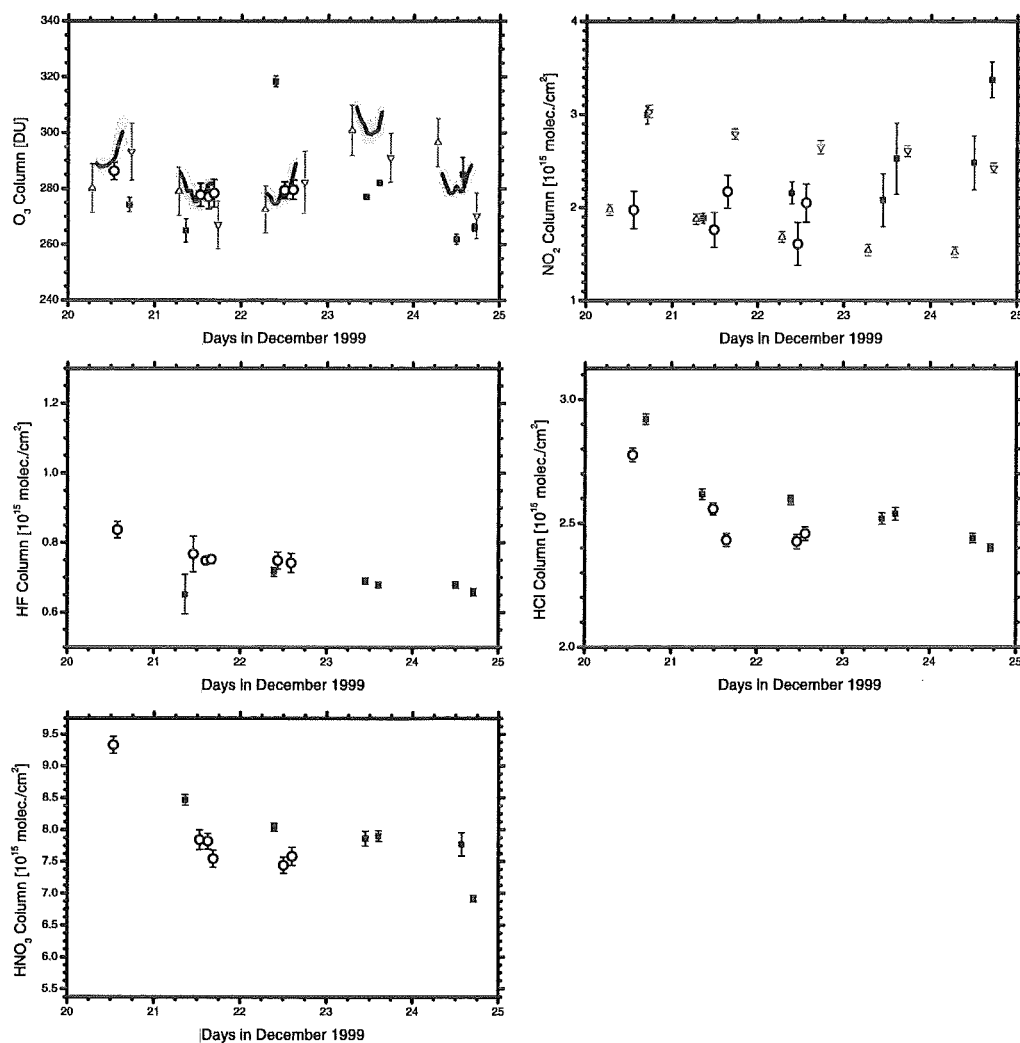
Fig. 6.23: Comparison of column amounts of O_3, NO_2, HF, HCl, and HNO_3 as detected at Izaña and from the POLARSTERN. Filled squares represent the POLARSTERN values, open circles show the Izaña data. For O_3 and NO_2, up and down triangles denote DOAS data for sunrise and sunset measurements. The O_3 plot also depicts Brewer results (solid lines with the grey shaded area indicating their uncertainty).

Chapter 7

Interpretation of Measurements

Some explanations of the general evolution of the detected trace components is already given in the previous chapter. Additionally, the general differences between model and measurements are already discussed there. This chapter intensifies these interpretational efforts by a more detailed consideration of both the evolution of measured components and their discrepancies to modelled data.

7.1 Trace Gas Ratios

As already mentioned, the distribution of trace gases is subject to both transport and chemical processes. Generally, it is difficult to separate these two processes, since they are coupled. However, some removal of the transport-related variations may be achieved by calculating the ratio between two trace gases with similar vertical and horizontal distributions. Subsequently, a classification into stratospheric and tropospheric components may be made. All members of one of the classes are assumed to have similar vertical and horizontal distribution patterns.

7.1.1 Stratospheric Components

We consider HF, HCl, O_3, and HNO_3 with HF being used as reference for transport processes, i.e. ratios of [HCl]/[HF], [O_3]/[HF], and [HNO_3]/[HF] are presented. Figure 7.1 shows the ratio between the column amounts of HCl and HF. Comparison with Figure 6.14 reveals that most of the short-term variations which are assumed to result from transport processes are removed. Figure 7.1 shows an annual cycle peaking in October/November and a minimum in May. The difference between the typical ratios for May and November is roughly 20%.

To estimate the influence of vertical motions on the [HCl]/[HF] ratio, this ratio was calculated for typical profiles, and these profiles were shifted vertically in steps
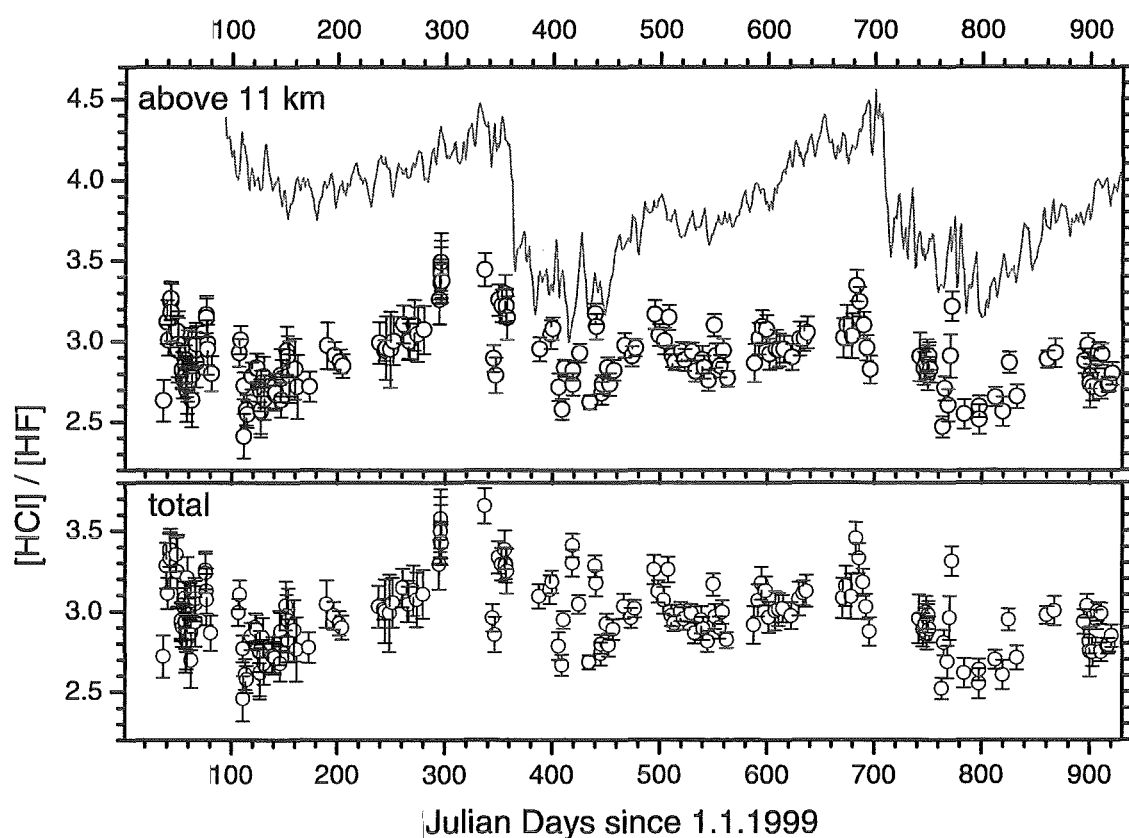
Fig. 7.1: Evolution of the HCl/HF ratio. Upper part: Stratospheric ratios of FTIR (open circles) and KASIMA (solid line). Lower part: Ratios of total FTIR column amounts.

of 2 km up to 6 km. The highest change of the [HCl]/[HF] ratio was achieved when profiles with low tropopause were shifted. But even in this case and for a shift of 6 km, the change in the ratio was less than 3%. It is difficult to make a similar estimation for the influence of horizontal transport, but the close confinement of the ratio values also in the winter period when most of the horizontal transport occurs suggests that it is far smaller than 20%, with one exception: If airmasses originating from the center of the tropics are present over IZO, the [HCl]/[HF] ratio rises abruptly. Such an event was detected on 10/2/01 (day 773).

Hence, transport processes clearly cannot explain the annual cycle found with variations of 20%. In the previous chapter, it is already suggested that this is due to the relatively slower rate of release of fluorine from its precursors than of chlorine in air that recently entered the stratosphere (see also [12]). An increase of the [HCl]/[HF] ratio would therefore correspond to a rejuvenation of stratospheric
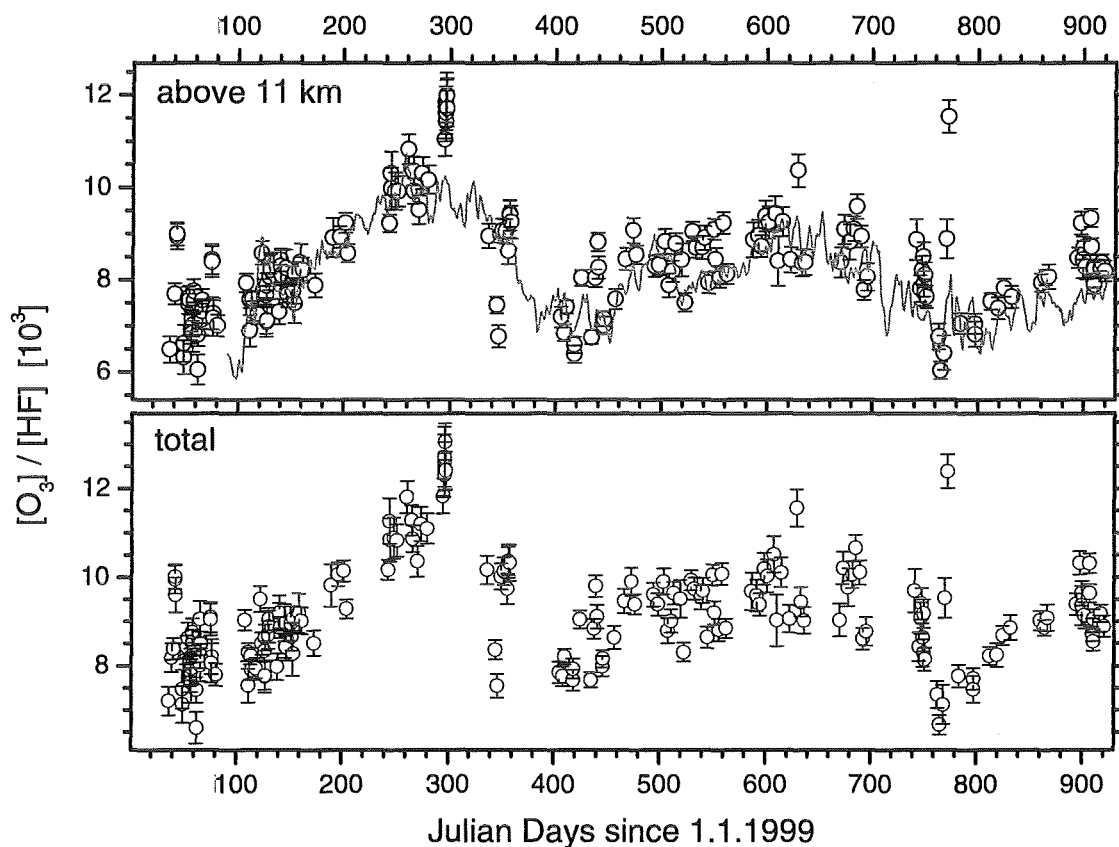
Fig. 7.2: Evolution of the O_3/HF ratio. Upper part: Stratospheric ratios of FTIR (open circles) and KASIMA (solid line). Lower part: Ratios of total FTIR column amounts.

air. Since nearly all transport from the troposphere into the stratosphere occurs in the tropics, it is obvious that from May to November the stratosphere above IZO is tropically influenced. As pointed out in chapter 2, a transport barrier exists between the tropical and extra-tropical stratosphere. Therefore, IZO must be situated on the tropical side of this barrier or the barrier must be weaker in this period. The latter is not verified by various calculation ([75], [11]). Calculations indicate the opposite, i.e. enhanced transport from out of tropics into the mid-latitudes from late fall to spring due to enhanced activity and breaking of planetary waves and a stronger barrier in summertime. A study of the tropical stratospheric reservoir in [21] based on observations of volcanic aerosols suggests, however, that the edges of the tropical reservoir are well defined and situated around 20°N from November to March and rather broad from May to October reaching up to 32°N. This may indicate that in the summertime the stratosphere above IZO belongs to the tropical stratospheric
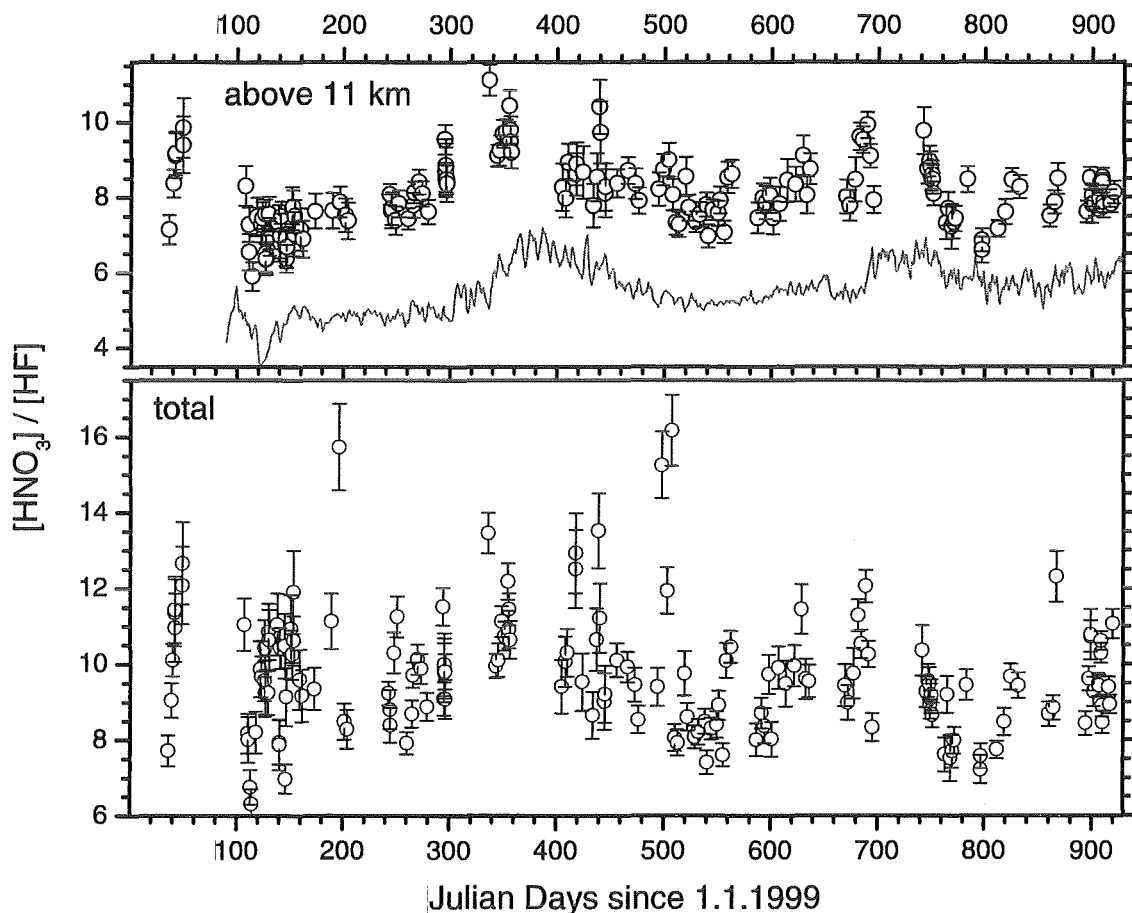
Fig. 7.3: Evolution of the HNO3/HF ratio. Upper part: Stratospheric ratios of FTIR (open circles) and KASIMA (solid line). Lower part: Ratios of total FTIR column amounts.

reservoir rather than to the extra-tropical stratosphere. The [HCl]/[HF] ratio determined by KASIMA exceeds the measured one by approximately 30%. It also shows an abrupt decrease in the beginning of winter, which is not detected by the FTIR.

In Figure 7.2 the [O3]/[HF] ratio is shown. Relating O3 to HF removes several short-term variations as is demonstrated by a comparison of 7.2 and 6.8. The maximum of this ratio in October has the same reasons as in the case of the [HCl]/[HF] ratio. In spring 2000, the increase of the ratio ceases compared to the other years. This may be due to enhanced chemical ozone depletion inside the polar vortex and its subsequent transport to lower latitudes in this year. KASIMA and FTIR generally show a good agreement in terms of the [O3]/[HF] ratio, but the model does not reveal the strong short-term variation present in the FTIR data (e.g. October 1999
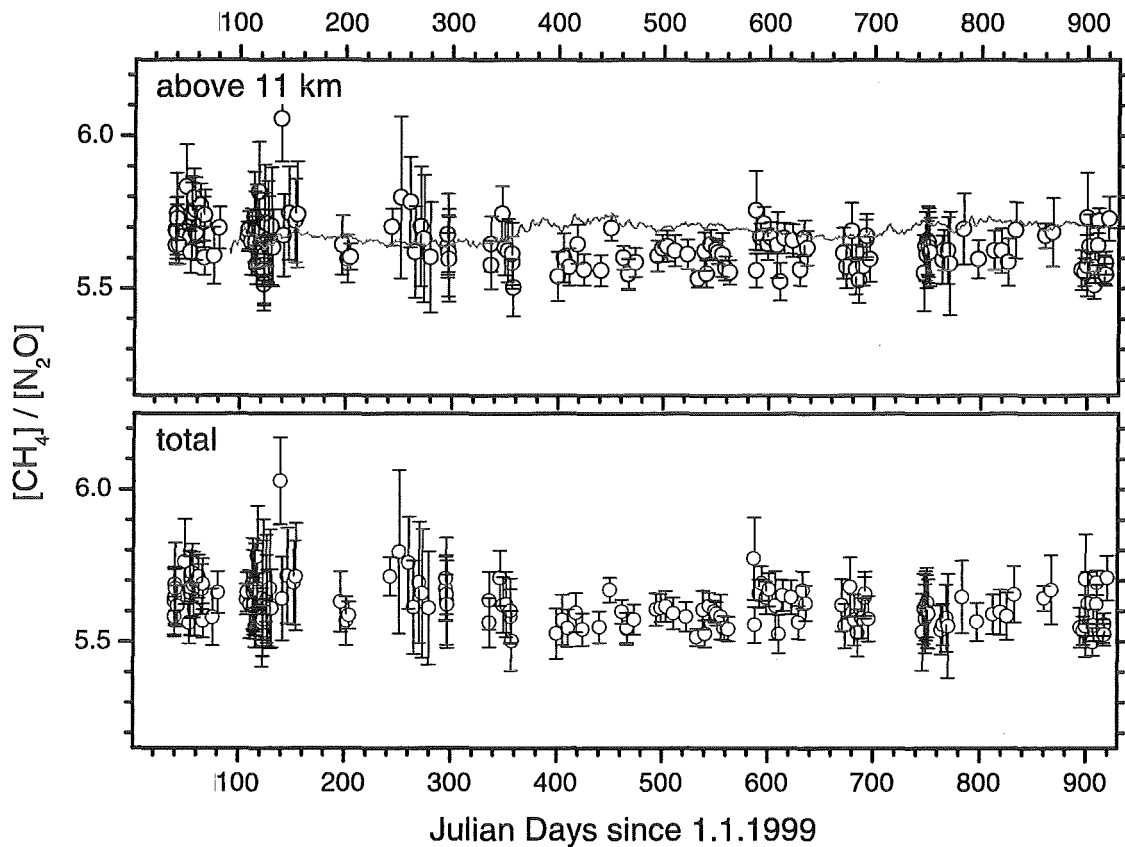
Fig. 7.4: Evolution of the CH_4/N_2O ratio. Upper part: Stratospheric ratios of
FTIR (open circles) and KASIMA (solid line). Lower part: Ratios of
total FTIR column amounts.

or February 2001).

Figure 7.3 depicts the $[HNO_3]/[HF]$ ratio. The ratio between the total column
amounts is influenced by tropospheric HNO_3 and shows a less defined annual cycle
than the ratio formed by stratospheric column amounts (above 11 km). A similar
cycle as for $[HCl]/[HF]$ is found, but it is shifted by about two months, i.e. it peaks
in December. This is mainly due to varying nitrogen partitioning in summer and
winter. In winter, a relatively large fraction of active nitrogen $(NO_2 + NO + HNO_3)$
exists in form of HNO_3 as compared to summer. This is caused by lower solar fluxes
and, thus, a decreasing efficiency of reaction 2.28. KASIMA and FTIR show the
same long-term evolution, but their absolute values disagree. This is due to the
already described inconsistencies between modelled and measured HNO_3.
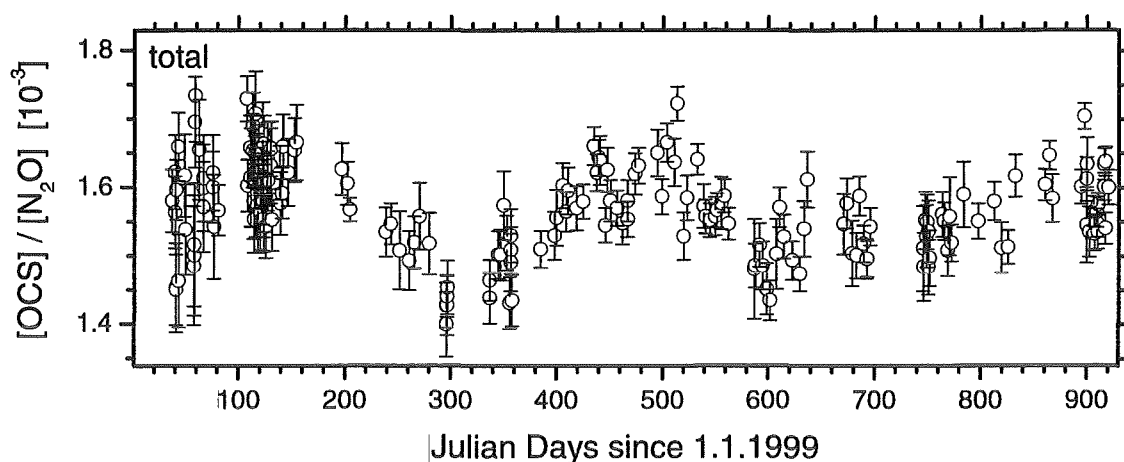
Fig. 7.5: Evolution of the OCS/N_2O ratio.

7.1.2 Tropospheric Components

As for stratospheric components the evolution of ratios between tropospheric components shall be presented below. As a reference for separating transport processes, N_2O is used. Figure 7.4 depicts the ratio of $[CH_4]/[N_2O]$ from February 1999 to July 2001. The short-term variation seen in Figures 6.4 and 6.5 is nearly completely removed, which strongly suggests that they are solely due to transport processes or instrumental errors, like mismatches of the sun tracker as described in chapter 5. An investigation of further tropospheric trace gases by relating them to N_2O therefore seems to be useful.

The $[OCS]/[N_2O]$ ratio is shown Figure 7.5. As before, the cycle is better defined compared to Figure 6.6 (15% difference between maximum and minimum in Figure 7.5 compared to 9% in Figure 6.6).

Finally, HCN was related to N_2O, which is depicted in Figure 7.6. Comparison with Figure 6.7 illustrates once again that short-term variations assumed to result from transport processes or instrumental uncertainties are removed. The annual cycle gets much smoother and becomes even better visible.

7.2 Typical Profiles for Airmasses from High and Low Latitudes

As can be seen in the annual cycles presented in chapter 6, both the lowest and highest amounts of the trace gases are detected during the winter period. These strong variations from November to April are mainly attributed to the enhanced
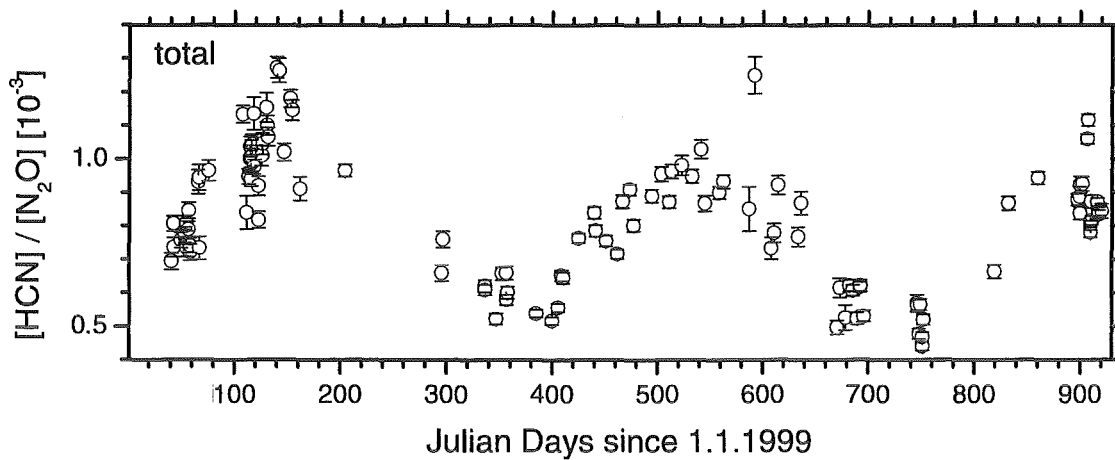
Fig. 7.6: Evolution of the HCN/N_2O ratio.

wave activity and, hence, enforced transport during the winter season. In this section we will have a closer look on the trace gases detected under different stratospheric conditions in order to demonstrate that these variations depend on the history of the detected airmass. This investigation is done in the form of a case study. Two extreme cases are distinguished, which are a stratosphere above IZO influenced by high latitudes and by the tropics. To decide on the stratospheric situation, the parameters described in chapter 4, i.e. the backward trajectories and the potential vorticity values, are applied.

7.2.1   High Latitude Airmass

A great difficulty in interpreting the trace gas amounts is that the atmospheric situation differs widely depending on the altitude region considered. In very rare cases, all stratospheric levels show a similar transport pattern. This is especially true in winter, when the enhanced wave activity generally disturbs a purely geostrophic flow pattern. Figures 7.7 and 7.8 confirm this problem. They present two situations for a stratosphere which is partly influenced by high latitudinal airmasses. The left panel shows the backward trajectories for the 400, 450 , 550, and 675 K levels, whereas the right part presents the respective EPV values. Deviations from a long-term mean EPV value are plotted. This value was calculated by adjacent averaging considering the 50 neighboring days. This was done to remove long-term variations. Additionally it allows to plot the EPV of all levels in the same graphics. In both cases presented in Figures 7.7 and 7.8, the situations of the different levels vary widely, i.e. besides levels that are influenced by high latitudes, there are also altitude regions that are influenced by low latitudes. On 18/2/99 for example, the 450 and

550 K levels, which correspond to an altitude region between 18 and 24 km, are clearly influenced by high latitudes, whereas the backward trajectory for 675 K (25.5-27km) shows airmasses originating from tropical regions. The EPV diagram suggests that especially the 400K level is affected by high latitudes, which is documented by an unusually high EPV value for this season. On 9/2/00, the higher levels are influenced by high latitudes as demonstrated by the backward trajectories for the 550 and 675 K levels (corresponding to an altitude of 22-27 km) and the EPV plot which shows unusually high values in particular for the 675 K level. On the other hand, the 400 K level (appr. 16 km altitude) is rather influenced by tropical airmasses. Unfortunately, no clearer, i.e. more defined, high latitudinal impact on the stratosphere above IZO prevailed on the measurement days in the years 1999-2001. Hence, the two situations described above are used as typical stratospheric conditions influenced by high latitudes. Figure 7.9 shows FTIR profiles for HF, HCl, O_3, HNO_3, N_2O, and CH_4 for these days, compared with the respective mean FTIR profile calculated from all FTIR profiles detected from January to March from 1999 to 2001. On 18/2/99, when the lower stratosphere was influenced by high latitudes, the respective profiles differed significantly in the altitude region around 10-25 km. The stratospheric components HF, HCl, and HNO_3 show increased VMR in exactly that altitude region where the backward trajectories and the EPV values indicate airmasses from high latitudes. Although less pronounced, the profile of O_3 shows the same behavior. In contrast to this, the tropospheric components N_2O and CH_4 are less abundant in this height region compared to their respective mean values. On 9/2/00, when the middle stratosphere was influenced by high latitudes, the deviations from the mean profiles were weaker. Some differences however, are also visible above 24 km: All stratospheric components, i.e. HF, HCl, O_3, and HNO_3, show a higher VMR in the altitude regions where backward trajectories and EPV values suggest high-latitude airmasses. A similar decrease of the tropospheric gases N_2O and CH_4 as on 18/2/99, however, is difficult to observe on 9/2/00. This may be due to the low height resolution above 22 km for these components.

In both cases, the altitude regions influenced by high-latitude airmasses showed an increased VMR for stratospheric components and a decreased VMR for tropospheric components. These observations are consistent with the Brewer-Dobson circulation described in chapter 2, since the enhanced downwelling at high latitudes explains both the higher VMR of stratospheric components and the lower VMR of tropospheric components (see also Figures 2.5 and 2.6 for the typical latitudinal-height distribution of HF and CH_4).
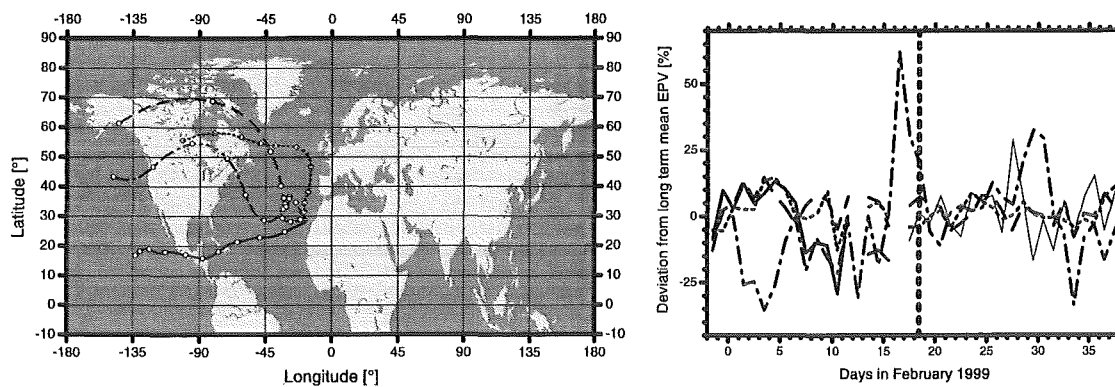
Fig. 7.7: Stratospheric conditions for 18/2/99. The left panel shows the 10-days backward trajectories, the right panel depicts EPV values. The levels of 675 K (solid line), 550 K (dashed line), 450 K (dotted line),and 400 K (dashed-dotted line) are considered.
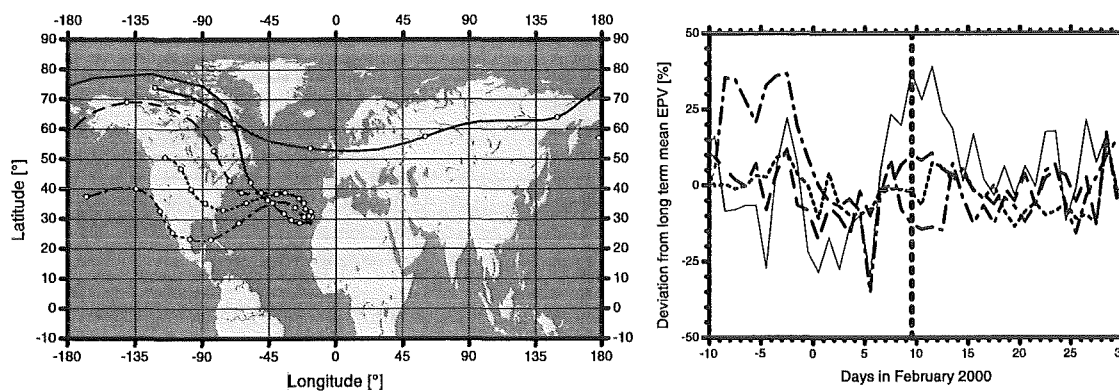
Fig. 7.8: Same as Figure 7.7, but for 9/2/00.
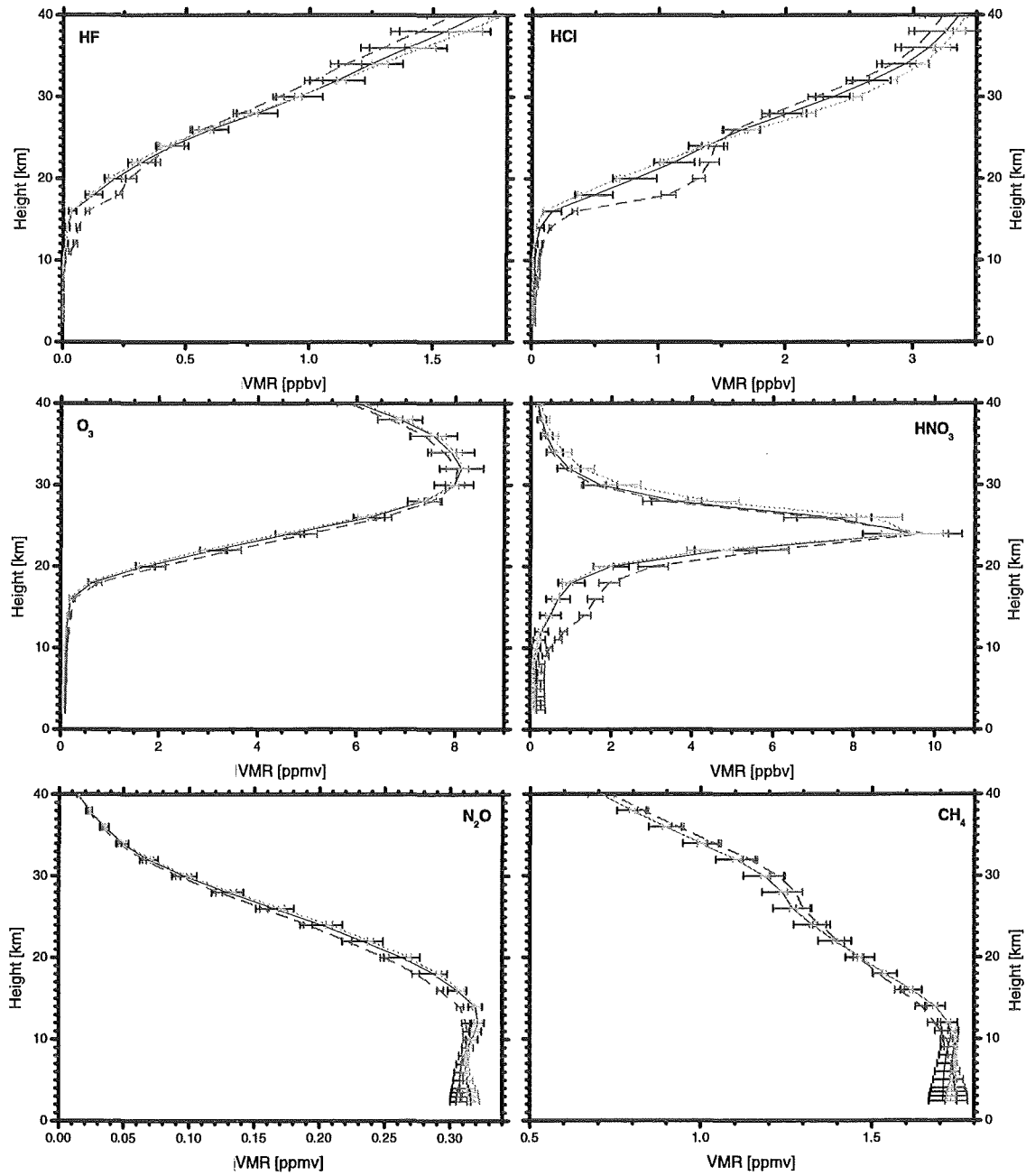
Fig. 7.9: FTIR profiles for airmasses from high latitudes. Shown are climatological profiles of FTIR measurements (solid lines), profiles for 18/2/99 (dashed lines), and profiles for 9/2/00 (dotted lines) of HF, HCl, O_3, HNO_3, N_2O, and CH_4.
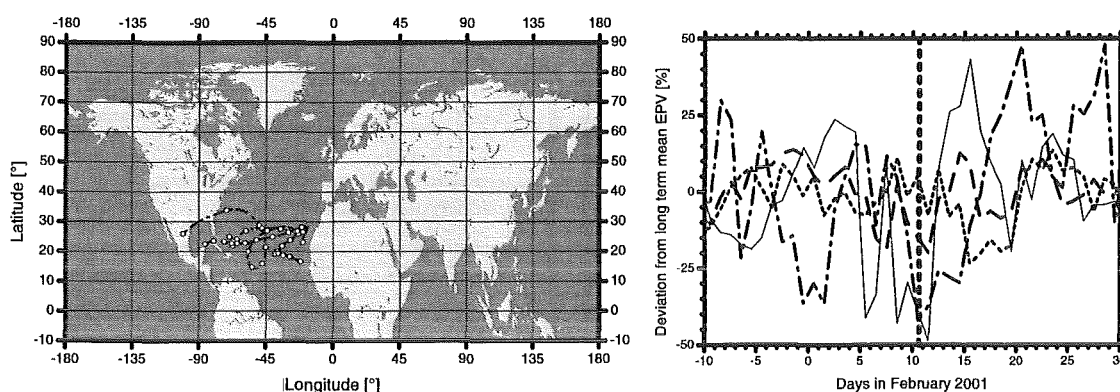
Fig. 7.10: Stratospheric conditions for 10/2/01. The same parameters on same levels as in Figure 7.7 are represented.

7.2.2 Low Latitude Airmass

Figure 7.10 depicts the backward trajectories and EPV values for a stratosphere influenced by tropical airmasses. The left shows that on 10/2/01, all levels above 400 K (above 16 km) are more or less tropically influenced, which is also suggested by the relatively low EPV values on this day. Additionally, the tropopause is situated at around 16 km on this day (see Figure 4.3). It is therefore self-evident that the whole atmosphere is influenced by the tropics. In Figure 7.11 profiles retrieved on 10/2/01 and the same mean FTIR profiles as in Figure 7.9 are plotted. Significant changes as compared to the typical situation are observed: All stratospheric (HF, HCl, O_3, HNO_3) and tropospheric gases (N_2O, CH4) show upward shifted profiles, which is due to the enhanced upwelling in the tropics according to the Brewer-Dobson circulation. Additionally, O_3 demonstrates increased VMR values around its maximum, which is the O_3 source region according to the Chapman cycle (equations 2.14 - 2.17). The maximum of HNO_3 also changes significantly. It is reduced by approximately 40%. Both enhanced O_3 production and decreased HNO_3 are typical for the tropics and caused by elevated solar fluxes.
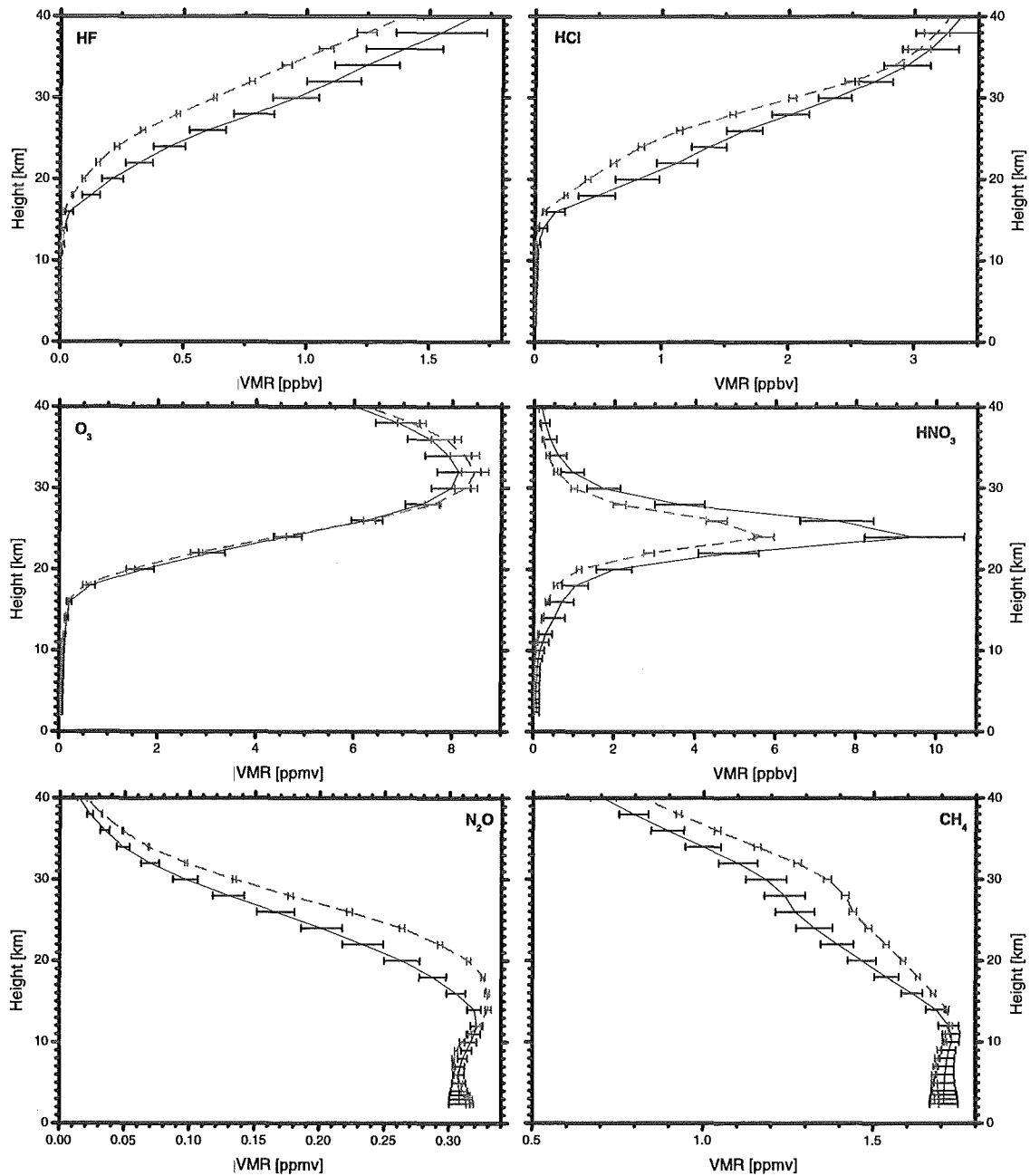
Fig. 7.11: FTIR profiles for 10/2/01 (airmasses from low latitudes). Shown are climatological profiles of FTIR measurements (solid lines) and profiles for 10/2/01 (dashed lines) of HF, HCl, O_3, HNO_3, N_2O, and CH_4.

7.3   Correlation with Vertical and Horizontal Transport

The trace gas ratios illustrated that most of the short-term variations are due to vertical or horizontal transport processes. Therefore, it is assumed that components with similar horizontal and vertical distribution patterns react in a similar manner on horizontal and vertical motions. Now, it is tried to relate the variations of certain trace gases directly to transport processes. Therefore, the dynamical tropopause height is applied as an indicator of short-term vertical transport and the calculated backward trajectories as parameter for the horizontal transport.

7.3.1   Correlation with Tropopause Height

As seen in Figure 4.3, changes in the tropopause height occur mainly on a rather small timescale. However, there is an annual cycle with a generally higher tropopause in summer than in winter. The changes in the trace gas profiles are also due to processes that occur on different timescales. Upwelling or chemical partitioning (e.g. partitioning between $NO + NO_2$ and HNO_3) influence the trace gases over typical timescales of $\frac{1}{2}$ year, whereas horizontal or vertical transport may produce abrupt changes. For a reasonable comparison of changes in the tropopause height and changes in the trace gas profiles, it is therefore necessary to remove these long-term variations.

It is searched for a correlation between the 2 PVU dynamical tropopause height and a residual VMR isoline typical for the lowermost stratosphere of the stratospheric gases O_3, HF, HCl, and HNO_3 and the tropospheric gases N_2O, CH_4, HCN, and OCS. For this purpose, a multiple linear least square regression is performed. In addition to the variation of tropopause height, 4 sine functions with frequencies of 2, $1\frac{1}{2}$, 1, and $\frac{1}{2}$ year^{-1} and their phases as well as a linear term are fitted in order to account for the long-term variations, which comprise annual and interannual variations and their rough asymmetries. The left parts of the Figures 7.12 to 7.14 depict the original isoline heights versus time (open circles) and their long-term variations derived from the multiple regression analysis (solid lines). The residual VMR isolines are then the measured ones separated from the long-term variations. The right panels of Figures 7.12 to 7.14 show the correlation between the 2 PVU dynamical tropopause height and a residual VMR isoline typical for the lowermost stratosphere of the stratospheric gases O_3, HF, HCl, and HNO_3 and the tropospheric gases N_2O, CH_4, HCN, and OCS.

Figures 7.12 presents the results for O_3. Apart from the FTIR profiles, all O_3 sonde profiles measured between February 1999 and July 2001 were analyzed. The long-term variation obtained from the multiple regression method shows rising iso-
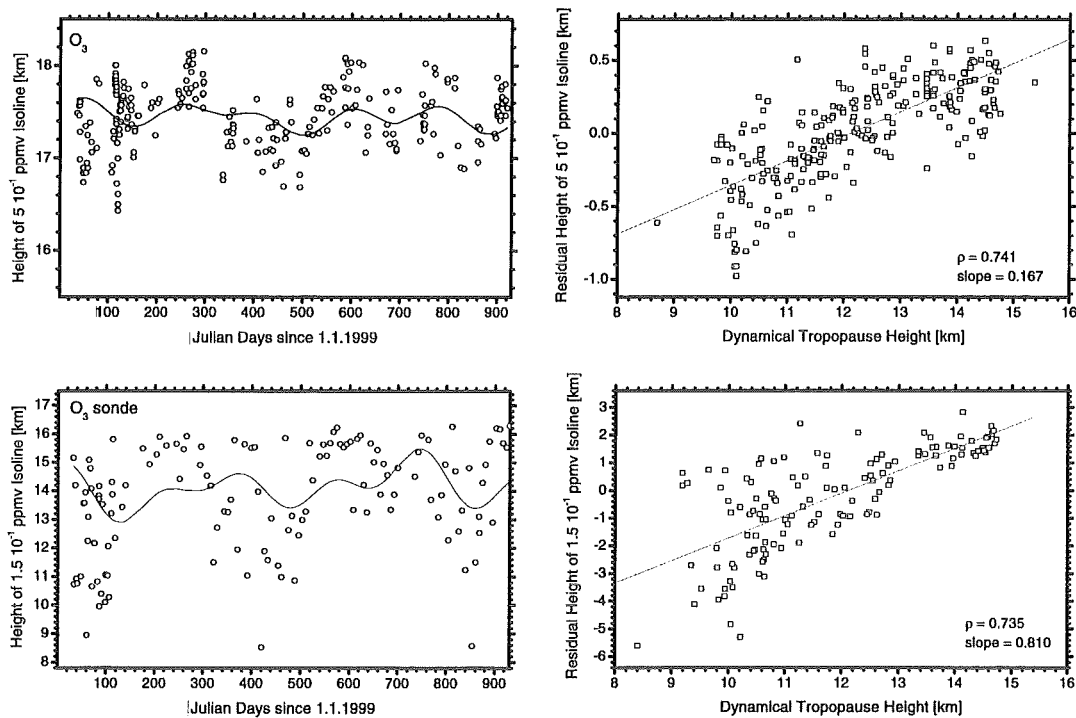
Fig. 7.12: Correlation between the height of the VMR isolines of O_3 and the
tropopause height. Shown are plots for FTIR results (above) and sonde
data (below). Left part: Height of isoline (open circles) and long-term
variation (solid line). Long-term variation is retrieved as described in
the text. Right part: Residual height of isoline versus tropopause height
(open squares) and its linear regression line (solid line). Residual height
is the original height corrected by the long-term variations (for more
details, see text).

lines in summer (enhanced upwelling) and decreasing isolines in winter. Additionally,
especially low isolines are always observed in December/January, which may be due
to amplified transport from higher latitudes during this period. As obvious from
the right panel, the 5×10^{-1}ppmv isoline of the FTIR profiles correlates well with
the tropopause height. The height resolution of the O_3 sonde results too good for
a non-ambiguous isoline height attribution in the lowermost stratosphere. There-
fore, the profiles were smoothed by convolution with a Gauss function ($\sigma^2 = 1$ km).
In particular, a good correlation between the O_3 sonde's 1.5×10^{-1}ppmv isoline
and the tropopause height was found. Similar to the FTIR isoline, the long-term
variation indicates increasing isolines in summer and a secondary minimum in De-
cember/January. Best correlations are found for O_3 sonde isolines which are situated

around the typical tropopause height (e.g. 1.5×10^{-1}ppmv isoline). In case of the FTIR profile best correlations are achieved for isolines around 17km. At lower altitudes the gradient of height versus isoline is too large for the low resolved FTIR profiles (see e.g. Figure 5.14b), which results in a less defined correlation. The sparse FTIR height resolution also explains the differences in the slopes: For the sonde merely isolines relatively close to the tropopause region correlate with the tropopause height. For the FTIR, on the other hand, the correlations are "smeared" over a wider altitude range, which results in a lower slope.

In Figures 7.13 the results for the FTIR profiles of HF, HCl, and HNO_3 are depicted. In all three cases, the retrieved long-term variations indicate upwelling in summer. The secondary minimum in July in the long-term variation of HNO_3 is due to changed nitrogen partitioning in summer, as discussed in chapter 6. For these gases, good correlations with the tropopause height are found.

The results of N_2O, CH_4, and OCS are illustrated in Figure 7.14. Once again, the retrieved long-term variation of the isolines indicates the enhanced upwelling in summer for all 3 components. The correlations with the tropopause height are weaker than for the stratospheric components, but they are still satisfactory. This may be attributed to the lower height resolution of the FTIR profiles of those gases in the lower stratosphere as compared to their stratospheric counterparts.

Keeping in mind that by fitting merely frequencies of $2 \text{-} \frac{1}{2}$ year^{-1}, the residual VMR very likely still includes chemically based variations or long-term transport not registered by the height variations of the 2 PVU isoline, the resulting correlations are satisfactory, especially for stratospheric gases. Fitting of further frequencies would even more clarify these correlations, but it is decided to restrict to the 4 most evident frequencies in order to ensure the correlations to be purely physical and not artificially produced by the fitting procedure.

Additionally, we tried to correlate the isolines derived by KASIMA. For this, the same fitting procedure as for the FTIR isolines was applied to KASIMA isolines lying typically between 12 and 18 km, but no correlation resulted (correlation coefficient ρ below 0.05). This may be due to a boundary effect, since the lowest atmospheric level considered by the model (10 km) is very close to the tropopause. Sometimes, especially in winter, it lies even completely in the stratosphere.
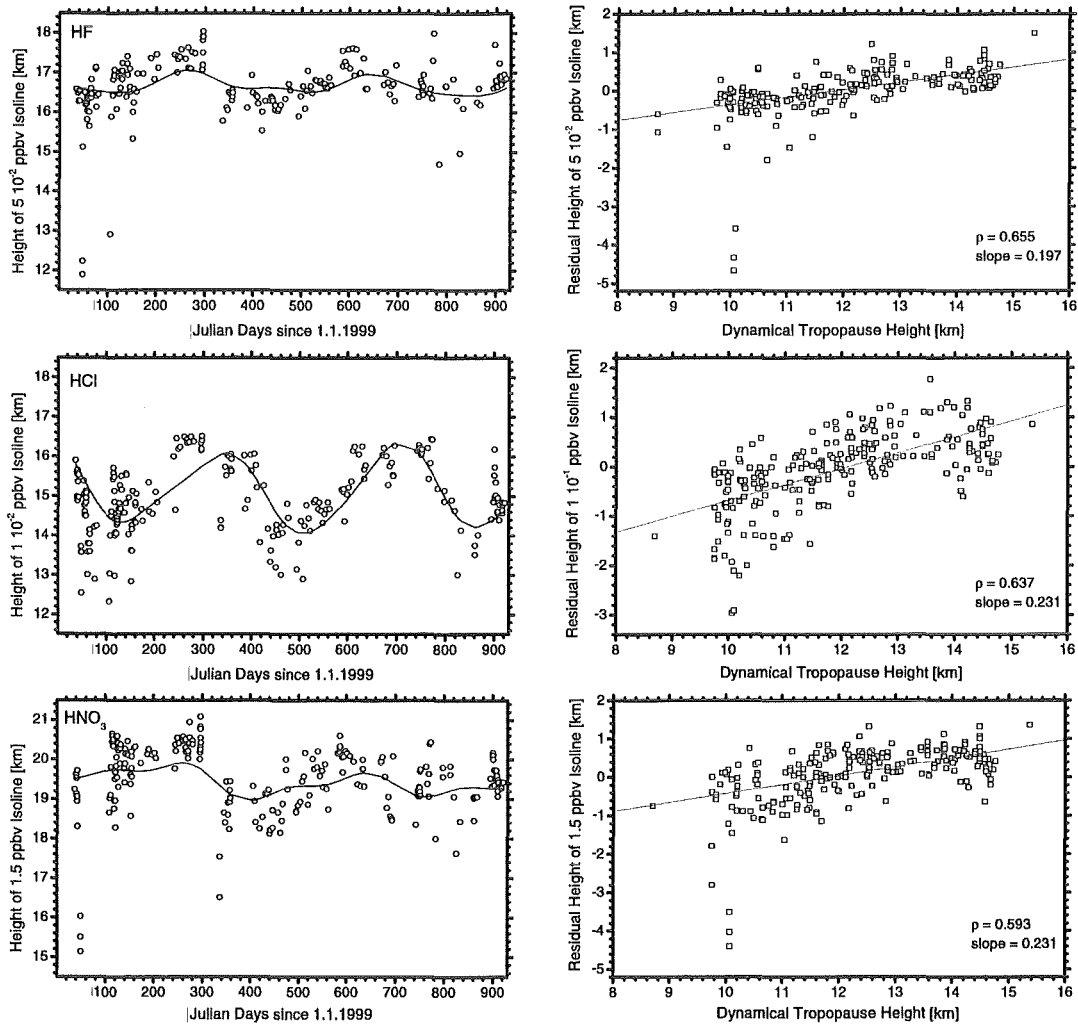
Fig. 7.13: Same as Figure 7.12, but for FTIR results of HF, HCl, and HNO₃. Left part: Height of isoline (open circles) and long-term variation (solid line). Long-term variation is retrieved as described in the text. Right part: Residual height of isoline versus tropopause height (open squares) and its linear regression line (solid line). Residual height is the original height corrected by the long-term variations (for more details, see text).
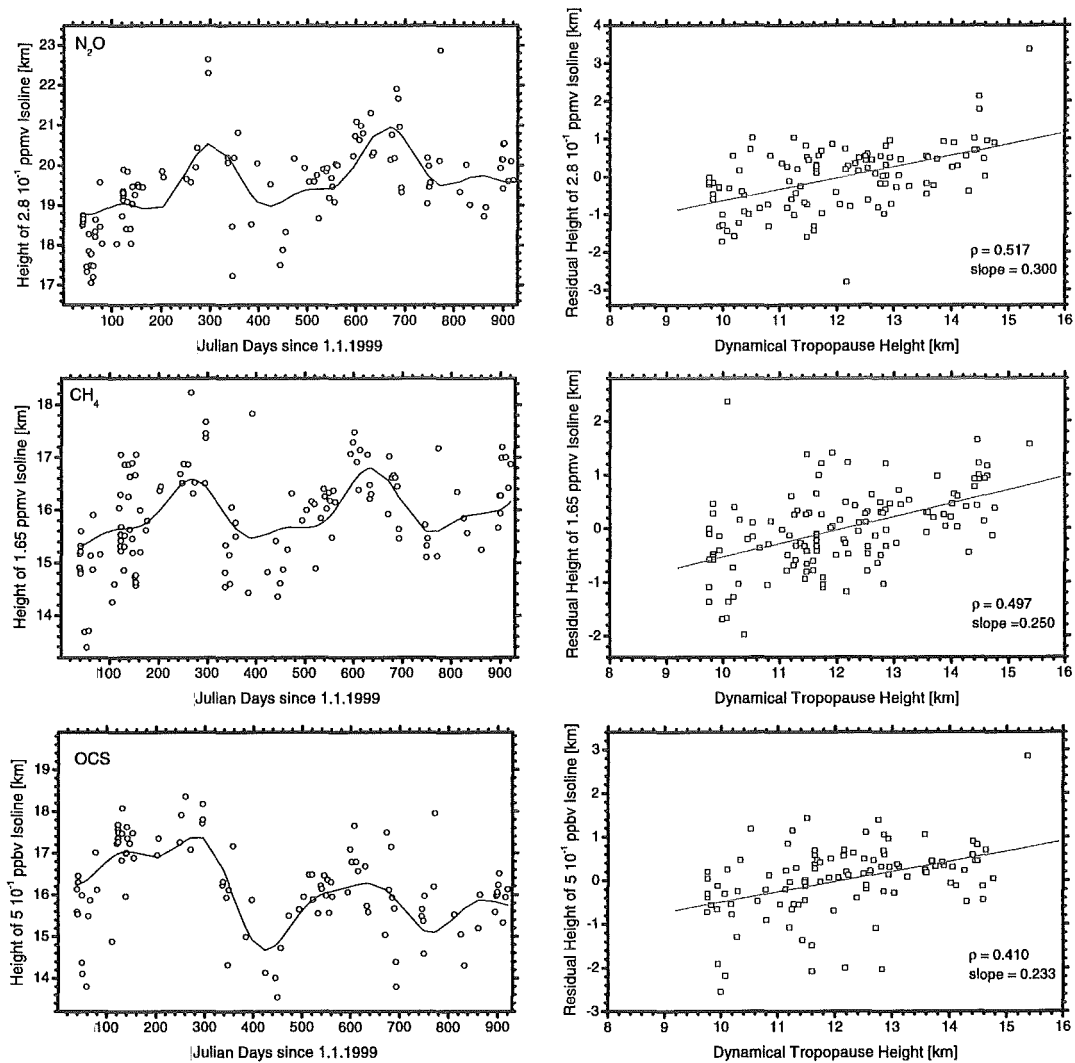
Fig. 7.14: Same as Figure 7.13, but for tropospheric gases.

7.3.2   Correlation with Origin of Airmass
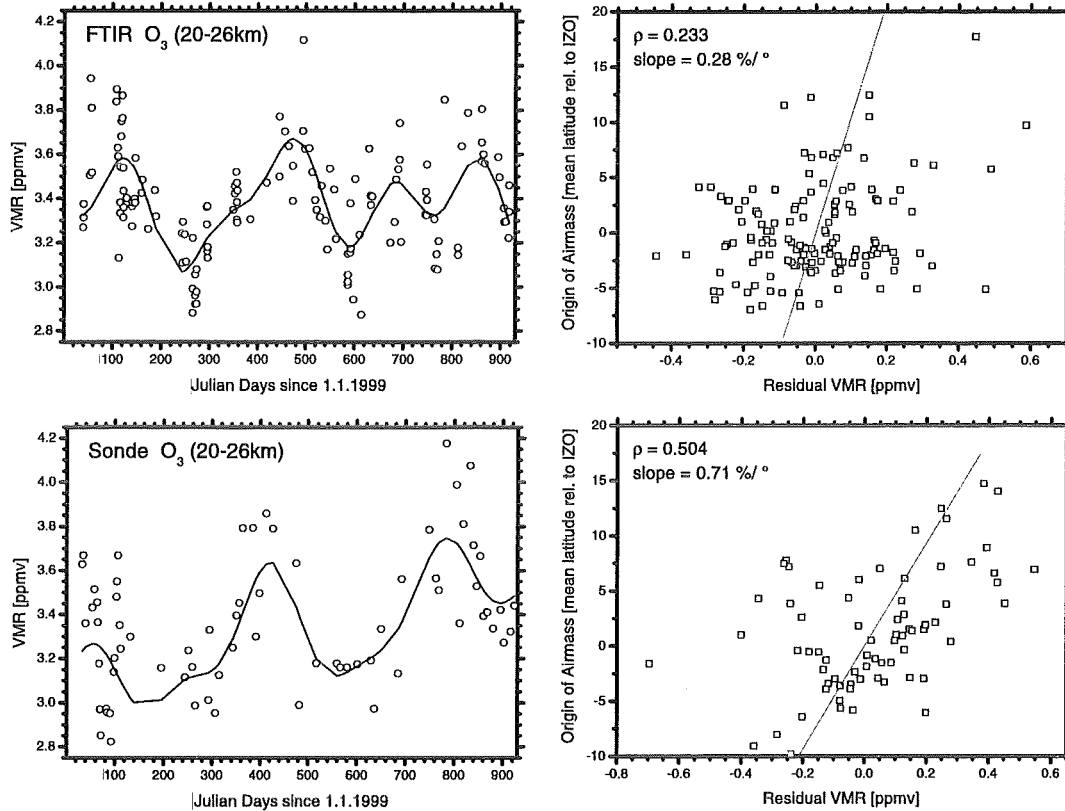
Fig. 7.15: Correlation between the mean VMR of the O_3 sonde and the FTIR and the origin of the airmass at 550 K. Left part: Mean VMR (open circles) and long-term variation (solid line). Right part: Residual mean VMR versus origin of airmasses (open squares) and its linear regression line (solid line).

Following the direct correlation of vertical motion and trace gas variations in the previous section, horizontal transport shall now be related to trace gas variations using backward trajectories. As mentioned in chapter 4, calculations of backward trajectories from January 1999 to August 2001 for the 300, 330, 350, 380, 400, 450, 550, and 675 K levels were provided by NASA's Climate Monitoring and Diagnostics Laboratory [25]. A simple mean value is calculated for the latitudinal and longitudinal location of the detected airmass relative to IZO during the 10 days prior to its arrival in order to identify the origin of the airmass (these values are also depicted in Figures 4.5 and 4.6). Generally, the backward trajectories differ widely depending on their level, i.e. typically each level is influenced by airmasses originating from

different regions. Thus, for reasons of ambiguity, we should restrict to a limited altitude range (see also Figures 7.7 and 7.8). The 550 K level was chosen, since it corresponds to the altitude region (22-24 km, see Figure 4.4) where the FTIR profiles for most components show the best height resolution. Subsequently, it is tried to correlate changes in the origin of the airmass to the mean VMR between 20 and 26 km. Due to the arguments mentioned already above, it is necessary to remove long-term variations in order to compare changes in the origin of the airmass with changes in the trace gas profiles. Therefore, a multiple linear least square regression is performed. Here, 4 sine functions with frequencies of 2, $1\frac{1}{2}$, 1, and $\frac{1}{2}$ year^{-1} and their phases, and a linear term are fitted apart from the origin of the airmass parameterization. This yields a residual mean VMR with removed long-term variations. The additionally fitted functions account for annual and interannual variations and their rough asymmetries.

The left panels of Figures 7.15 to 7.17 show the mean VMR for FTIR data between 20 and 26 km (circles) and their long term variations retrieved as described above (solid line). For O_3, we additionally analyzed the O_3 sonde data from February 1999 to July 2001. The decrease for all stratospheric components (O_3, HF, HCl, and HNO_3) and the increase for tropospheric gases (N_2O and CH_4) seen in the long-term VMR values in summer is due to enhanced upwelling. For O_3 the decrease in summer is weakest (peak to peak: <18%), since it is partly compensated by amplified photochemical production. For HCl a decrease of appr. 50% is observed. HF and HNO_3 show the largest changes of the long-term VMR during summer (peak to peak: HF: 100%; HNO_3: 75%). In the case of HF, this is due to younger airmasses in summer and, consequently, less release of fluorine from its precursors (as already discussed above). HNO_3 is additionally decreased by enhanced photodissociation in summer according to equation 2.28.
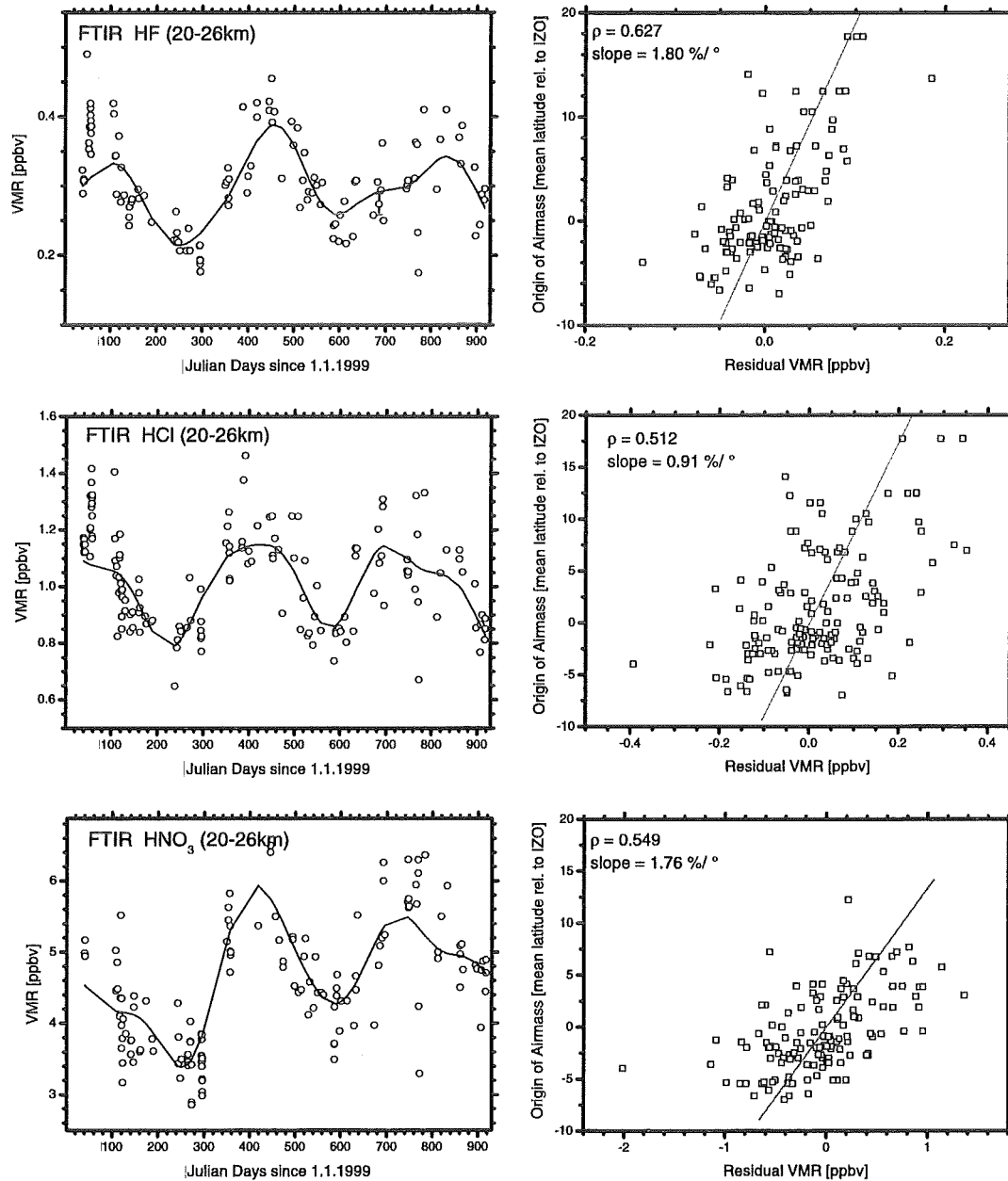
Fig. 7.16: Correlation between the mean VMR of HF, HCl, and HNO₃ and the origin of the airmass at 550 K. Left part: Mean VMR (open circles) and long-term variation (solid line). Right part: Residual mean VMR versus origin of airmasses (open squares) and its linear regression line (solid line).
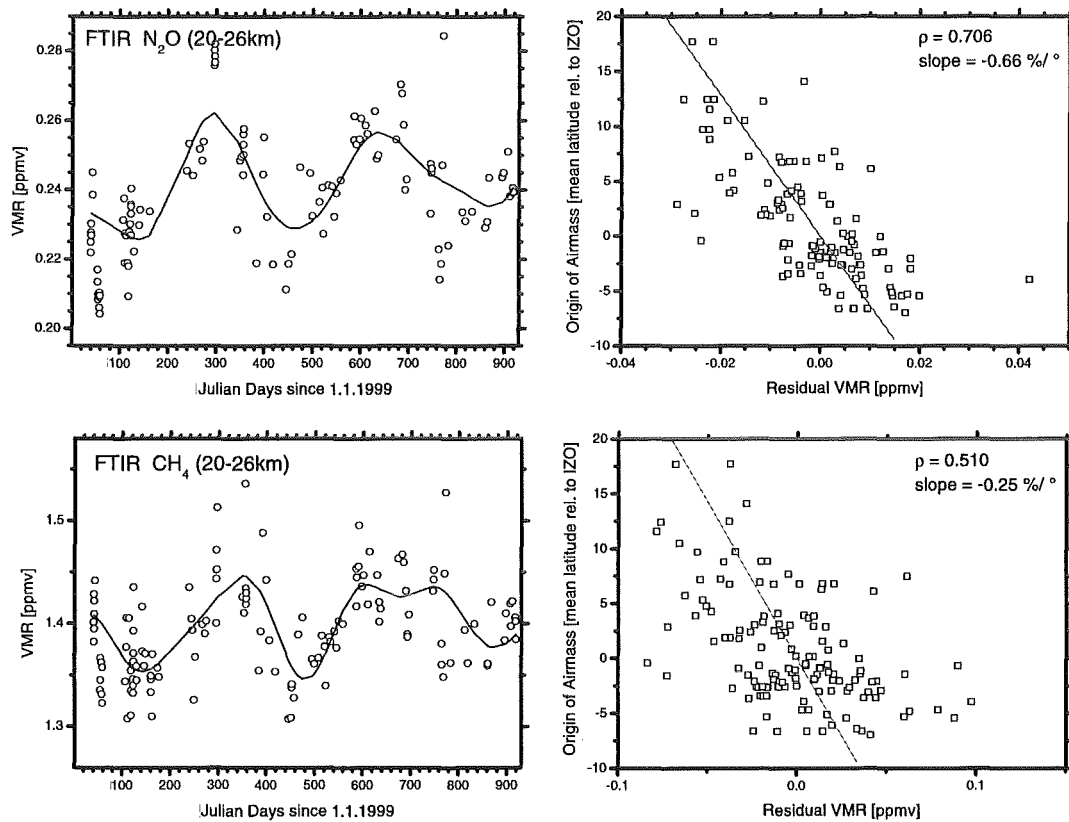
Fig. 7.17: Same as Figure 7.16, but for N_2O and CH_4.

The right panels of Figures 7.15 - 7.17 show the correlation between the residual mean VMR between 20 and 26 km and the origin of the airmass at 550 K given in mean latitude relative to IZO as described above. For stratospheric gases (O_3, HF, HCl, and HNO_3) the correlation retrieved indicates higher VMR for airmasses originating from higher latitudes, and lower VMR for tropically influenced airmasses. The correlations of tropospheric components (N_2O and CH_4) indicate the contrary, i.e. lower VMR for high-latitude airmasses and high VMR for tropical airmasses. Stratospheric tracers increase steeply in meridional direction from the tropics towards high latitudes, while tropospheric components show the opposite behavior (see e.g. Figures 2.4 to 2.6). This latitudinal distribution pattern is mainly due to tranport processes (upwelling in tropics, downwelling at higher latitudes). It is therefore demonstrated by the correlations observed that a great part of the short-term variations of the trace gases recorded at IZO is caused by transport processes. By these correlations, the observations made above on the days of 18/2/99, 9/2/00, and 10/2/01 under the case study are extended to the whole measurement period. For O_3, the correlation is weaker (lower ρ value) than for the other components, which is consistent with its relatively higher chemical reactivity. Thus, the amount of O_3 is relatively more influenced by short-time chemical processes than the other chemically more stable trace gases analyzed. The regression line of O_3, i.e. its typical change of VMR per change in latitude of airmass origin, also is less steep (lower slope value) than for the other stratospheric gases, which may be explained by its source region being situated in the tropical stratosphere. For tropical airmasses, the decrease caused by upwelling is partly counterbalanced by a higher production rate. The contrary may be observed for HF and HNO_3 whose regression lines are especially steep. Besides a decrement caused by enhanced upwelling, these components show additionally low values in the tropics due to the presence of younger airmasses (less release of HF from its precursors) and higher solar fluxes (more effective photodissociation of HNO_3). At high latitudes, they are not only subject to downwelling, but additionally increased due to advanced decomposition of fluorine substances (HF) and less photodissociation (HNO_3).

Except for O_3, all correlations are satisfactory, keeping in mind that a simple mean value over the 10 days prior to the airmass's arrival was used to decide on the origin of the detected airmass, that further variations in longitudinal directions were not considered and that, like in the previous section, the residual VMR may probably still include variations due to long-term horizontal or vertical transport processes not registered by the simple mean latitude parameterization.
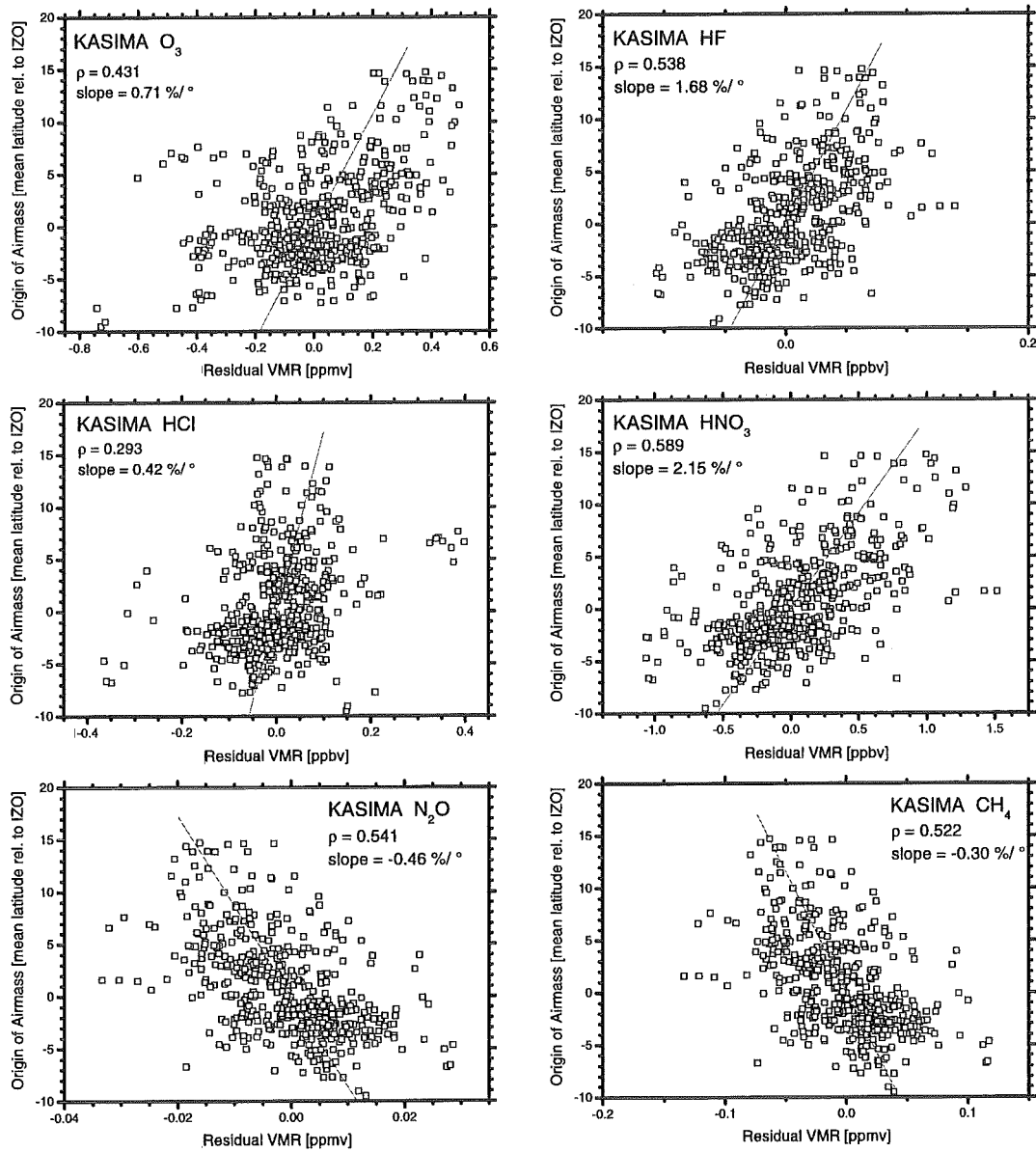
Fig. 7.18: Correlation between the mean VMR of the KASIMA data and the origin of the airmass at 550 K

	O_3	HF	HCl	HNO_3	N_2O	CH_4
FTIR	0.28 %/°	1.80 %/°	0.91 %/°	1.76 %/°	-0.66 %/°	-0.25 %/°
KASIMA	0.71 %/°	1.68 %/°	0.42 %/°	2.15 %/°	-0.46 %/°	-0.30 %/°
sonde	0.71 %/°					

Table 7.1: Typical dependence of VMR at 550 K on the origin of the airmass

The same fitting procedure as for the FTIR mean VMR values was applied to KASIMA mean VMR values between 20 and 26 km. The long-term VMR values retrieved show a similar evolution as for the FTIR. The resulting correlations are shown in Figure 7.18. Similar correlation coefficients (ρ value) as for the FTIR are determined. Largest differences are seen for O_3 and HCl. Whereas KASIMA O_3 correlates better than FTIR O_3, the contrary is observed for HCl. The retrieved regression lines (slope value), i.e. typical change of VMR per change in latitude of airmass origin, are quite similar for FTIR and KASIMA, which indicates that the latitudinal variations of the trace gases are modelled in consistency with the measurements. The largest differences are seen in O_3 and HCl, which at least for HCl is certainly due to the problems of the modelled HCl (see chapter 6). Table 7.1 lists the slopes of the retrieved linear regression lines, for FTIR and KASIMA and the O_3 sonde.

Chapter 8

Summary and Outlook

FTIR measurements were conducted at the low-latitude site of the Izaña Observatory (IZO, 28°N), Tenerife, Spain, from February 1999 to July 2001. Besides the detection of highly-resolved atmospheric absorption spectra (approximately 200 measurement days), the instrument characteristics were determined regularly (about every 2 months) according to [26]. The measured ILS was subsequently used for profile retrieval. It was found that the instrument alignment remained quite stable during the whole measurement period, i.e. no greater readjustments had to be made.

The measurements over $2\frac{1}{2}$ years provided clear annual cycles for all trace gases. From May to October, the profiles indicated enhanced upwelling and, thus, generally higher ZCA of tropospheric gases and lower ZCA of stratospheric gases. In winter, the stratosphere proved to be more disturbed by enhanced wave activity, which was reflected by larger short-term variations of the detected species. For HF a particularly strong annual cycle was observed, which is due to the stratosphere above IZO showing different characteristics in winter and summer. In summer, a rather tropical stratosphere prevails, above IZO, which implies relatively young stratospheric airmasses. In winter, it shows extra-tropical characteristics along with relatively old airmasses. Younger stratospheric air is characterized by less release of HF from its precursors and, hence, relatively low VMR values. In contrast to this, O_3 shows a weaker annual cycle, since a decrease in summer due to upwelling is partly counterbalanced by a higher O_3 production rate present in a tropical stratosphere. The strong annual cycle of HNO_3 is due to enhanced photolysis to NO_x in summer. This also explains the cycles of NO_2 and NO.

The FTIR results are compared to other measurements conducted at IZO or in its vicinity. The O_3 ZCAs showed a good agreement with results from Differential Optical Absorption Spectroscopy (DOAS), the Brewer spectrometer, and O_3 sonde measurements. NO_2 data are consistent with the respective DOAS results. The comparison of O_3 profiles between sonde and FTIR revealed in a good agreement. The cruise of the POLARSTERN research vessel from the German Alfred-Wegener

Institute close to IZO at the end of December 1999 allowed to compare nearly all stratospheric components, which also resulted in a reasonable agreement. Merely the comparison of H_2O ZCA with radiosonde data results in large deviations on some days, which may be explained mainly by the different locations of the measuring instruments (FTIR and sonde), e.g. surface influences may lead to higher FTIR VMR values up to 3.5 km as compared to the sonde which above 2.5 km generally represents VMR values of the free atmosphere. This is consistent with the good agreement of the H_2O sonde and FTIR profiles between 4 and 20 km.

The modelled KASIMA data show the same general evolution like the FTIR data, i.e. enhanced upwelling in summer and higher variability in winter. Both KASIMA and the FTIR yield more pronounced annual cycles of HF and HNO_3, and a weaker annual cycle of O_3 due to enhanced tropical influences in summer. However, large differences between the absolute values of the modelled and the measured data are found. As illustrated in chapter 6, all these differences may be explained by a modelled stratosphere that experiences larger tropical influences than suggested by the measurements and, hence, they confirm that the link between tropical and extra-tropical stratosphere is still not understood completely.

Furthermore the modelled data does not show any correlations with the dynamical tropopause height, whereas both FTIR and O_3 sonde data clearly exhibit such a correlation. This is attributed to a boundary effect. It is currently being examined whether reducing the boundary height of the model yields such an improvement.

In the middle stratosphere, the model and measurement results react quite similarly on horizontal transport, which is shown by correlations of KASIMA and FTIR values with the origin of the airmass for the altitude range of 20-26 km. This demonstrates that the model calculates a latitudinal trace gas distribution like the one detected by the FTIR. Larger discrepancies are only seen for HCl, which may be due to errors in the modelled HCl, as described in chapter 6.

Further automation of the evaluation procedure will be an important task in the future. In particular, the automations performed within this work should be better implemented into the retrieval code PROFFIT in order to facilitate and speed up the time-consuming evaluation of the numerous measurements. Moreover automation of the measurements would allow to perform the measurements even more frequently. It was proven that a high frequency of the measurements is important for detecting interesting features like tropical streamers or filaments originating from high latitudes, especially if it is intended to estimate their frequency.

The evaluation of NO could be improved considerably by fitting the solar line along with the absorption features during the evaluation procedure. The corresponding improvements of KOPRA are currently in work.

The comparisons of modelled and measured data for lower latitudes are important for an improved understanding of the dynamics and chemistry of the stratosphere. This is in particularly illustrated by the disagreements found between

KASIMA and FTIR. Further model validation will be made. With respect to the validation of satellites, the generally good measurement conditions at IZO are of great benefit, since they allow to perform measurements with high frequency. This will especially apply to the ENVISAT satellite, which is scheduled for launch in March 2002.

134

Bibliography

[1] Bais, A. F., B. G. Gardiner, H. Slaper, M. Blumthaler, G. Bernhard, , R. McKenzie, A. R. Webb, G. Seckmeyer, B. Kjeldstad, T. Koskela, P. J. Kirsch, J. Gröbner, J. B. Kerr, S. Kazadzis, K. Leszczynski, D. Wardle, W. Josefsson, C. Brogniez, D. Gillotay, H. Reinen, P. Weihs, T. Svenoe, P. Eriksen, F. Kuik, A. Redondas, *SUSPEN intercomparion of ultraviolet spectroradiometers*, J. Geophys. Res., 106, 12509, 2001

[2] Ballard, J., W. B. Johnston, M. R. Gunson, P. T. Wassel, *Absolute absorption coefficients of* $ClONO_2$ *infrared bands at stratospheric temperatures*, J. Geophys. Res., 93, 1659, 1988

[3] Beer, R., *Remote sensing by Fourier transform spectroscopy*, Wiley & Sons, 1992

[4] Blumenstock, T., H. Fischer, A. Friedle, F. Hase, P. Thomas, *Column amounts of* $ClONO_2$, HCl, HNO_3, *and* HF *from ground-based FTIR measurements made near Kiruna, Sweden, in late winter 1994*, J. Atmos. Chem., 26, 311, 1997

[5] Brewer, A. W., *Evidence for a world circulation provided by measurements of helium and water vapor distribution in the stratosphere*, Q. J. Roy. Met. Soc., 75, 351, 1949

[6] Bruehl, C., and P. J. Crutzen, *NOx-catalyzed ozone destruction and NOx activation at midlatitudes to high latitudes as the main cause of the spring to fall ozone decline in the Northern Hemisphere*, J. Geophys. Res., 105, 12163, 2000

[7] Calbet, X., P. M. Romero, M. C. Romero, *1997-1990 Measurements of aerosol size distributions at Izaña (Tenerife) and its relationship with the continental origin of air masses*, Aceptado para los Proceedings 2ª Asamblea Hispano-Portuguesa de Geodesia y Geofísica, Lagos (Portugal), 8-12 Febrero 2000

[8] Carter III R. O., N. E. Lindsay, and D. Beduhn, *A solution to baseline uncertainty due to MCT detector nonlinearity in FT-IR*, Applied Spectroscopy, 44, 1147, 1990

[9] Chandrasekhar, S., *Radiative transfer*, Dover Publications Inc.,New York, 1960

[10] Chapman, S., *A Theory of Upper Atmospheric Ozone*, Mem. Roy. Meteorol. Soc. 3, 103, 1930

[11] Chen, P., *The influence of zonal flow on wave breaking and tropical-extratropical interaction in the lower stratosphere*, J. Atmos. Sci., 53, 2379, 1996

[12] Chipperfield, M. P., M. Burton, W. Bell, C. Paton Walsh, T. Blumenstock, M. T. Coffey, J. W. Hannigan, W. G. Mankin, B. Galle, J. Mellqvist, E. Mahieu, R. Zander, J. Notholt, B. Sen, and G. C. Toon, *On the use of* HF *as a reference for the comparison of stratospheric observations and models*, J. Geophys. Res., 102, 12901, 1997

[13] Crutzen, P. J., *Ozone production rates in an oxygen, hydrogen-nitrogen oxide atmosphere*, J. Geophys. Res., 76, 7311, 1971

[14] Díaz, J. P., F. Expósito, C. J. Torres, F. Herrera, J. M. Prospero, M. C. Romero, *Radiative properties of aerosols in Saharan dust outbreaks using ground-based and satellite data: Applications to radiative forcing*, J. Geophys. Res., 106, 18403, 2001

[15] Dobson, G. M. G., *Origin and distribution of polyatomic molecules in the atmosphere*, Proc. Roy. Soc. Lond. A, 236, 187, 1956

[16] Farman, J. C., B. G. Gardiner, J. D. Shanklin, *Large Losses of Total Ozone in Antarctica Reveal Seasonal ClO_X/NO_X Interaction*, Nature, Vol. 315, pp. 207–210, May 1985

[17] Fischer, H., *Remote sensing of atmospheric trace constituents using Fourier Transform Spectroscopy*, Ber. Bunsenges. Phys. Chem., 306, 1992

[18] Garcia, R. R. and S. Solomon, *A numerical model of the zonally averaged dynamical and chemical structure of the middle atmosphere*, J. Geophys. Res., 88, 1379, 1983

[19] Gil M., O. Puentedura, M. Yela, E. Cuevas, *Observations of NO2 and O3 columns by visible spectroscopy during the eclipse of February 26, 1998*, J. Geophys. Res., 105, 3583, 2000

[20] Grant, W. B., E. V. Browell, J. Fishman, V. G. Brackett, R. E. Veiga, D. Nganga, A. Minga, B. Cros, C. F. Butler, M. A. Fenn, C. S. Long, and L. L. Stowe, *Aerosol associated changes in the tropical stratospheric ozone following the eruption of Mount Pinatubo*, J. Geophys. Res., 99, 8197, 1994

[21] Grant, W. B., E. Browell, C. Long, L. Stowe, R. Grainger, and A. Lambert, *Use of volcanic aerosol to study the tropical stratospheric reservoir*, J. Geophys. Res., 101, 3973, 1996

[22] Griffith, D. W. T., N. B. Jones, W. A. Matthews, *Interhemispheric ratio and annual cycle of carbonyl sulfide (OCS) total column from ground-based solar FTIR spectra*, J. Geophys. Res., 103, 8447, 2000

[23] Hampson, J., *Photochemical behavior of the ozone layer*, Canadian Armament Research and Development Establishment (CARDE), Technical note 1627, 11-18, 1964

[24] Harris, J. M., *An analysis of 5-day midtropospheric flow patterns for the South Pole: 1985-1989*, Tellus, 44B, 409, 1992

[25] Harris, J. M., and J. D. V. Kahl, *An analysis of 10-day isentropic flow patterns for the Barrow, Alaska: 1985-1992*, J. Geophys. Res., 99, 25845, 1994

[26] Hase, F. T. Blumenstock, C. Paton-Walsh, *Analysis of the instrumental line shape of high-resolution Fourier transform IR spectrometers with gas cell measurements and new retrieval software*, Applied Optics, 38, 3417, 1999

[27] Hase, F., *Inversion von Spurengasprofilen aus hochaufgelösten bodengebundenen FTIR-Messungen in Absorption*, Dissertation, genehmigt von der Fakultät für Physik der Universität Karlsruhe (TH), 2000

[28] Haynes, P. H., and E. Shuckburgh, *Effective diffusivity as a diagnostic of atmospheric transport: 1. Stratosphere*, J. Geophys. Res., 105, 22777, 2000

[29] Holton, J. R., *An introduction to dynamic meteorology*, Academic Press, (New York), 1979

[30] Holton, J. R., P. H. Haynes, M. E. McIntyre, A. R. Douglass, R. B. Rood, and L. Pfister, *Stratosphere-troposphere exchange*, Rev. Geophys., 33, 403, 1995

[31] Höpfner, M., G. P. Stiller, M. Kuntz, T. v. Clarmann, G. Echle, B. Funke, N. Glatthor, F. Hase, H. Kemnitzer, and S. Zorn, *The Karlsruhe optimized and precise radiative transfer algorithm. Part II: Interface to retrieval applications*, SPIE Proceedings, 3501, 186, 1998

[32] Huster, S., *Bau eines automatischen Sonnenverfolgers für bodengebundene IR-Absorptionsmessungen*, Diplomarbeit, genehmigt von der Fakultät für Physik der Universität Karlsruhe (TH), 2000

[33] Jaeglé, L., C. R. Webster, R. D. May, D. W. Fahey, E. L. Woodbridge, E. R. Keim, R. S. Gao, M. H. Proffitt, R. M. Stimpfle, R. J. Salawitch, S. C. Wofsy, and L. Pfister, *In situ measurements of the* NO_2/NO *ratio for testing atmospheric photochemical models*, Geophys. Res. Lett., 21, 2555, 1994

[34] Johnson, J. E., A. R. Bandy, D. C. Thornton, T. S. Bates, *Measurements of atmospheric carbonyl sulfide during the NASA chemical instrumentation test and evaluationproject: Implications for the global* COS *budget*, J. Geophys. Res., 98, 23443, 1993

[35] Johnston, H. S. and J. Podolske, *Interpretations of stratospheric chemistry*, Rev. Geophys. Space Phys. 16, 491, 1978

[36] Juckes, M. N. and M. E. McIntyre, *A high resolution, one layer model of breaking planetary waves in the stratosphere*, Nature, 328, 590, 1987

[37] Karbstein, H., *Bestimmung von Säulengehalten atmosphärischer Spurengase aus mit Eigenstrahlung überlagerten IR-Spektren*, Diploma thesis, IMK, Universität Karlsruhe, 1994

[38] Kentarchos A., G. J. Roelofs, J. Lelieveld, E. Cuevas, *On the origin of elevated surface ozone concentrations at Izana Observatory during the last days of March 1996: a model study*, Geophys. Res. Lett., 27, 3699, 2000.

[39] Kouker, W., D. Offermann, V. Küll, R. Ruhnke, T. Reddmann, A. Franzen, *Streamers observed by the CRISTA experiment and simulated in the KASIMA model*, J. Geophys. Res., 104, D13, 16405, 1999

[40] Kowol-Santen, J. and G. Ancellet, *Transport across the subtropical tropopause: observations and model guided analyses*, European Commission Air Pollution Research Report 73, Stratospheric Ozone 1999: Proceedings of the fifth European Symp. Saint Jean de Luz, France, 27 September - 1 October, 229, 1999

[41] Kuntz, M., M. Höpfner, G. P. Stiller, T. v. Clarmann, G. Echle, B. Funke, N. Glatthor, F. Hase, H. Kemnitzer, and S. Zorn *The Karlsruhe optimized and precise radiative transfer algorithm. Part III: ADDLIN and TRANSF algorithms for modeling spectral transmittance and radiance*, SPIE Proceedings, 3501, 247, 1998

[42] Lait, L. R., *An alternative form of potential vorticity*, J. Atmos. Sci., 51, 1754, 1994

[43] Lary, D. J., *Catalytic destruction of stratospheric ozone*, J. Geophys. Res., 102, 21515, 1997

[44] Lary, D. J., *Carbon aerosols and atmospheric chemistry*, J. Geophys. Res., 102, D3, 3671, 1997

[45] Moore, W. J., *Physical Chemistry*, Fourth Edition, Prentice Hall, Inc., Englewood Cliffs, New Jersey, USA, 1972

[46] Navascués, B. and C. Rus, *Carbon dioxide observations at Izaña baseline station, Tenerife (Canary Islands) 1984-1988*, Tellus, 43B, 118-125, 1991

[47] Notholt, J., G. C. Toon, C. P. Rinsland, N. S. Pougatchev, N. B. Jones, B. J. Connor, R. Weller, M. Gautrois, and O. Schrems, *Latitudinal variations of trace gas concentrations in the free troposphere measured by solar absorption spectroscopy during a ship cruise*, J. Geophys. Res., 105, 1337, 2000

[48] Oltmans, S. H. Levy II, J. M. Harris, J. T. Merrill, J. L. Moody, J. Lathrop, E. Cuevas, M. Trainer, M. S. O'Neill, J. M. Prospero, H. Vömel, and B. J. Johnson, *Summer and spring ozone profiles over the North Atlantic from ozone sonde measurements*, J. Geophys. Res., 101, 29179, 1996

[49] Phillips, D., *A technique for the numerical solution of certain integral equations of the first kind*, J. Ass. Comput. Math., 9, 84, 1962

[50] Pirre, M., H. Le Texier, F. Gautail, J. P. Pommereau, and R. Ramaroson, *Seasonal behavior of NO_2 total column at polar circle*, European Commission Air Pollution Research Report 34, Polar Stratospheric Ozone: Proceedings of the first European Workshop, Schliersee, Germany, 3 - 5 October, 263, 1990

[51] Polvani, L. M., D. W. Waugh, and R. A. Plumb, *On the subtropical edge of the stratospheric surf zone*, J. Atmos. Sci., 52, 1288, 1995

[52] Qinbin, L., D. J. Jacob, I. Bey, R. M. Yantosca, Y. Zhao, Y. Kondo, and J. Notholt, *Atmospheric Hydrogen Cyanide (HCN): biomass burning source, ocean sink ?*, Geophys. Res. Lett., 27, 357, 2000

[53] Raes, F., R. Van Dingenen, E. Cuevas, P. Van Velthoven, J. M. Prospero, *Observations of aerosols in the free troposphere and marine boundary layer of the subtropical N.E. Atlantic: discussion of the processes determining their size distribution*, J. Geophys. Res., 102, 21315, 1997

[54] Randel, W. J., J. C. Gille, A. E. Roche, J. B. Kurner, J. L. Mergenthaler, J. W. Walters, and E. F. Fishbein, *Planetary wave mixing in the subtropical stratosphere observed in UARS constituent data*, Nature, 365, 533, 1993

[55] Rees, D., J. Barnett, and K. Labitzke, *Cospar International Reference Atmosphere: 1986 part II. Middle Atmosphere Models*, Advances in Space Research, 10, 1990

[56] Richter, M., *Auswertung hochaufgelöster, solarer IR-Spektren aus dem Winter 1995/96: NO_x in der polaren Stratosphäre*, Diploma thesis, IMK, Universität Karlsruhe, 1997

[57] Rinsland, C. P., N. B. Jones, B. J. Connor, J. A. Logan, N. S. Pougatchev, A. Goldman, F. J. Murcray, T. M. Stephen, A. S. Pine, R. Zander, E. Mahieu, and P. Demoulin, *Northern and southern hemisphere ground-based infrared spectroscopic measurements of tropospheric carbon monoxide and ethane*, J. Geophys. Res., 103, 28197, 1998

[58] Rinsland, C. P., M. R. Gunson, P. H. Wang, R. F. Arduini, B. A. Baum, P. Minnis, A. Goldman, M. C. Abrams, R. Zander, E. Mahieu, R. J. Salawitch, H. A. Michelsen, F. W. Irion, and M. J. Newchurch, *ATMOS/ATLAS 3 infrared profile measurements of trace gases in the November 1994 tropical and subtropical upper troposphere*, J. Quant. Spectrosc. Radiat. Transfer, 60, 891, 1998

[59] Rípodas, P., R. Ramos, E. Cuevas, and X. Calbet, *1984-1999 CO_2 continuous measurements at Izaña /Tenerife. Relationship between the CO2 short-term variability and the latitude origin of air masses*, Report of the WMO 10th CO_2 experts meeting, Stockholm (Sweden), August 1999

[60] Rodgers, C. D., *Retrieval of atmospheric temperature and composition from remote measurements of thermal radiation*, Reviews of Geophysics and Space Physics, 14, 609, 1976

[61] Rothman, L. S., C. P. Rinsland, A. Goldman, S. T. Massie, D. P. Edwards, J. M. Flaud, A. Perrin, C. Camy-Peyret, V. Dana, J. Y. Mandin, J. Schroeder, A. McCann, R. R. Gamache, R. B. Wattson, K. Yoshino, K. V. Chance, K. W. Jucks, L. R. Brown, V. Nemtchinov, and P. Varanasi, *The HITRAN Molecular Spectroscopic Database and HAWKS (HITRAN Atmospheric Workstation): 1996 Edition*, J. Quant. Spectrosc. Radiat. Transfer, Vol. 60, No. 5, pp. 665–710, 1998

[62] Ruhnke, R., W. Kouker, and T. Reddmann, *The influence of the $OH+NO_2+M$ reaction on the NO_y partitioning in the late arctic winter 1992/1993 as studied with KASIMA*, J. Geophys. Res., 104, 3755, 1999

[63] Ruhnke, R., W. Kouker, T. Reddmann, H. Berg, G. Hochschild, G. Kopp, R. Krupa, and M. Kuntz, *Model calculations of the vertical ClO distribution at Ny-Alesund during March 1997*, Geophys. Res. Lett., 26, 839, 1999

[64] Ruhnke, R., *Personal Communications*, 2001

[65] Salawitch, R. J., S. C. Wofsy, P. O. Wennberg, R. C. Cohen, J. G. Anderson, D. W. Fahey, R. S. Gao, E. R. Keim, E. L. Woodbridge, R. M. Stimpfle, J. P. Koplow, D. W. Kohn, C. R. Webster, R. D. May, L. Pfister, E. W. Gottlieb, H. A. Michelsen, G. K. Yue, M. J. Prather, J. C. Wilson, C. A. Brock, H. H. Jonsson, J. E. Dye, D. Baumgardner, M. H. Proffitt, M. Loewenstein, J. R. Podolske, J. W. Elkins, G. S. Dutton, E. J. Hintsa, A. E. Dessler, E. M. Weinstock, K. K. Kelly, K. A. Boering, B. C. Daube, K. R. Chan, and S. W. Bowen, *The diurnal variation of hydrogen, nitrogen, and chlorine radicals: Implications for the heterogeneous productions of* HNO_2, Geophys. Res. Lett., 21, 2551, 1994

[66] Sancho, J. M., E. Cuevas, and V. Carreño, *Characterization of the Double-Tropopause over the Subtropical Region from 1981-1996 Radiosonde Observations at Tenerife*, Aceptado para los Proceedings 2ª Asamblea Hispano-Portuguesa de Geodesia y Geofísica, Lagos (Portugal), 8-12 Febrero 2000

[67] Schmitt, R., B. Schreiber, and I. Levin, *Effects of long-range transport on atmospheric trace constituents at the baseline station Tenerife (Canary Islands)*, J. Atmos. Chem., 7, 335, 1988

[68] Smith, M. A. H., et al., *Collision broadening parameters from infrared spectra*, Molecular Spectroscopy: Modern Research Vol. III, K. Narahari Rao, Ed., chapter 3, Academic Press, Orlando 112, 1985

[69] Solomon, S., R. W. Portmann, R. R. Garcia, L. W. Thomason, L. R. Poole, and M. P. McCormick, *The role of aerosol variations in anthropogenic ozone depletion at northern mid latitudes*, J. Geophys. Res., 101, D3, 6713, 1996

[70] Stiller, G., M. Höpfner, M. Kuntz, T. v. Clarmann, G. Echle, B. Funke, N. Glatthor, F. Hase, H. Kemnitzer, and S. Zorn, *The Karlsruhe optimized and precise radiative transfer algorithm. Part I: Requirements, justification, and model error estimation*, SPIE Proceedings, 3501, 257, 1998

[71] Stolarski, R. S., and R. J. Cicerone, *Stratospheric chlorine: A possible sink for ozone*, Can. J. Chem., 52, 1610, 1974

[72] Tikhonov, A., *On the solution of incorrectly stated problems and a method of regularisation*, Dokl. Acad. Nauk SSSR, 151, 501, 1963

[73] Toon, G. C., J. F. Blavier, B. Sen, R. J. Salawitch, G. B. Ostermann, J. Notholt, M. Rex, C. T. Mc Elroy, J. M. Russell, *Ground-based observations of artic O_3 loss during spring and summer 1997*, J. Geophys. Res., 104, 26497, 1999

[74] Veryand, R. G., and R. A. Ebdon, *Fluctuations in tropical stratospheric winds*, Met. Mag., 90, 125, 1961

[75] Waugh, D. W., *Seasonal variation of isentropic transport out of the tropical stratosphere*, J. Geophys. Res., 101, 4007, 1996

[76] Wofsy, S. C., M. B. McElroy, and Y. L. Yung, *The chemistry of atmospheric bromine*, Geophys. Res. Lett., 2, 215, 1975

[77] Yela, M., *Estudio del Sistema O_3-NO_2 en latitudes bajas basado en observaciones desde tierra utilizando la técnica de espectroscopia de absorción UV-Visible*, PhD Thesis, Universidad de Salamanca, 1998

Nomenclature

Constants

c velocity of light; $c = 2.9979 \times 10^8$ m/s, page 42

c_p specific heat of air at constant pressure; $c_p = 29.0734$ K mol/J, page 6

h Planck's constant; $h = 6.626076 \times 10^{-34}$ Js, page 42

k_B Boltzmann's constant; $k_B = 1.38066 \times 10^{-23}$, page 7

R gas constant for air; $R = 8.315$ J/K mol, page 7

Functions

B Planck's function, page 44

BX boxcar function, page 26

bx Fourier transform of boxcar function, page 27

C self-radiation of the instrument, page 45

F function describing typical $[NO_2]/[NO]$ ratio versus time since sunrise, page 100

f shape factor, page 43

f_D shape factor for Doppler bradening, page 43

f_p	shape factor for pressure bradening, page 44
ILS	instrumental line shape function, page 45
$\mathcal{T}$	spectral sensitivity of the instrument, page 45

Greek Symbols

α_{max}	maximum off-axis angle in spectrometer, page 28
$\Delta\nu_D$	half width due to Doppler broadening, page 43
$\Delta\nu_N$	half width due to natural broadening, page 43
$\Delta\nu_p$	half width due to pressure broadening, page 44
Δk	spacing of the spectra, page 30
Δk_{FWHM}	spectral resolution as characterized by FWHM criterion, page 28
$\Delta k_{\text{Rayleigh}}$	spectral resolution as characterized by Rayleigh criterion, page 27
Δk_{self}	width of spectral rectangle due to self apodization, page 28
Δx	spacing of the interferogram, page 30
ΔS	offset in the spectrum, page 48
γ	regularization parameter, page 47
κ	absorption coefficient, page 42
κ_{jk}	absorption coefficient of gas k in layer j, page 45
λ	wavelength, page 24
μ_{nm}	electrical dipol matrix element for transition between E_n and E_m, page 42
ν_i	frequency at spectral grid point i, page 45
ν_{nm}	frequency at the center of the line, page 43

$\Phi(k)$ Phase of radiation at wavenumber k, page 25

φ latitudinal component of spherical coordinates, page 8

ρ correlation coefficient, page 120

ρ mass per unit volume, page 6

σ standard deviation of spectrum from its mean, page 48

σ_D σ value for Gaussian distribution of intensity due to Doppler broad-ening, page 43

τ optical depth, page 44

τ_{coll} mean time between collision of molecules, page 44

Θ potential temperature, page 7

ϑ longitudinal component of spherical coordinates, page 8

ζ vorticity with respect to the Earth's surface, page 8

Roman Symbols

a Earth's radius, page 8

a coefficient of typical change of [NO_2] per time, page 97

c_{jk} mixing ratio of gas k in layer j, page 45

d molecular diameter, page 44

d_j optical path lenght in layer j, page 45

E_n energy level of state n, page 42

EPV   Ertel potential vorticity, page 8

err_{noise} error due to spectral noise, page 48

err_{offset} error due to offset in the spectrum, page 48

f	Coriolis parameter, page 8
g	gravitational acceleration, page 7
g_n	total degeneracy of the state at E_n, page 42
H	scale height, page 7
I	intensity of interferogram, page 24
I_{fin}	finite interferogram (e.g. truncated by boxcar function), page 26
I_{inf}	infinite interferogram, page 26
k	wavenumber, page 24
k_{laser}	wavenumber of laser, page 30
L	maximum optical path difference, page 26
m	mass of molecule
N	number of independent spectral grid points within the half width of the absorption line, page 48
N	number of interferogram sample points, page 30
n	number density of molecules, page 42
n_j	number density in layer j, page 45
p	pressure, page 6
p_j	pressure in layer j, page 46
Q	net heating rate per unit mass, page 6
Q	total internal partition function, page 42
r	distance from Earth's center, page 8
S	intensity of spectrum, page 24
S_i	intensity of spectrum at spectral grid point i, page 45
S_{fin}	intensity of spectrum corresponding to finite interferogram, page 26
S_{IM}	imaginary part of complex spectrum, page 25

S_inf	intensity of spectrum corresponding to infinite interferogram, page 27
S_RE	real part of complex spectrum, page 25
S_{ij}	contribution of layer j to intensity of spectrum at spectral grid point i, page 46
$\mathbf{S}$	complex spectrum, page 25
$\tilde{S}$	spectrum as detected by the instrument, page 45
T	temperature, page 6
T_j	temperature in layer j, page 46
t	time, page 6
u	longitudinal wind velocity component, page 8
v	latitudinal wind velocity component, page 8
x	mirror displacement, page 24
z	spatial compenent in vertical direction, page 7

Vectors and Matrices

$\mathbf{A}^i$	Jakobi matrix of dimension $\dim(\mathbf{f}) \times \dim(\mathbf{s})$ for the ith iteration, page 46
$\mathbf{B}$	matrix connecting spectrum with additional conditions, page 47
$\Delta\mathbf{s}^i$	vector containing the differences at i spectral grid points of intensities of measured spectrum and simulated spectrum for the ith iteration, page 46
$\vec{F}$	frictional force due to viscosity, page 6
$\mathbf{f}$	vector containing parameters influencing the spectrum, page 46

$\mathbf{f^i}$ vector containing parameters influencing the spectrum as present for the ith iteration, page 46

$\vec{g}$ gravitational acceleration, page 6

$\vec{\Omega}$ angular rotation rate of the Earth, page 6

$\mathbf{r}$ vector imposing additional conditions for regularization, page 47

$\mathbf{s}$ vector containing intensity of measured spectrum at i spectral grid points, page 46

$\mathbf{s^i}$ vector containing intensity of simulated spectrum at i spectral grid points as present for the ith iteration, page 46

$\vec{v}$ wind velocity, page 6

Acronyms

CFCs Chlorofluorocarbons

CTM Chemical Transport Model

DOAS Differential Optical Absorption Spectroscopy

DU Dobson Unit

ECC Electrochemical Compound

ECMWF European Centre for Medium-Range Weather Forecasts

EPV Ertel Potential Vorticity

FT Fourier Transform

FTIR Fourier Transform Infrared Spectrometer

FWHM Full Width at Half Maximum

GAW Global Atmospheric Watch

GSFC Goddard Space Flight Center

HITRAN High Resolution Transmission Molecular Absorption Database

IAC Instituto Astrofísico Canario

ILS Instrumental Lineshape

IMK Institut für Meteorologie und Klimaforschung

INM Instituto Nacional de Meteorología

InSb Indium Antimonid

INTA Instituto Nacional de de Técnica Aeroespacial

ITCZ Inner Tropical Convergence Zone

IZO Izaña Observatory

KASIMA Karlsruhe Simulation Model of the Middle Atmosphere

KOPRA Karlsruhe Optimized and Precise Radiative Transfer Code

LINEAR software for determination of baseline errors due to nonlinearities

LINEFIT software for determination of ILS out of gas cell measurements

LTE Local Thermodynamic Equilibrium

MCT Mercury Cadmium Telluride

NASA National Aeronautics & Space Administration

NCEP National Centers for Environmental Prediction

NDSC Network for the Detection of Stratospheric Change

NOAA National Oceanic and Atmospheric Administration

OPD Optical Path Difference

pc photoconductive

PROFFIT software for determination of trace gas profiles out of solar absorption spectra

PSC Polar Stratospheric Cloud

pv photovoltaic

PVU Potential Vorticity Unit

SZA Solar Zenith Angle

UARS Upper Atmospheric Research Satellite

UV Ultraviolet

UT Universal Time

VIS Visible

VMR Volume Mixing Ratio

WMO World Meteorological Organization

ZCA Zenith Column Amount

List of Figures

154

List of Tables

Acknowledgments